Torstein Grav Aakre

Partial Discharges in Voids at Variable Voltage Frequency and Temperature

Diagnostic Testing of Stator Mainwall Insulation

Torstein Grav Aakre

Doctoral thesis

Doctoral theses at NTNU, 2020:143

NTNU
Norwegian University of Science and Technology
Thesis for the Degree of
Philosophiae Doctor
Faculty of Information Technology and Electrical
Engineering
Department of Electric Power Engineering

NTNU
Norwegian University of
Science and Technology

NTNU
Norwegian University of
Science and Technology

NTNU

Torstein Grav Aakre

Partial Discharges in Voids at Variable Voltage Frequency and Temperature

Diagnostic Testing of Stator Mainwall Insulation

NTNU
Norwegian University of
Science and Technology

Abstract

The main purpose of this thesis is to improve diagnostic testing by PD detection at variable voltage frequency by developing and experimentally testing theoretical models proposed for measurement of PDs in voids in a mica/epoxy generator bar insulation. The focus of this thesis is to compare estimated and measured values, and from that determine which physical mechanisms best describe the voltage frequency and temperature dependence of observed PD activity. The main contribution to theoretical modelling was to propose an impedance abc-model and include the dielectric response.

Two types of test object were examined: **1)** laboratory made, square-shaped insulation sheets using mica/epoxy tape, made with cylindrical voids with different diameter and gap distance and **2)** 50 cm long sections of service-aged generator bars.

A frequency sweep procedure for PD detection was developed, based on the relevant condition assessment standard IEC 60034-27 to study the frequency dependence experimentally. PDs were recorded during applying an increasing voltage of 10 equal steps, at reducing voltage frequency, starting at 300 Hz to 0.1 Hz for laboratory objects, and starting at 50 Hz to 0.1 Hz for service-aged bars. The temperature was varied in the range of 20 °C to 155 °C.

Experimental testing compared to the proposed model showed that the capacitive abc-model needed to be expanded to include both conductive elements and dielectric response; the impedance abc-model, to explain a frequency and temperature dependence for the partial discharge inception voltage (PDIV) and increased residual charge relaxation at high temperatures. The impedance abc-model was also expanded by a time lag and limited discharge area to describe the apparent charge magnitude. The capacitive abc-model describes PDIV for most cases. The effect of a high conductivity and dielectric response can explain the behaviour at low frequencies according to the impedance abc-model. The maximum apparent charge is frequency-dependent, which can be explained by PD ignition at an increased voltage caused by a time lag. Measured apparent charge magnitude

indicates that the void area only partly discharges during each PD. This was observed to cause a distribution of PD magnitudes, instead of a few large PDs. The total apparent charge per period is, however, close to the expected values based on the void geometry, and is frequency independent below 100 °C. The total apparent charge per period is frequency-dependent at 130 °C and 155 °C. This dependency was here modelled by an increased relaxation of residual charges, which enabled more PDs to occur during the same period. The relaxation was modelled by the material dielectric response.

The impedance abc-model fits to the experimental results for both insulation systems containing cylindrical voids and generator bars. This includes the important fit to the lowered PDIV and the increased total apparent charge due to an increased dielectric response at high temperatures. A correlation was found between electrical PD measurements and results from microscopy investigations of cross-sections of the generator bars. A higher PD activity was correlated to a larger void content compared to bars with lower PD activity. This correlation to void geometry is in line with results from test objects with known void geometry. Measured material properties, estimated time lag, and estimated void conductivity were used to describe the voltage frequency and temperature dependence.

Preface

This thesis is submitted in partial fulfilment of the requirements for the degree of Philosophiae Doctor (PhD) at the Norwegian University of Science and Technology (NTNU) in Trondheim, Norway. The PhD work was carried out between August 2016 and January 2020, including three months of parental leave, six months of taking courses, and two months of teaching duties, leaving two and a half years for the research presented here. The core of the work was to perform experiments and explain test results by developed models for measurable PD activity in the stator insulation of generators.

This thesis gives a comprehensive summary of collected information and results from the research performed in the PhD work. Published articles during the PhD period are attached in the appendix at the end of the thesis.

Trondheim, March 2020

Torstein Grav Aakre

Contents

Chapter 1

Introduction

1.1 Background

The average yearly Norwegian production of electric power is approximately 135 TWh. In 2019, about 94% of this was produced by 1626 hydroelectric power stations [1]. The generators installed before 1970 are producing in total one third of the total production today. Considering the expected design service life of 50-70 years, many of these generators are soon to require refurbishment or replacement [2].

Earlier, the Norwegian utilities typically operated the generators at a steady load of about 80% of the maximum nominal load. This was beneficial as it might reduce the average operating temperature by 10 °C, and possibly prolong the expected life and postpone costly replacements and refurbishments [2]. The power production today undergoes a transition from fossil-based fuel to new renewable energy sources, such as solar and wind. Such renewable sources are directly dependent on the varying weather, and additional energy storage and controllable power production are needed. Such flexibility is provided by the Norwegian hydropower magazines. This means that hydropower generators today are operated at a heavier load and with more frequent starts and stops. It is uncertain how this might affect the life expectancy of generators that are designed to operate at a more continuous load [2]. Thus, the overall effect of this is an increased need for diagnostic testing as an input to condition assessment and planning of replacement or refurbishment.

The Cigré working group A1.10 performed an international survey among utilities and manufacturers in 2009 [3]. The results showed that, in 50% of the cases, the root cause of failure was related to stator fault, caused by ageing, internal partial discharges (PDs), loose bars or thermal cycling. Around 70% of stator faults were related to PDs at or inside the stator insulation, which indicates that diagnostic testing and characterisation of PD activity are important for such insulation systems.

1

1.2   Literature Survey

This literature survey aims to describe how condition assessment of generators is performed today, with a special emphasis on measurements of PDs and how to interpret the test results by using theoretical models.

1.2.1   State of the Art of Condition Assessment of Generators

Condition assessment aims to detect ageing before breakdown occurs. For generators, '*aging is not dominated by electrical stress but rather by the combination of different stress factors, of which thermal and mechanical wear are the most important.*' [4] The final breakdown, which is an electric failure, occurs due to material imperfections caused by ageing or introduced during the production. In generator insulation, critical imperfections include voids, cracks, delamination, resin accumulation, or damaged mica layers may play an important role [4].

Condition assessment of hydropower generators can be performed in several ways [5]: The DC insulation resistance can be measured offline and, similarly, the leakage current during online assessment. A reduced resistance can also be identified by a dissipation factor test. Air filled voids inside the insulation system generate PDs when the electric field is sufficiently high. These PDs can be detected in several ways: Online or offline electrical signals, by acoustic detection, visual detection of PD light, or by detection of the known PD by-product ozone or other marker species incorporated in the insulation. Different defects related to generator bars, such as internal discharges, slot discharges, endwinding discharges, and bar-to-bar discharges, show their typical phase resolved PD analysis (PRPDA), which are used as a fingerprint of the source type based on laboratory measurements in [6] (at 50 Hz). In some cases, therefore, it becomes possible to identify the defect that is causing PDs. A recent laboratory work performed a similar fingerprint study on different voltage frequencies [7], showing a minor frequency dependency in the overall PRPDA shape for different stator bar defects. The PD numbers, however, varied significantly with frequency. The results and trends were shown, but no explanation was given regarding the large variation in the number of PDs with voltage frequency.

PD measurements are usually calibrated, but calibration procedures are not intended for use in a large inductive apparatus [8], such as generators with a complex capacitive-resistive-inductive network. The PD pulses are damped and change shape after just a few windings. Because PDs are a symptom, rather than a root cause, it can be misleading to compare only measured number and magnitude of PDs, when the source is unknown. It is possible to detect PDs by using a different detection bandwidth and centre filter frequencies for noise reduction. Magnitude calibration is, however, possible only by PD

detecting systems operating at low frequencies (kHz range).

The picture in Figure 1.1 shows the stator windings of a hydropower generator with the rotor removed. It consists of more than 200 four-metre-long stator bars. Removing the rotor increases the test possibilities and enables for example, visual inspection of the windings or PD detection by an antenna for PD source localisation purposes.
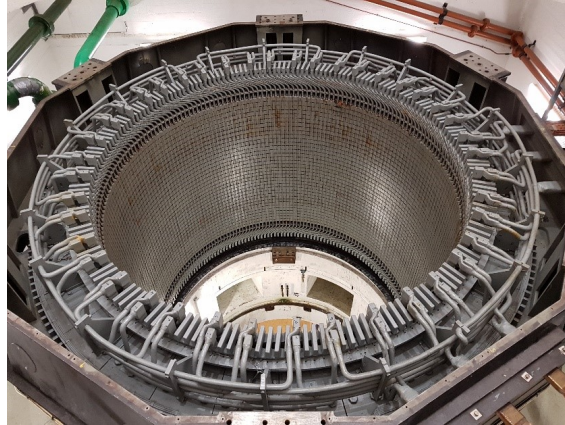
Figure 1.1: Photo of a hydropower stator when its rotor is removed. The generator bars are approximately 4 m long. Photo: Lars Lone, Hydro Energi.

Generators have a large capacitance to ground, typically between 0.5 μF to 3 μF. Test equipment for external voltage application as separate 50 Hz test transformers or 50 Hz resonant test equipment are heavy and costly compared to what is required for 0.1 Hz power sources. 0.1 Hz sources are usually portable on euro pallets, whereas 50 Hz sources typically require a large truck or a 40-foot container. However, results indicate that the PD results obtained from 0.1 Hz tests might significantly differ from those at 50 Hz. Thus, test results obtained at different voltage frequencies might not be directly compared [9].

In general, the temperature of the generator insulation varies with time and current load. The heating and cooling of generators is a slow process due to their large mass and high thermal heat capacity.

It is likely, therefore, that different condition assessment tests are performed at various voltage frequencies and under various test temperatures. To overcome this challenge, a better understanding of the relations between test conditions and measured results is needed. Particularly so with respect to explain the effect of the frequency and temperature on PD results from different types of defects in stator insulation.

1.2.2 Voids in Stator Insulation

It is likely that a considerable variation in the shape and dimensions of voids are present in the service-aged high-voltage insulation of hydropower stator bars [10], [11], and [12]. It is common to find delamination due to poor attachment between layers, or slot discharges, and voids in the epoxy. Delamination are typically characterised by a large area and a small void gap distance. The sketch in Figure 1.2 illustrates the various possible voids in stator insulation. The non-destructive tomographic technique has revealed that delamination and many small spherically shaped voids are present in a binder of polyester imide resin [13] and epoxy resin [14]. Similarly, cross-section microscope investigations of the bar cross-section has revealed delamination and voids [15]. Voids, delamination, and cracks have been found to produce similar PD behaviour, but with slightly different skewness in the PRPDA pattern [16].

Cross section of a generator bar
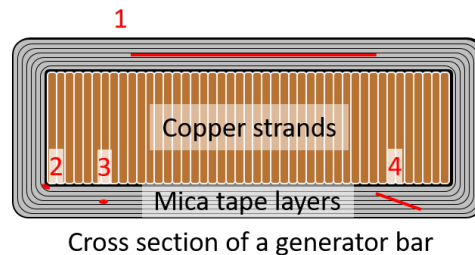
Figure 1.2: Sketch of typical voids in stator insulation systems: 1) delamination, 2) ellipsoid void in the high field region, 3) ellipsoid void in the main insulation, and 4) crack along more layers.

1.2.3 Modelling of Partial Discharge Test Results

The study by the Cigré working group A1.10 [3] reported that electric breakdowns of the main stator bar insulation system was the main source of generator failures. It is a common assumption that high PD activity is a precursor to electric breakdown. Fundamental knowledge of PDs from voids is needed to understand obtained PD test results during the assessment. In the literature, four major model approaches have been presented for describing the mechanisms of PDs [17]:

1. *The capacitive abc-model* [18] treats the different parts as capacitances and the PD event occurs when the voltage across the void collapses.

2. *The electrostatic dipole model* [19] treats the PD as a rapid change of the void dipole moment.

3. *The conductance model* [20] treats the PD event in a finite element method (FEM) model as a change in the void conductivity from a low to a high value during the

PD event. The discharge event is iteratively calculated.

4. *The plasma model* [21] treats the PD event in a FEM model with the involved gas discharge physics by using the plasma model in the void to represent the details of the PD event.

In a review article from 2005, dealing with the degradation of solid dielectrics due to internal PDs, Morshuis [22] concluded that there is a lack of knowledge of how the voltage frequency affected the PD activity. Since 2005, main contributions on the relation between voltage frequency and measurable quantities are performed by Cavallini et al. [23], Forssén et al. [24] [20], and Illias et al. [25], who experimentally have studied the PD of an air-filled void in polycarbonate and in epoxy resin. They used the conductance model and compared measured quantities to expected values from simulations, covering the voltage frequency range of 0.01 Hz to 100 Hz at ambient conditions. It was concluded, based on PRPDA results, that PD results from different voltage frequencies could not be directly compared. The maximum apparent charge decreased with frequency for the small 1 mm diameter spherical voids in [23][25], whereas increased with frequency for large cylindrical voids in [24]. This might indicate a void geometry dependence of PD amplitude. The PD amplitude distribution changed with voltage in [24], indicating that the PD mechanism are different at different voltages. Illias et al. curve-fitted the void surface conductivity, without physical explanation, to increase linearly with frequency, and 1 nS/m at 50 Hz, which is a high value, but not sufficiently high to change the electric field distribution from dominantly capacitive to resistive. These studies have shown that PD parameters change with voltage frequency and voltage magnitude. Only a qualitative explanation for the frequency dependence was given.

The experimental and theoretical focus in this thesis has, therefore, been to examine what factors affect measurable PD parameters of the insulation system. The internal PD event dynamics are, in fact, very fast and cannot be directly measured. PD analysis is, therefore, usually limited to examination of the external effect of rapid internal void discharge, that is, the impact of the total object. The measured PD signals occurring due to such rapid discharge is usually efficiently described using a capacitive abc-model, which is also the basis for modelling the PD signals in this thesis.

According to the typical textbook [18], the abc-model is based on four assumptions:

1. The electric field inside the void is homogeneous.

2. PD ignition[1] occurs when the voltage across the void reaches the breakdown strength of the void. Thus, there is no time delay between reaching this threshold voltage

---

[1]*Ignition* is here used as the start of the local PD event, whereas *inception* is used to describe the measurable event in the outer circuit.

and the start of the PD.

3. The complete electrode area of the void is discharged during the PD event. This area can be considered as an equipotential surface both before and after the PD event.

4. There is no decay of residual charges between each event of discharge.

The four fundamental assumptions for the abc-models are, however, not always valid:

1. The electric field inside the void is generally not homogeneous [26].

2. There is a time lag before the void breakdown [27].

3. The void discharge area is smaller than the total void area, only a fraction of the void is discharged during a PD event [28].

4. Remanent charges decay [10].

5. Void parameters may change with the duration of PD activity [29].

Test objects are generally voltage preconditioned to minimise the effect of time and PD-dependent void parameters. The capacitive abc-model should be used with care and its validity should be evaluated to assure proper use of it.

McAllister [30], Crichton et al. [31], and Boggs [32] discredit the capacitive assumption in the abc-model for spherical voids. They claim that the model capacitance of such geometry gives no meaning. It is not possible to measure capacitance in the spherical void and, therefore, the use of a corresponding capacitance in the model should be avoided. Only models that include electric field theory can give physical meaning. On the other hand, it is argued that the use of the abc-model, such as [33], who stated that '*the capacitive representation of cavities is a valid and powerful tool assisting engineers to analyse the transients related to space charges located within cavities inside the insulating material of any electrical equipment.*'

The capacitive model describes what can be measured as an electric signal in an external circuit. It has, therefore, still been studied in recent years and compared with numerical field calculations (FEM) including edge effects. In the case of a cylindrical void, it was found that at 50 Hz [34] both models give similar results. The abc-model, including resistive elements, has also been used to compare the measured effect of DC superimposed AC voltage on PDs in voids in a PET-film and found that the model described the measured results [35].

1.2.4 Results from Selected Experimental Examinations

Nair et al. [7] showed how phase-resolved PD analysis (PRPDA) changed for typical defects, such as internal voids, delamination, and slot discharges, in real stator bars as a function of applied voltage frequency. It was shown that the total of apparent charge per period increased for decreasing frequency, whereas the maximum apparent charge was found to increase with increasing power frequency. No models or physical theories were presented to explain this behaviour.

Niemeyer [36] and Gutfleisch [37] described a method of how to model PDs in voids embedded in a dielectric material. This includes field enhancement, initial electron generation by volume generation and surface emission, mechanisms of discharge propagation, and formation of remanent voltage due to surface charge accumulation. The effect of neither voltage frequency nor temperature was explored. The model included the breakdown process in the gas without the properties of the surrounding insulation material.

Other relevant articles have investigated the effect of a specific parameter that influences measurable quantities. Results obtained by Gjærde [38] indicate that the void pressure decreases as a function of time at test voltages well above PDIV. The decrease was only significant after tens of hours. The pressure was found to be quasi-constant with a pressure decrease of 0.2% for one hour. The pressure change is, therefore, expected to be insignificant during short PD tests. Hudon et al. [29] applied a voltage of 3.2 kV close to PDIV for 500 hours to a parallel plane air gap of 0.5 mm with the electrodes covered with 0.5 mm anhydride cured epoxy. The surface conductivity was measured and found to increase by 6 orders of magnitude during the first 100 hours of voltage application. It was later concluded that the increase in conductivity was caused by conductive PD by-products [39]. This change in surface conductivity takes time, as Levesque et al. showed in the case of slot discharges in generator bars kept for 1000 hours at twice the nominal voltage [40].

The capacitive abc-model requires that the complete void area (i.e., equivalent capacitance) discharges during each PD. Morshuis et al. [41] observed a distribution of light spots of PDs in cylindrical voids with a larger void diameter. This result indicates the existence of several PD occurring more or less simultaneously in a large void. Each discharging a fraction of the void surface only. The decay of surface charges on a plain epoxy surface has also been investigated by Kindersberger et al. [42]. Here, it was concluded that the decay of a surface charge on insulators is mainly due to three mechanisms: 1) electric conduction through the volume of the insulator 2) electric conduction along the surface of the insulator, and 3) charge neutralisation by gas ions. These residual charge decays were found to last for hours at room temperature. Hudon et al. [43] measured that the discharge current, that is, the total apparent charge in a void with one electrode surface

7

(slot discharges) increased with a factor of approximately 4 from 20 °C. to 155 °C. This is one of few works also studying the temperature dependence of the PD activity.

1.3 Main Goal and Selected Methodology

1.3.1 Main Goal

The literature survey revealed a lack of research contributions regarding the relations between measurable partial discharge parameters, the test voltage frequency and temperature.

As mentioned above, condition assessment can in practice be performed at different voltage frequency and test temperature. Morshuis [22] identified a lack of knowledge of how PD activity is affected by the voltage frequency. Forssén et al. [24] [20] and Illias et al. [25] claimed that no direct comparison between results obtained at 0.1 Hz and 50 Hz could be made based on experiments and simulations in cylindrical voids in polycarbonate and spherical voids in epoxy, respectively. The aim of the work presented in this thesis is to experimentally and theoretically examine relations between measurable PD parameters and voltage frequency and test temperature. An important part of this is to examine limitations of the classical capacitive abc-model and to test the validity of proposed modified model.

Experimental results are discussed with reference to proposed modified abc-model including conductivity and dielectric response. Tests were performed using laboratory object with cylindrical void inclusions and sections of service aged generator bars with unknown void size and number. The investigations were done by first developing the abc-model sufficiently to describe observed test results, then test at the cylindrical void with known geometry before comparing the model to the generator bar with unknown void size and number.

The main goal of this thesis is summarised by the following statement:

Explain frequency and temperature dependence of experimental PD results in a generator bar

1.3.2 Selected Methodology

The following methodology approach was selected to fulfil the main goal:

1. Conduct a literature review to provide a base for the examination.

2. To propose a modified and applicable PD model including the frequency and temperature dependent material parameters.

3. Experimentally examine the frequency and temperature dependence of PD parameters using laboratory-made reference objects with embedded cylindrical void.

4. Perform similar experimental PD examinations of short sections of service-aged generator bars containing many voids of unknown geometry.

5. Compare experimental results from both test objects to the proposed model. This should give insight to the similarity in the PD results from both objects and test the validity of the models used on both test objects.

6. Perform a study of the effects of preconditioning to verify that the test procedure produces similar void conditions at the different voltage frequencies.

A sketch of the involved test objects in this thesis are presented in Figure 1.3. The generator bars are taken from a hydropower generator, cut in shorter sections to reduce the capacitance of each test object. Results from these bar objects with voids of unknown size and number are compared to results from cylindrical voids with known geometry.
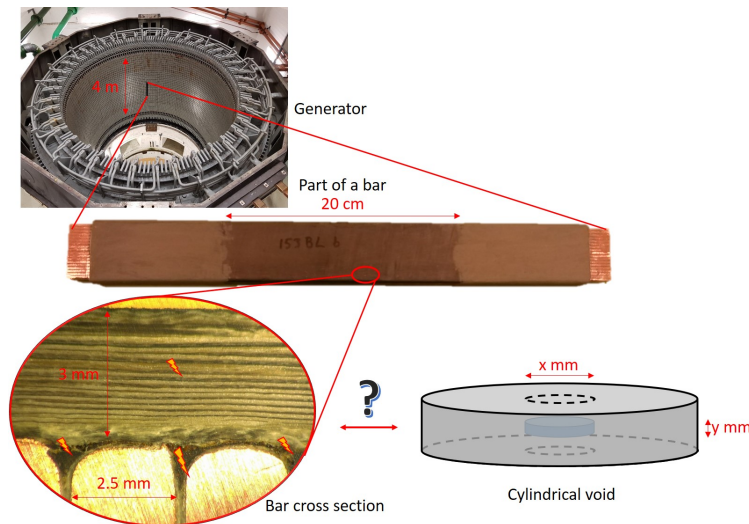
Figure 1.3: Overview of the different studied test objects in relation to condition assessment of hydropower generators in this work. The test objects include generator bars with unknown void size and geometry, and objects with known geometry.

1.4   Presentation of Data Points

Theoretical models predict continuous values as a function of frequency and temperature, whereas experimental data points are measured at selected combinations of those parameters. Some values are impossible to measure directly by common methods and are, therefore, estimated by using models and a curve fit to find the value. These data points are presented differently in this thesis:

1. *Theoretical* values are given either as a continuous or dotted lines, e.g. —and −−

2. *Measured* data points are given as open markers, e.g. ○, □ and △

3. *Estimated* data points are given as filled markers, e.g. ●, ■ and ▲

4. *Simulated* values are given either as a continuous or dotted lines, e.g. —and −−

The measured and estimated data points are often given with a dotted 'help' line (similar to the lines used for theoretical values), −○−, to increase the visibility of the trend.

The results from different test temperatures are assigned to a specific colour:

20 °C: ●, 40 °C: ●, 60 °C: ●, 90 °C: ●, 130 °C: ● and 155 °C: ●

Voltages are given as rms values unless otherwise is specified.

1.5   Publications Submitted during the Period of PhD Study

Overview of Publications

The findings of this PhD work have also been presented in the following six papers:

Torstein Grav Aakre planned, performed, and wrote all the papers included in this thesis. All co-authors contributed to discuss the results and paper.

Paper I

T. G. Aakre, E. Ildstad, S. Hvidsten, and A. Nysveen. Review of partial discharge and dielectric loss tests for hydropower generator bars. In *2017 Nordic Insulation Symposium (NordIS)*, volume 25, 2017.

This paper reviews the state of the art of various condition assessment methods for hydropower generators.

Paper II

T. G. Aakre, E. Ildstad, and S. Hvidsten. Condition assessment of hydrogenerator stator bar insulation using partial discharge measurements. In *Electrical Insulation Conference, EIC 2018*, 2018.

This paper presents results from PD measurements at variable voltage frequencies on various old generator bars.

Paper III

T. G. Aakre, E. Ildstad, and S. Hvidsten. Time development of voltage frequency dependence of partial discharge activity in voids. In *Nordic Insulation Symposium (NordIS)*, volume 26, 2019.

This paper describes the time development of the effect of preconditioning, that is, the temporary short-circuiting of the void.

Paper IV

T. G. Aakre, E. Ildstad, and S. Hvidsten. Partial discharge inception voltage of voids enclosed in epoxy/mica versus voltage frequency and temperature. *IEEE Transactions on Dielectrics and Electrical Insulation* 27(1): 214-221, 2020

This paper discusses variants of the impedance abc-model for describing the partial discharge inception voltage at different voltage frequencies and temperatures. The measured

dielectric response was shown important at 130°C and 155°C, and a high estimated void conductivity was shown important at temperatures below 90°C.

Paper V

T. G. Aakre, Erling Ildstad and S. Hvidsten. 'Partial Discharge Magnitude at Variable Voltage Frequency and Temperature of Voids in Stator Insulation.' Draft soon to be completed and submitted to: *IEEE Transactions on Dielectrics and Electrical Insulation*.

This paper discusses models for describing the apparent charge magnitude at different voltage frequencies and temperatures. The total apparent charge per period was shown frequency independent below 130°C, whereas highly influenced by residual charge decay caused by a high dielectric response at 130°C and 155°C.

Paper VI

T. G. Aakre and S. Hvidsten. Partial discharges in mainwall insulation of hydropower generator bars versus voltage frequency and temperature. Draft soon to be completed and submitted to: *IEEE Transactions on Dielectrics and Electrical Insulation*.

This paper describes if and how the presented models for one void in Paper IV and Paper V can be used on sections of generator bars (as was initially tested in Paper II). The models describe well the observed trends.

Additionally, a master student working with related topics resulted in a conference paper on limitations with the abc-model (Paper VII [44]), the content is, however, discussed more in detail in other papers and, therefore, not included in the thesis. Participation in online and offline PD measurements of an old hydropower generator was done, which also resulted in a conference paper (Paper VII [45]).

Paper VII: Paper not included in the thesis

T. G. Aakre, R. Skattenborg, and E. Ildstad. Limitations regarding use of the abc-model for interpretation of partial discharge measurements. In *2019 Nordic Insulation Symposium (NordIS)*, volume 26, 2019.

This paper discusses limitations with the commonly used capacitive abc-model.

This paper is based on experiments performed by the master work by Regina Skattenborg. Torstein Grav Aakre analysed the results, wrote the paper, and expanded on her work. Erling Ildstad participated in writing. All contributed to discuss the results and paper

Paper VIII: Paper not included in the thesis

E. Eberg, T. G. Aakre, G. Berg, and S. Hvidsten. Comparison of offline VLF pd measurements and online PD measurements on a 50-year-old hydrogenerator stator in Norway. In *Electrical Insulation Conference, EIC 2018*, 2018.

This paper discusses online 50 Hz vs offline 0.1 Hz PD measurements on a 50-year-old hydrogenerator stator. The focus is on pattern recognition.

Torstein Grav Aakre participated in the experimental work and discussions for the paper.

Chapter 2

Theoretical Model

Partial discharges (PDs) in electrical insulation occur in gas-filled voids that are exposed to a sufficiently high electric field. It is common to characterise PD activity in a test object by measurement of partial discharge inception voltage (PDIV), apparent charge magnitude, and number of discharges per voltage period. The PDIV is the lowest applied voltage at which PDs are detectable. The measured apparent charge is the charge needed to restore the voltage across the test object after a rapid discharge. The void voltage in AC systems is initially varying sinusoidally before any PDs occur. PDs create a residual charge voltage in a short time that opposes the applied voltage. This means that the total void voltage, including PD events, has a sinusoidal variation with steps at the PD events. This chapter first describes a model for the frequency- and temperature-dependent PDIV, then suggested models for the frequency and temperature dependence of apparent charge are presented.

2.1 Model for Frequency-Dependent Partial Discharge Inception Voltage

The common capacitive abc-model used to describe PDs is independent of voltage frequency [18]. The main contribution of the work presented in this thesis is to describe and evaluate a more general impedance model to describe a voltage frequency dependency. Different material modelling approaches are described, including resistance and dielectric response. Including dielectric response in the abc-model and later experimentally showing its importance is the main contribution in this thesis.

2.1.1 General Equivalent Circuit

The electrical properties of a dielectric material are generally characterised by its conductivity and frequency-dependent dielectric response. These properties can be represented by an impedance Z in an equivalent circuit. Generally, an insulation system containing a void is modelled as an equivalent circuit with the impedance abc-model, as shown in Figure 2.1. The impedance in the void is Z_c, the impedance in series with the void is Z_b, and the insulation in parallel with Z_c and Z_b is Z_a. The top and bottom of the void, representing the area in the equivalent capacitance of the section, are here called the ***void electrodes***.
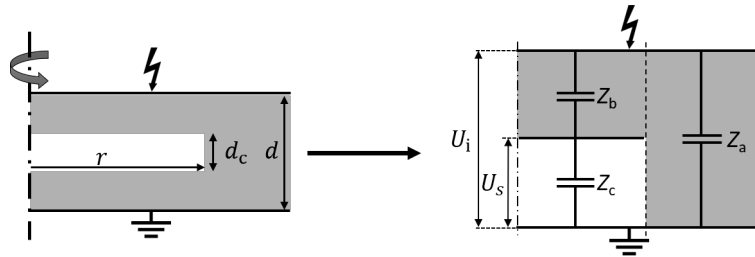
Figure 2.1: Sketch of the general equivalent circuit of an insulation system with a void. The air-filled void is represented by white, and the surrounding insulation is grey.

In a gas-filled void, PDs occur when the electric field becomes higher than the breakdown strength of the gas. In the case of homogeneous air-filled gap, the breakdown voltage follows the Paschen law for air, empirically given by

$$U_{\mathrm{s}} = 6.72\sqrt{pd} + 24.36pd + \frac{0.00411}{\sqrt{pd}} [\mathrm{kV_{peak}}], \tag{2.1}$$

which is based on experimental data for air gaps [18] and is valid for pressure p times distance d between 10^{-3} and 10^2 bar·cm.

The general relation between void voltage U_{void} and applied voltage U_{applied} for an electric circuit described in Figure 2.1 then becomes:

$$U_{\mathrm{applied}} = \left(1 + \frac{Z_{\mathrm{b}}(\omega)}{Z_{\mathrm{c}}(\omega)}\right) \cdot U_{\mathrm{void}}. \tag{2.2}$$

This equation can be used to find the expected PDIV U_{i} considering the void voltage U_{void} to be equal to the Paschen voltage U_{s}.

2.1.2 Estimates of PDIV for Different Impedance Models of Material Properties

As an example, the following reference test object was chosen with total thickness of 3 mm and a void gap distance of 0.5 mm. This type of insulation system is similar to the laboratory test objects used during the experimental examination described later. The presented models start with the common capacitive model, then describing the capacitive and resistive model, and finally introducing the capacitive and resistive model including dielectric response.

Selected material parameters used in the examples are listed in Table 2.1. Different subsets of the values were used for different models for material properties. The values were inserted into Equation (2.2) to illustrate the influence of the different material models on the measurable PDIV. In all models, the lowest breakdown voltage of the void is determined by Paschen law to $1.94\,\mathrm{kV_{rms}}$.

Table 2.1: Material properties derived from literature.

Parameter name	Symbol	Value	Unit	Reference
Mica/epoxy conductivity	σ_b	$2 \cdot 10^{-16}$	S/m	[46][1]
Insulation activation energy	E_a	0.70	eV	[47][2]
Air conductivity	σ_c	$10^{-16} - 10^{-13}$	S/m	[48]
Mica/epoxy permittivity	$\varepsilon_\mathrm{r}(\infty)$	3.94	1	[46][1]
Mica/epoxy permittivity	$\varepsilon_\mathrm{r}(\mathrm{DC})$	989	1	[46][1]
Polarisation relaxation time constant	$\tau(20°\mathrm{C})$	$1.3 \cdot 10^{15}$	s	[46][1]
Time constant activation energy	E_a	1.42	eV	[46][1]
Shape factor	α	0.71	1	[46][1]

[1] Based on data found in the reference
[2] Curve-fitted to data found in [47] in the temperature range 60 °C to 100 °C

Model 1: A Pure Capacitive Model

The pure capacitive model is the standard abc-model found in textbooks and often used as a first approximation in modelling of PD parameters, Figure 2.2a. The PDIV in the case of this pure capacitive model is

$$U_{\mathrm{i}} = \left(1 + \frac{d_{\mathrm{b}}}{d_{\mathrm{c}}} \cdot \frac{\varepsilon_{\mathrm{r,c}}}{\varepsilon_{\mathrm{r,b}}}\right) \cdot U_{\mathrm{s}}, \tag{2.3}$$

where $\varepsilon_{\mathrm{r,c}}$ and $\varepsilon_{\mathrm{r,b}}$ are the frequency independent relative permittivity of air and material, respectively. Thus, PDIV is frequency independent, as also indicated in Figure 2.2b.

(a) Model

(b) PDIV as a function of frequency.
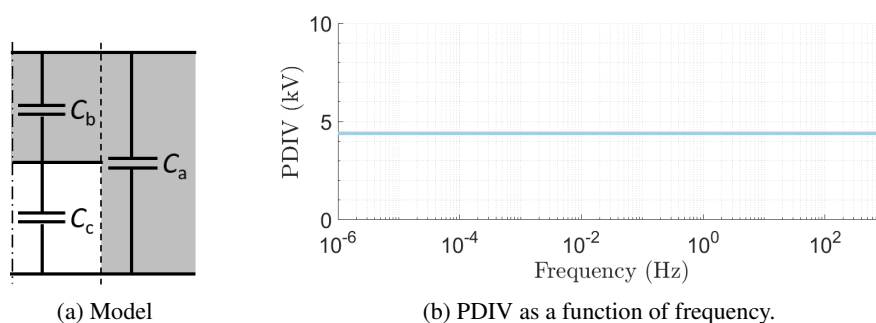
Figure 2.2: Capacitive model.

Model 2: Capacitive and Resistive Model

As a first modification, the effect of material conductivity is included in the model. The material DC conductivity is generally temperature dependent, and this dependence is here modelled by the common Arrhenius relation

$$\sigma_{\mathrm{b}} = \sigma_0 \exp\left(-\frac{E_{\mathrm{a}}}{k_{\mathrm{B}}T}\right), \tag{2.4}$$

where σ_0 is a constant, E_{a} is the activation energy, k_{B} is the Boltzmann constant, and T is the absolute temperature in Kelvin. The void is here considered to have a high resistance, due to a combination of high air resistance and void surface resistance. For simplicity, this combination is treated by the equivalent conductivity σ_{c}. It is common to assume that the void conductivity is close to zero and thereby neglect it; this was also done here.

The PDIV for the Model 2 in Figure 2.3a using a capacitance and resistance is

$$U_{\mathrm{i}} = \left(1 + \frac{d_{\mathrm{b}}}{d_{\mathrm{c}}} \cdot \frac{\sigma_{\mathrm{c}} + i\omega\varepsilon_0\varepsilon_{\mathrm{r,c}}}{\sigma_{\mathrm{b}} + i\omega\varepsilon_0\varepsilon_{\mathrm{r,b}}}\right) \cdot U_{\mathrm{s}}, \tag{2.5}$$

where σ_{c} and σ_{b} are the void and material conductivity, respectively. The combination of permittivity and conductivity results in a frequency dependent PDIV, as indicated in Figure 2.3b. At low frequencies, the high insulation conductivity short-circuits the insulation, resulting in low PDIV values. This case illustrates that PDIV is permittivity-dominated at high frequencies and conductivity-dominated at low frequencies.

(a) RC-model (1)

(b) PDIV as a function of frequency.
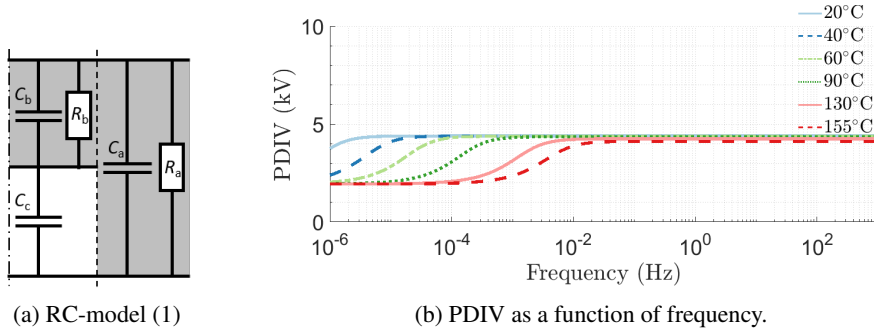
Figure 2.3: Capacitive and resistive model, neglecting void resistance.

Using this model, it is also possible to consider the effect of a certain void resistance R_c, Figure 2.4a. If the void conductivity increases of any reason, for example due to conductive PD by-products [29], the graph presented in Figure 2.4b illustrates that increased PDIV values are expected. It is demonstrated that the effect of increased void conductivity is to strongly increase the PDIV at low frequencies. The voltage across the void is expected to be low in the case of a high void conductivity and hence no PDs occur for the same applied voltage.

(a) RC-model (2)   (b) PDIV as a function of frequency.
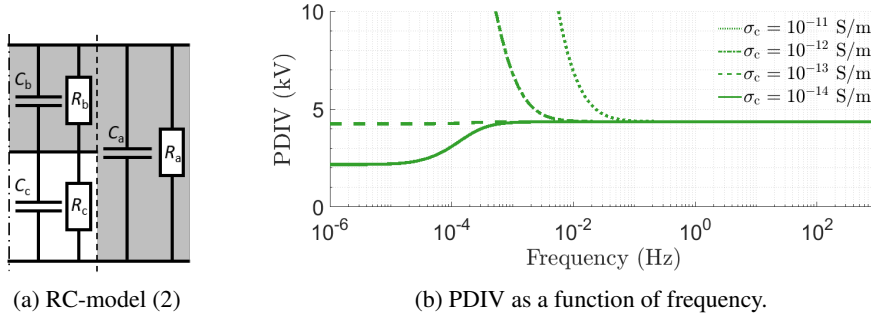
Figure 2.4: Capacitive and resistive model considering selected non-zero values of void conductivity. (Conductivity values selected at 90 °C with $\sigma_b = 4.1 \cdot 10^{-12}$ S/m)

From literature, it is expected that the void conductivity increases with the duration of PD activity. It is here assumed that such increase is time dependent with an exponential behaviour. Details behind this choice are found in Appendix A.3. It is assumed one behaviour when the high voltage is applied, and PDs are produced as

$$\sigma_c(t) = \sigma_{c,0} \cdot \left(1 - \exp\left(-\frac{t}{\tau_{PD}} \right) \right), \tag{2.6}$$

where $\sigma_{c,0}$ is a constant representing the equilibrium value and τ_{PD} a time constant related to the rate at which the void conductivity is changed. A similar relation is obtained for the situation after grounding of the object. Without PDs present, a different time constant τ_{GND} describes the rate of restoring:

$$\sigma_c(t) = \sigma_{c,0} \cdot \exp\left(-\frac{t}{\tau_{GND}} \right). \tag{2.7}$$

Model 3: General Impedance Model Including Dielectric Response

In this theoretical approach also the effect of dielectric response is considered in Figure 2.5a. The dielectric response of a material is a measure of dielectric loss by polarisation relaxation mechanisms. One mathematical description of dielectric response is the Cole-Cole model [49] of the complex permittivity. This is here considered to describe the dielectric response in general. The advantage is that the shape parameter α can be adjusted so many different materials can be described,

$$\varepsilon^* = \varepsilon(\omega = \infty) + \frac{\varepsilon(\omega = 0) - \varepsilon(\omega = \infty)}{1 + (i\omega\tau)^{1-\alpha}} = \mathrm{Re}(\varepsilon^*) - j\,\mathrm{Im}(\varepsilon^*), \qquad (2.8)$$

where $\varepsilon(\omega = \infty)$ is the permittivity at high frequencies, giving rise to capacitance in Z_{b}, $\varepsilon(\omega = 0)$ is the permittivity at low frequencies, ω is the angular frequency, the relaxation time constant τ is temperature dependent with an Arrhenius relation; $\tau = \tau_0 \exp\left(\frac{E_{\mathrm{a}}}{k_{\mathrm{B}}T}\right)$ [50] and the shape factor α varies between 0 and 1 describing the broadness of the relaxation. The Cole-Cole relaxation model is reduced to the Debye model if the shape factor $\alpha = 0$, equivalent to polarisation relaxation modelled by a capacitance in series with a resistance.

By inserting values in Equation (2.2), expected values of PDIV is given by

$$U_{\mathrm{i}} = \left(1 + \frac{d_{\mathrm{b}}}{d_{\mathrm{c}}} \cdot \frac{\sigma_{\mathrm{c}} + i\omega\varepsilon_0\varepsilon_{\mathrm{r,c}}}{\sigma_{\mathrm{b}} - \omega\varepsilon_0\,\mathrm{Im}(\varepsilon_{\mathrm{b}}^*) + i\omega\varepsilon_0\,\mathrm{Re}(\varepsilon_{\mathrm{b}}^*)}\right) \cdot U_{\mathrm{s}}, \qquad (2.9)$$

where $d_{\mathrm{b}} = d - d_{\mathrm{c}}$ is the insulation thickness and d_{c} is the void gap distance. PDIV as a function of frequency by including the dielectric response of the material is illustrated at different temperatures in Figure 2.5b. The temperature dependence is included by using a temperature dependent time relaxation $\tau(T)$ in Equation (2.8). In this case, the effect of dielectric response is dominating the effect of material conductivity, as seen in Figure 2.3.

(a) RC tanδ model(1)

(b) PDIV as a function of frequency.
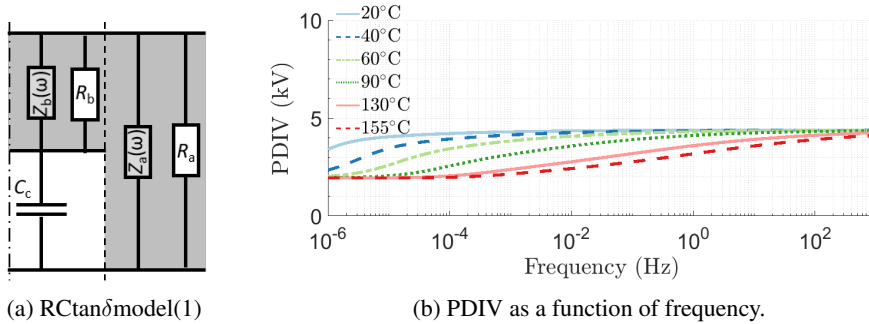
Figure 2.5: Capacitive and resistive model including dielectric response and neglecting void resistance.

The effect in this case of including a void conductivity, Figure 2.6a, is illustrated by the graphs presented in Figure 2.6b. Resulting in increased PDIV values, comparable to similar values of Model 2 at 90 °C shown in Figure 2.4b.
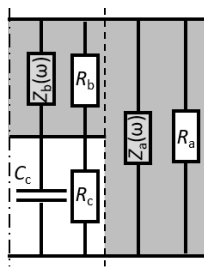
(a) RCtanδmodel(2)
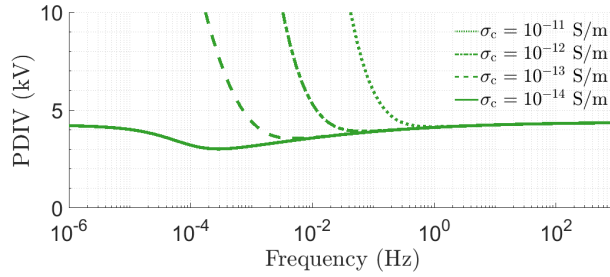
(b) PDIV as a function of frequency.

Figure 2.6: Capacitive and resistive model including dielectric response, considering selected non-zero values of void conductivity. (Conductivity values selected at 90 °C)

2.2 Estimating Apparent Charge Magnitudes

The void voltage and PDIV are described in the previous chapter, that is, the voltage distribution in the insulation system with a void before a PD occurs. The PD pulses are fast transients, that is, they consist of high frequencies, and the insulation system is, therefore, considered purely capacitive when performing calculations of PD parameters as measured in the outer circuit. The following description of apparent charge magnitude is, therefore, the same for all three abc-models.

2.2.1 The Basic Model

Residual charges are deposited at the void surface immediately after a PD. These charges create a residual voltage that opposes the externally applied voltage. This remanent void voltage is U_r and is of lower value than the breakdown voltage U_s. Previous examinations have estimated the electric field in breakdown channels in air to about 0.5 kV/mm [51]. The typical void voltage for two voltage periods is sketched in Figure 2.7. The sinusoidal void voltage without any PDs is presented as green in the graph and the void voltage including PD events is orange with a voltage reset to the remanent voltage U_r when a PD occurs when the voltage reaches ignition voltage U_s. The step graph in blue representing the residual charge voltage is, in this case, the difference between the other two curves.
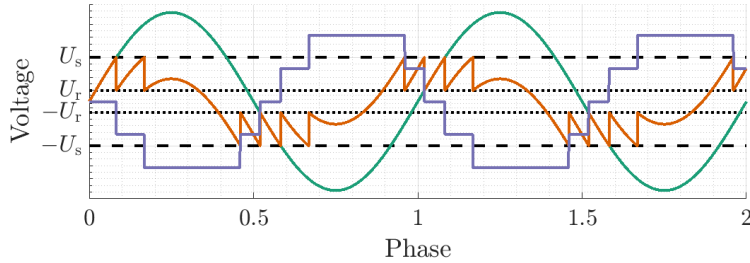
Figure 2.7: Sketch of voltage occurring across a void during sinusoidal application of voltage. The different curves represent void voltage (orange), void voltage without PDs (green), and residual charge voltage (blue).

The rapid voltage change $U_s - U_r$ during the PD event is measured as a current impulse. The apparent charge is defined as the charge needed from the external circuit to restore the voltage across the test object. This is given by

$$q_a = \left(C_a + \frac{C_c C_b}{C_c + C_b} \right) \cdot \left(\frac{C_b}{C_b + C_a} \right) \cdot (U_s - U_r) \approx C_b \cdot (U_s - U_r), \qquad (2.10)$$

where U_r is the remanent voltage after the PD event. This approximation is valid if $C_b << C_c$ or $(C_b \text{ and } C_c) << C_a$. The number of PD events during one voltage period is given

by

$$n = 2 \cdot \left\lfloor 2 \cdot \frac{U_0 - U_r}{U_s - U_r} \right\rfloor = 2 \cdot f(x), \tag{2.11}$$

where U_0 is the maximum applied voltage across the void in the case of no PDs and $f(x) = \lfloor x \rfloor$ the mathematical floor function, e.g. $\lfloor 2.7 \rfloor = 2$. Experimental results from [52] indicates that the floor function is omitted in real insulation systems, resulting in a straight line vs applied voltage U_0. Using this simplification and combining Equation (2.10) and Equation (2.11), the total measured apparent charge during a voltage period is expressed as

$$\sum q_a = n q_{a0} = 4 C_b \left(U_0 - U_r \right). \tag{2.12}$$

Example: The Apparent Charge at PDIV

Real and large insulation systems, for example a generator bar, is likely to contain many voids with different void gap distances. This example describes the expected apparent charge at PDIV as a function of PDIV with a void electrode area of $1 \ \mathrm{mm}^2$. The void gap distance is related to the PDIV value in a system with total thickness of 3 mm and are shown in Figure 2.8. The relation between void gap distance and PDIV (x-axis) is based on Equation (2.1) for Paschen law and the capacitive abc-model in Equation (2.3) for PDIV. The expected apparent charge magnitude is based on Equation (2.10). It is seen that in the case of an insulation thickness of 3 mm, the minimum PDIV is obtained at a void gap distance of 0.5 mm. The void gap distance of 0.5 mm is therefore used as the standard void gap distance in this thesis.
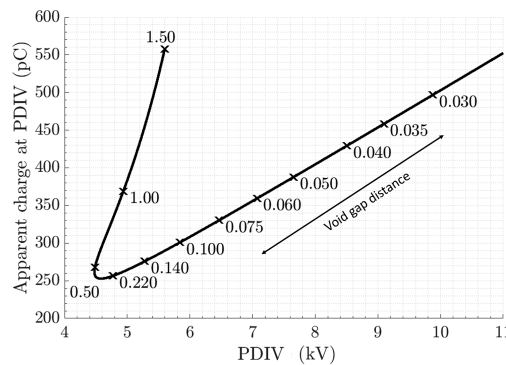
Figure 2.8: Expected apparent charge at PDIV as function of applied voltage. The different PDIVs correspond to indicated void gap distances (void gap distances at the graph is in mm). The void area is fixed at $1 \ \mathrm{mm}^2$ with $\varepsilon_r = 3.8$.

2.2.2 The Effect of Faster Void Voltage Restoration by Residual Charge Relaxation on the PD Repetition Rate

It is shown above that in the case of no relaxation of the deposited charge, the PD repetition rate is expected to follow the basic expression in Equation (2.11). It is, however, reasonable to assume that the deposited residual charges slowly decay due to surface conduction, recombination and diffusion through the void, or surrounding insulation bulk [42]. The voltage in the void U_0^* with n PDs occurring at time instant $t_{\mathrm{PD,i}}$ can then be modified to

$$U_0^* = U_0(t) - U_{\mathrm{q}} \sum_{\mathrm{i}=1}^{n} \exp\left(-\frac{t - t_{\mathrm{PD,i}}}{\tau}\right) \cdot u\left(t - t_{\mathrm{PD,i}}\right), \qquad (2.13)$$

where $U_0(t)$ is the sinusoidal void voltage without PDs, U_{q} the voltage from residual charges created in the PD events, which decay with a time constant τ, and $u\left(t - t_{\mathrm{PD,i}}\right)$ is the unit step function. The total void voltage is the superposition of the sinusoidal voltage and residual charge voltage from all PD events. Figure 2.9 presents a typical void voltage with a decaying residual charge.
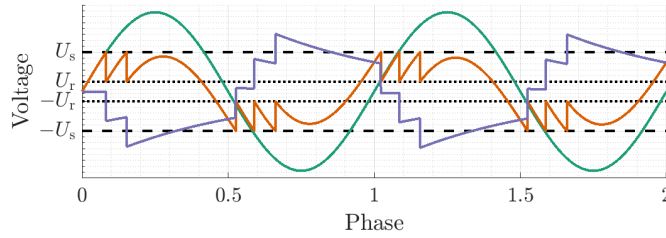
Figure 2.9: Sketch of voltage occurring across a void during sinusoidal application of voltage with residual charge relaxation. The relaxation time constant of residual charge voltage is equal to half the period. The different curves represent void voltage (orange), void voltage without PDs (green), and residual charge voltage (blue).

The residual charge relaxation time constant τ represents here the RC decay of residual charges, including a void resistance, insulation resistance, and dielectric response as sketched in the Thévenin equivalent of the charged void in Figure 2.10. The insulation in parallel, section a, is neglected because the capacitance C_a is much larger than C_b.
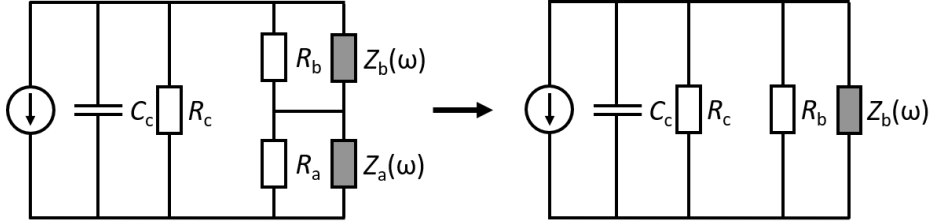

Figure 2.10: The Thévenin equivalent of the insulation system with a charged void (left). The contribution from section a is neglected due to the large capacitance C_a compared to C_b, which simplifies the circuit (right). $Z_a(\omega)$ and $Z_b(\omega)$ represent the dielectric response of the material. The charged void represented by a charged capacitance is decaying with time according to the circuit parameters.

The time constant τ in Equation (2.13) is frequency dependent when including dielectric response and is then given by

$$\tau = \varepsilon_0 \cdot \frac{\varepsilon_{\mathrm{rb}}(\omega) + \frac{d_\mathrm{b}}{d_\mathrm{c}}\varepsilon_{\mathrm{rc}}}{\sigma_\mathrm{b}(\omega) + \frac{d_\mathrm{b}}{d_\mathrm{c}}\sigma_\mathrm{c}}, \tag{2.14}$$

where ε_c is the relative permittivity of void air, and σ_c is the void conductivity. The material conductivity and dielectric response is here represented by a frequency-dependent resistance and capacitance in parallel, to enable the use of a permittivity $\varepsilon_{\mathrm{rb}}(\omega)$ and conductivity $\sigma_{\mathrm{rb}}(\omega)$ representing the insulation material.

2.2.3 The Effect of Variable Discharge Area

Considering the PDIV determined by the Paschen law, the magnitude of the apparent charge varies in accordance with the series capacitance C_b, which value is determined by the void electrode area involved in each discharge. In the case of a large void, the surface roughness and amount of remanent surface charge results in a variation of the surface potential of the voids. Thus, increasing the probability that just a fraction of the void electrode area is discharged during each PD. The presented model describes the case when the complete geometrical void electrode area discharges in each PD, whereas experimental results show that only a fraction of the void is discharge in each PD [41] [53].

The fractional discharge of the void electrode results in a high PD repetition rate n, and the magnitudes vary very much. This makes idealised equations based on a complete void

discharge difficult to use, and it is difficult to represent the apparent charge distribution with a single number. It is suggested, therefore, to use an estimator $\hat{n}$ to represent n to consider all PDs in one period instead of only single PDs. This estimator is defined by

$$\hat{n} = \frac{1}{q_{a0}} \cdot \sum q_a = x \cdot n, \qquad (2.15)$$

where q_{a0} is the theoretical apparent charge given by Equation (2.10) at Paschen voltage in the case of complete void area discharges, the total measured apparent charge per voltage cycle is $\sum q_a$, and x is the fraction of the void electrode area discharging during one voltage period. This means that the new estimator $\hat{n}$ is a measure of how many times the total void electrode area is discharged during each voltage cycle. The fundamental equation for the total apparent charge, Equation (2.12), is, therefore, used in this analysis. An important interpretation of this is that the void electrode area is not needed to discharge simultaneously to use the presented model equations.

2.2.4 The Effect of Statistical Time Lag on Ignition Voltage

Generally, PD inception requires that the voltage across the void is higher than the Paschen breakdown voltage and that a start electron is available to start an avalanche. The availability of start electrons is statistically described by a statistical time lag Δt. It has been suggested to have an exponential distribution [54]. A time lag is directly influencing the ignition voltage U_s, which can be higher than the values given by the Paschen law by

$$U_s = U_0 \sin \left(\omega \left(t_{PD} + \Delta t \right) \right) + U_{res}, \qquad (2.16)$$

where t_{PD} is the time the void voltage U_s is at the Paschen voltage U_s^0, U_0 is the maximum applied voltage across the void without any PDs occurring as found by Equation (2.9), and U_{res} is the voltage from residual charges from the previous PDs. A varying time lag produces a measurable effect as an overvoltage resulting in larger PD magnitudes. In the case of a completely discharged void electrode area, Figure 2.11 presents one example of such void voltage with an exponential distribution of time lags with Δt_0 chosen to be 5% of voltage period. The time lag is the time from when the voltage is at U_s to the PD event occurs (as a rapid voltage drop).
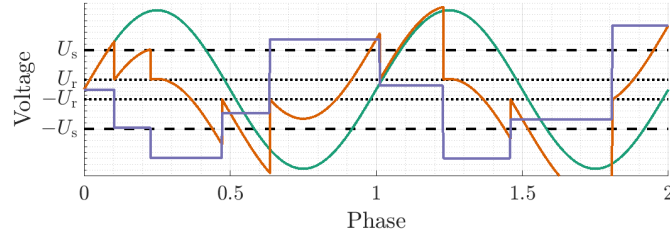
Figure 2.11: Sketch of voltage occurring across a void during sinusoidal application of voltage with a time lag present. The time lag follows an exponential distribution with Δt_0 chosen to be 5% of voltage period ($\propto \exp \Delta t / \Delta t_0$). The different curves represent void voltage (orange), void voltage without PDs (green), and residual charge voltage (blue).

The maximum theoretical ignition voltage U_s with a time lag longer than half a period is twice the maximum void voltage amplitude without PDs U_0, as it is possible to get residual charges creating a voltage of $U_\mathrm{res} = U_0$ from one PD. A frequency independent time lag gives rise to a frequency dependence of the maximum apparent charge, assuming $U_\mathrm{r} = 0$,

$$q_\mathrm{a,max} = C_\mathrm{b} \cdot (U_\mathrm{s} + (2U_0 - U_\mathrm{s}) \cdot f(\omega \Delta t)) , \qquad (2.17)$$

where the transition function $f(\omega \Delta t)$ between discharge voltage of U_s at low frequencies to $2U_0$ at high frequencies is here assumed linear in frequency until $\omega \Delta t = 1$, and above the unit function as a first approximation:

$$f(\omega \Delta t) = \min(\omega \Delta t, 1) . \qquad (2.18)$$

This is basically describing a frequency dependence between the low and high frequency limit. Appendix C presents a numerical comparison of Equation (2.16) and Equation (2.18).

The time lag is inversely proportional to the electron generation rate [37]. Volume ionisation is important before surface charges are deposited due to the first PD event after the electron generation rate is dominated by surface emission [36]. The electron generation rate from surface emission is increasing with a factor of about 10^5 from 20 °C to 155 °C by using the parameter values in [37].

Chapter 3

Research Questions and Hypotheses

This chapter presents the research questions (RQs) together with hypotheses (Hs) based on the presented literature survey and theoretical model. The research questions are ordered by the most important research question first, and then the less important questions succeeding. This is however opposite to the discussion order of the questions in this thesis because RQ3 and RQ2 are first needed to answer to be able to discuss RQ1 adequately.

Main Research Question:

RQ1 **Why are the measurable PD parameters PDIV, apparent charge and PD repetition rate different when applying a voltage frequency at power frequency (50 Hz) compared to very low frequency (0.1 Hz)?**

H1) PD parameters are frequency-dependent in the case of generator bar insulation.

H2) The insulation material conductivity and dielectric response function vary with temperature.

H3) The three presented abc-models are suitable to describe measured PDIV.

H4) The maximum apparent charge is frequency-dependent and can be modelled by a time lag.

H5) The PD repetition rate per period is frequency independent.

H6) PD parameters are dependent on the variation in void gap distance and void diameter.

Supporting Research Questions:

RQ2 **How can the measured PD parameters PDIV, apparent charge and PD repetition rate from generator bars be compared to voids with known geometry?**

H1) Only a fraction of the void electrode area discharges in each PD, but during a voltage period, the entire void electrode area is discharged.

H2) There is a correlation between measured PD parameters and void size and number in the test object.

RQ3 **What is the effect of preconditioning on measurable PD quantities?**

H1) Constant voltage application decreases the void resistance and, hence, the PD activity.

H2) The effect of constant voltage application vanishes with time after grounding the object.

H3) Preconditioning the test objects ensures similar start conditions for the different voltage frequency tests.

Chapter 4

Methods and Materials

4.1 Test Objects

Two different types of test objects were used: Laboratory objects with cylindrical voids and service aged generator bars. The number of parallel objects was 3.

The laboratory objects were made of assembled and cured commercially available resin-rich mica/epoxy/glass fibre tape (Samicatherm® 366.28-02) and named 'M'. The total laboratory object dimension was 100 mm × 100 mm × 3 mm. 9 tape layers were stacked half-overlapping to form a thickness of 1.5 mm (half the object thickness). The test objects were cured at 160 °C under pressure for one hour, and cooled to room temperature by air, according to the manufacturer's instructions. Cylindrical voids were created by a metal spacer in the curing process. Two cured sheets pressed together form a laboratory object.

Table 4.1 presents the void geometries used when making the laboratory objects. Figure 4.1 presents a sketch of the laboratory objects. The electrode diameter was 30 mm for all PD tests of laboratory objects. Laboratory objects M1 consist of voids with a diameter from 3 mm and up to 20 mm. The smallest void diameter was chosen to conform with the assumption of a homogeneous electric field, as discussed in Appendix A.1. The void in the laboratory objects M2 has a diameter of 80 mm and larger than the 30 mm electrode to study PDs without void walls in the high field region. The laboratory objects M3 are a modified version of M1, where copper tape covers the void top and bottom with and without thin wires connected to the outside. The thin copper wires enable a measurement of the void resistance. Laboratory object M4 is without voids, intended for dielectric tests and are 1 mm thick, except for the object tested for PD with a thickness of 3 mm.

The measurement of DC conductivity required aluminium electrodes evaporated to the surface of the laboratory object M4. The electrode diameter was 40 mm with a guard.

31

Table 4.1: Test object parameters for laboratory objects with cylindrical voids.

Parameter name	M1	M2	M3
Void diameter D (mm)	3, 5, 10, 15, 20	80	10
Void gap distance d_c (mm)	0.1, 0.3, 0.5, 0.75, 1.0	1.0	0.5
Void electrode - top and bottom	Insulating	Insulating	Metallic
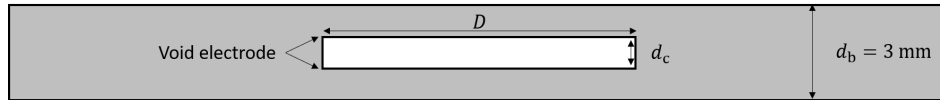
Figure 4.1: Sketch of test objects M1-3 with cylindrical void.

The generator bars used were taken from after 35 years in service (installed in 1970). Bars with three different service stresses were used: Back-up bars (GB1), service aged close to high voltage terminal (GB2), and service aged close to neutral terminal at ground potential (GB3). The insulation consists of resin-rich tape (MicaMat), and has a thickness of 3 mm. The rated ground voltage is $6.4 \text{ kV}_{\text{rms}}$. The generator bars were cut in 50 cm long sections. The total active length subjected to HV was 20 cm. The remaining length was covered by a commercially available field grading paint (CoronaShield® P 8001) at both sides. The generator bars used in tests to determine the dielectric response and DC conductivity had a 1 mm thick removal of the semi-conducting paint to form a guard to the field grading paint. The active test length was 20 mm, excluding the guarded area.

A summary of the different test objects are sketched in Figure 4.2.

Figure 4.2: Sketch [not to scale] and naming of the two test objects. Both test objects have sub objects with slightly different properties. Red/orange indicate metal.

4.2 Methods for Material Characterisation

4.2.1 Dielectric Tests

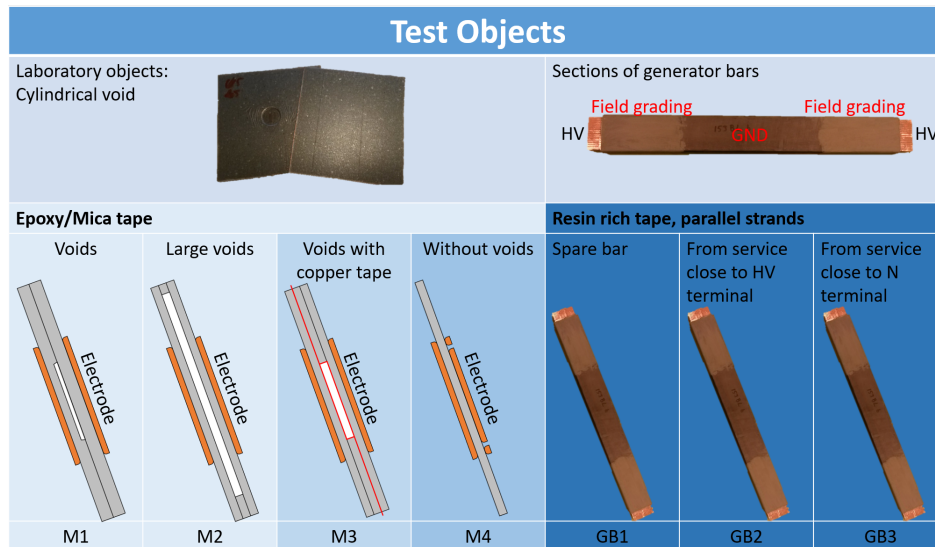The insulation in the two test object groups was characterised by dielectric spectroscopy in frequency domain, and DC conductivity. These parameters are used to compare the measured and estimated PD parameters.

The dielectric response was measured in the frequency domain. The frequency range was 10^3 Hz to 10^{-4} Hz at 200 V_{peak}. The temperatures were in the range of 20 °C to 155 °C. All measurements were performed using an IDAX 206 hardware and software.

The DC conductivity of the laboratory object M4 was measurement using an automated measurement setup, as described in [55]. A constant DC voltage in the range of 1 kV to 8 kV was used during the measurements. The temperatures used were 40 °C, 60 °C, and 90 °C. The DC conductivity of the generator bars with guard was measurement using a similar setup. The generator bars were tested in the DC voltage range from 200 V to 13.6 kV at room temperature (20 °C). The DC voltage for both test objects was applied for 2 h to measure the polarisation current before the objects were grounded for 20 h during which period the depolarisation current was measured.

4.2.2 Bar Cross Section Examination

One of each type of the generator bars (GB1, GB2, and GB3) were moulded into epoxy cylinders. All nine generator bars were then sectioned into twelve 1.5 cm sections each after performing the electric tests. Only three generator bars were moulded into epoxy because results from these objects did not show need for the extra epoxy support. The cross-sections of all sections were examined for voids with a microscope.

4.3 Partial Discharge Test Setup

The PD test setup is shown in Figure 4.3. The circuit is based on the 'direct test circuit' as described in for example IEC 60034-27 [56]. The test object was connected in parallel with a coupling capacitance. The voltage measure impedance was in series with the coupling capacitance (Omicron CPL 542 with PD output frequency range of 20 kHz to 6 MHz) and the data processing unit MPD 600. The voltage amplitude and frequency were set by a DAQ, and amplified 2000 times to high voltage by a TREK 20/20B in series with a RLC-low-pass filter with a cut-off frequency at 5 kHz. All test objects were completely placed inside a kitchen oven that controlled the test temperature. The voltage source, heat control, and data measurements were fully automated in LabView. The test procedure was based on the standard method from IEC 60034-27 [56] and IEEE 1434 [8].

1. DAQ – Producing voltage waveform
2. High voltage amplifier
3. Low pass filter
4. Oven with test object
5. Coupling capacitance
6. Battery driven PD detection unit
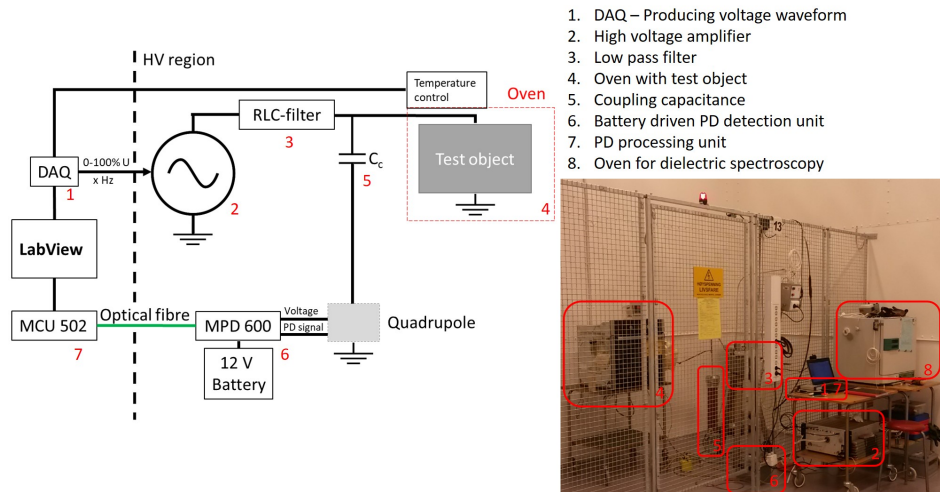7. PD processing unit
8. Oven for dielectric spectroscopy

Figure 4.3: Sketch and photo of the PD test setup.

To avoid correcting the measured apparent charge value, the following coupling capacitances were used: a) 100 pF for laboratory objects with capacitance of 20 pF, and b) 3.4 nF for the generator bar sections with capacitance of 400 pF.

The 'Rogowski' brass electrodes for the laboratory objects were moulded into epoxy and pressed together around the test object with a thin silicone grease layer in between. The electrodes were tightened until no more grease were squeezed out to minimise unintended voids between the brass electrode and test object. The electrode arrangement is shown in Figure 4.4.

1. Electrode
2. Test sample
3. Screw
4. Epoxy
5. Silicone grease
6. High voltage
7. Ground
8. Bakelite support
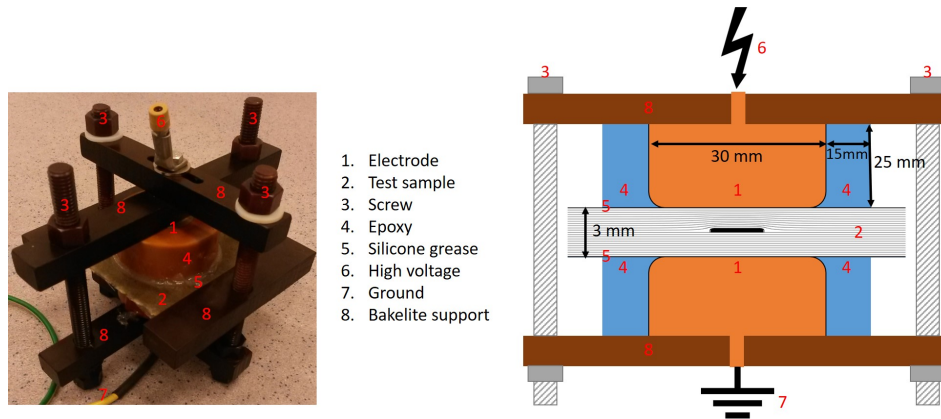
Figure 4.4: Sketch and photo of the electrode arrangement for M1 and M2.

Similarly, the ground electrodes for the generator bar sections were pressed to the semiconductive outer corona protection to simulate the stator slots. The electrodes for the sections of generator bars were pressed together to ensure good contact between the test object and ground electrode, as seen in Figure 4.5.
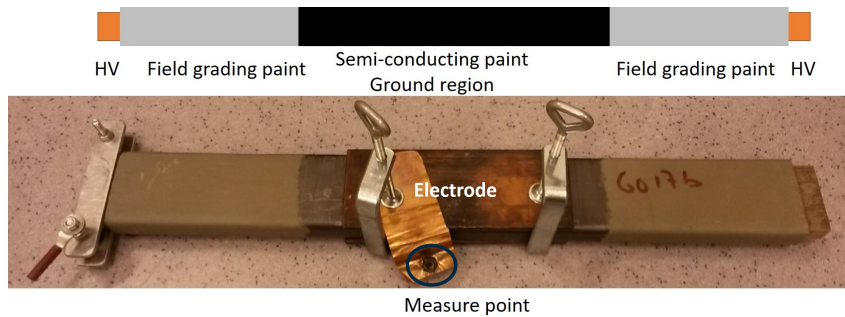
Figure 4.5: Sketch and photo of the electrode arrangement for GB1-3.

The frequency of the test voltage was varied in the range from 0.1 Hz to maximum 300 Hz. The upper frequency limit was determined by the capacitance of the test object and coupling capacitance. The test temperatures were in the range from room temperature to class F temperature (155 °C), which is the design temperature (one class higher than maximum service class temperature) of the insulation of the generator bars. The maximum test voltage was set to 1.5 times the rated ground voltage of the tested generator bar (10 kV$_{\text{rms}}$).

The setup was calibrated by injecting 100 pC by a calibrator across the test objects.

The PD magnitude detection region of the PD detection equipment covers a range of 1000. This means that a poor sensitivity is chosen if the equipment is chosen to detect large PD magnitudes. The maximum expected measured apparent charge is 78 nC by using Equation (2.10) with numbers from the maximum test void dimensions of $d_{\mathrm{c}} = 0.5$ mm and $D = 20$ mm, the corresponding Pachen voltage and $U_{\mathrm{r}} = 0$. Knowing that the void electrode of such large voids only fractionally discharges, the maximum detectable PD magnitude was fixed at 50 nC. This choice limited the sensitivity of the PD detection to 50 pC. The noise was measured to be below this sensitivity limit and thereby not described further. The PDIV is here measured in accordance with the definition in IEC 60270 [57], that is, the lowest voltage level that produces PDs above the threshold value of 100 pC. The threshold level was chosen higher than the sensitivity limit to not risk any PDIV from too small discharges compared to the expected discharge magnitude.

4.4 Test Procedures

4.4.1 Main Procedure of Voltage and Temperature Application

The voltage application procedure suggested in IEC 60034-27 [56] and IEEE std 1434 [8] was used as a baseline in this work. The stepwise alternative of voltage increase was chosen in this work and is sketched in Figure 4.6. The standardised procedure at 50 Hz starts with a preconditioning period at maximum test voltage for 5 minutes. Then, the test object is grounded before a stepwise increase in voltage to maximum test voltage and a stepwise decrease in voltage to zero voltage. The minimum step length is 10 s, and the minimum number of steps is 5 (10 steps are sketched here). This enables measurements of PDIV, apparent charge, and PD repetition rate.
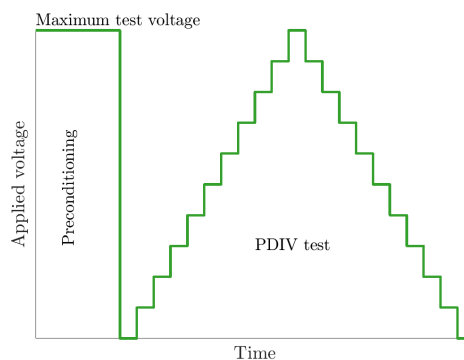

Figure 4.6: Sketch of the standardised voltage application procedure to measure PDIV, apparent charge, and PD repetition rate.

Several different voltage frequencies were tested in this work. A modification of the presented standardised test method was therefore needed. The purpose with the modification was to establish equal starting conditions for each test frequency. A frequency sweep modification was, therefore, established. The standardised test procedure was repeated at all test frequencies, with two modifications:

1. The preconditioning voltage frequency was 50 Hz. The length of the preconditioning was 5 min only before the first test, the other intermediate conditioning periods were reduced to 5 s.

2. The length of the voltage steps was the longest duration of 10 s and 10 voltage periods.

The intermediate conditioning was reduced to 5 s because the start conditions should remain the same during the frequency sweep. This 5 s voltage application also worked as a reference for PD parameters at 50 Hz. The minimum of 10 voltage periods was chosen in order to test many objects at different frequencies in a limited time.

The test frequency was varied in the range of 300 Hz to 0.1 Hz for the laboratory objects with capacitance of 20 pF and varied in the range of 50 Hz 0.1 Hz for the generator bar sections with capacitance of 400 pF. Measurements at 50 Hz were repeated after 0.1 Hz. Figure 4.7 presents the frequency sweep procedure for the laboratory objects.
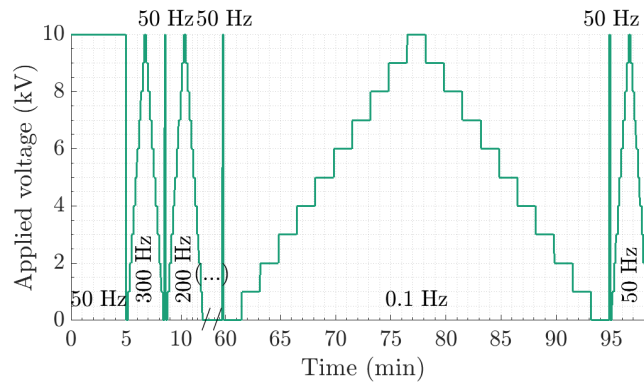
Figure 4.7: Sketch of voltage application procedure to measure PDIV and q_a in laboratory test objects.

The frequency sweep was finished at one temperature before heating the object and continuing at a higher temperature. The waiting time before PD measurement after change of oven temperature was 1 (2) hour(s) for test objects M1-2 (GB1-3). The temperature was varied in steps from 20°C via 40°C, 60°C, 90°C, 130°C, and ending at 155°C.

Four M1 laboratory objects were tested a second time to check if the frequency and temperature sweep had introduced permanent changes to the objects that influenced the PDIV.

4.4.2 Procedure of Voltage Application for Investigating the Effect of Voltage Preconditioning

The purpose of the previously presented voltage application procedure was to perform PD tests with equal starting conditions for each test frequency. The effect of the 5 min voltage application (preconditioning) was, therefore, studied in detail, both during voltage application and after grounding the test object. Additionally, an 1 h voltage application period was used to investigate the effect of a long voltage application time.

A maximum test voltage of 50 Hz and 10 kV was applied on three objects with electrode separation of 3 mm and void gap distance of 0.5 mm with a void diameter of 10 mm. The test was done at 20 °C, 40 °C, and 60 °C.

Assuming that PD activity influences the void condition, the PD test length must be kept at a minimum. Voltage frequency sweeps were, therefore, chosen to have 5 periods at each frequency of 50-10-1-0.1-1-10-50 Hz, equal to 35 voltage periods, which are likely to have a negligible effect on the void condition. Figure 4.8 presents a sketch of this voltage application with time. This choice of frequency sweep enables checking whether the first and second frequency tests are different. If they are not different, the frequency sweep did not influence the condition. Such frequency sweeps were distributed in time to show the time dependence.
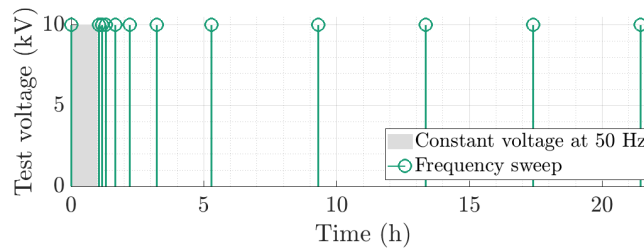
Figure 4.8: Sketch of voltage application procedure for studying the effect of voltage application. The procedure starts with a constant voltage application before object grounding and frequency sweeps are performed at selected time instants.

The void resistivity was measured at 1 kV DC before and after 1 h voltage preconditioning on the test object with metal void electrodes and metal wires (M3). A sketch of the electrode arrangement is presented in Figure 4.9. The voltage for PD application is applied between the brass electrodes, whereas the 1 kV from the DC insulation tester (Megger) is applied between point A and B. by using a DC insulation tester at 20 °C. This was done to examine whether the long voltage application affected the void resistivity.
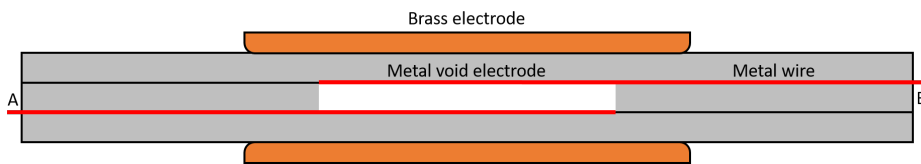
Figure 4.9: Sketch of test object M3 with metal void electrodes and thin wires to the outside (red). Voltage for PD application is applied to the brass electrodes, whereas the 1 kV DC insulation tester is applied between point A and B.

5

Chapter

Results from Laboratory Objects with Known Geometry

5.1 Material Characteristics

5.1.1 Material Conductivity of Laboratory Objects

Figure 5.1 presents the measured DC conductivity of laboratory-made test object M4 as a function of voltage and temperature. The conductivity was independent of the electric field range of 0.2 kV/mm to 5 kV/mm for the 1 mm thick object. The comparison to an Arrhenius relation in temperature resulted in the following parameters: $\sigma_{20°\mathrm{C}} = 5 \cdot 10^{-15}$ S/m and $E_\mathrm{a} = 0.44$ eV.

Figure 5.1: Measured DC conductivity as a function of inverse temperature at two electric field strengths. The test object was a 1 mm thick laboratory made sheet of glass fibre reinforced mica/epoxy tape (M4).

5.1.2 Dielectric Response of Laboratory Objects

The measured dielectric response with model fit as a function of frequency is presented in Figure 5.2 for the laboratory object M4. The real part of the permittivity incre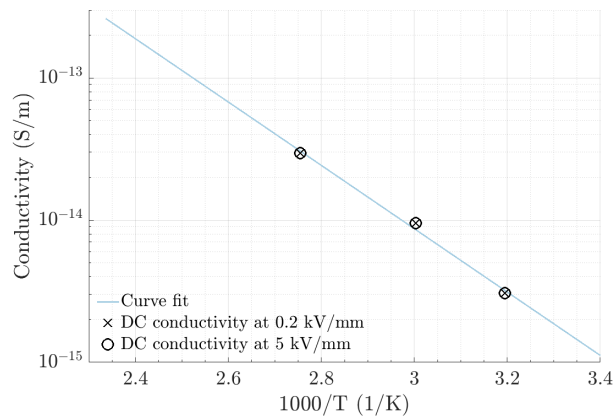ases with temperature at the lowest frequencies to high values. The results indicate that the imaginary part of the permittivity is increasing with a temperature-independent slope for lower frequencies. The dielectric response was here fitted to one Cole-Cole model, Equation (2.8), and Table 5.1 presents the best fit parameters by simultaneously fitting both the real and imaginary part of the permittivity.

Table 5.1: Curve-fitted numbers in the Cole-Cole model to measured complex permittivity.

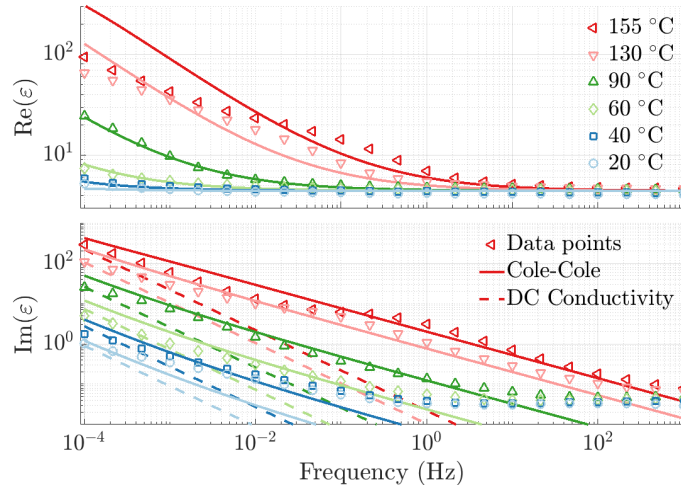| Parameter	Mica/epoxy tape	Unit
$\varepsilon(f = \infty)$	4.42	1
$\varepsilon(f = 0)$	940	1
τ_0	$7.4 \cdot 10^{-9}$	s
$E_{\mathrm{a}\tau}$	1.0	eV
α	0.42	1

Figure 5.2: Measured real and imaginary part of the permittivity as function of frequency at the indicated temperatures. The solid lines represent the Cole-Cole model using curce fitted values.

5.2   PD Inception Voltage of Laboratory Objects

Figure 5.3 presents measured PDIV as a function of frequency at the indicated temperatures for laboratory objects with a void diameter of 80 mm (M2) and 15 mm (M1). The results for void diameter of 15 mm are similar to those obtained for laboratory objects with void diameter of 10 mm and 20 mm. The main similarity between the two figures is the frequency independent PDIV at 60 °C and 90 °C, and a reduced PDIV at the combination of frequencies below 10 Hz and temperatures above 130 °C. The main difference between PDIV results from these two objects (M1 and M2) with large void diameter is that PDIV of M1 with void walls in the high field region at 20 °C and 40 °C are above 10 kV below 100 Hz. This is here modelled (solid lines) as a very high void conductivity in the impedance abc-model in Equation (2.9) based on measured dielectric response.
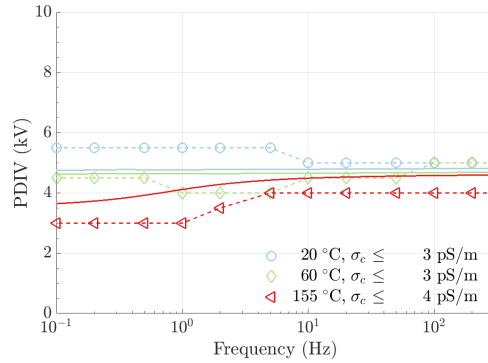
(a) Laboratory object M2 with a void diameter of 80 mm larger than the electrode with diameter of 30 mm.
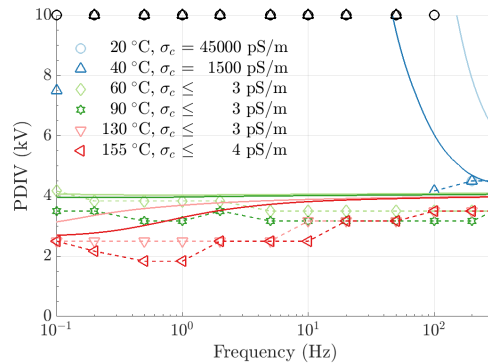
(b) Laboratory object M1 with a large void of 15 mm in diameter and void gap distance of 0.5 mm.

Figure 5.3: Measured PDIV as a function of frequency at indicated temperatures. The values are compared to an estimate based on the impedance abc-model (solid lines), including dielectric response and void conductivity σ_c. Black markers represents no measured PDs.

Figure 5.4 presents a similar graph as for the voids with large void diameter in Figure 5.3, with either a narrow void gap distance of 0.1 mm (Figure 5.4a) or a small void diameter of 3 mm (Figure 5.4b). Both geometries show an influence of the estimated high void conductivity in the impedance abc-model in Equation (2.9) based on measured dielectric response (Chapter 5.1.2). The estimated void conductivity for a void diameter of 3 mm is high at all temperatures, and thereby influencing the PDIV.
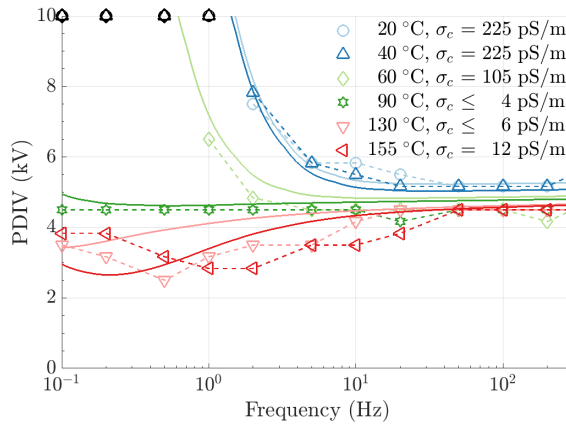
(a) Laboratory object M1 with a void of 10 mm in diameter and narrow void gap distance of 0.1 mm.

(b) Laboratory object M1 with a small void of 3 mm in diameter and void gap distance of 0.5 mm.

Figure 5.4: Measured PDIV as a function of frequency at indicated temperatures. The values are compared to an estimate based on the impedance abc-model (solid lines), including dielectric response and void conductivity σ_c. Black markers represents no measured PDs.

5.3   Distribution of PD Magnitude in Laboratory Objects

All the abc-models describe the case when the complete void electrode area discharges
during each PD event. The reality is that voids produce an apparent charge distribution.
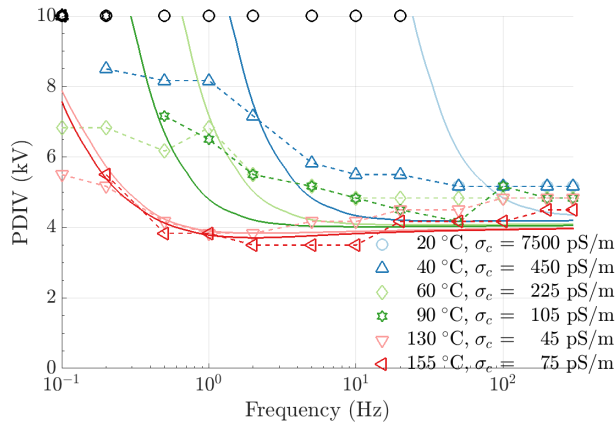This is illustrated in Figure 5.5 for the measured PD repetition rate per period as a func-
tion of measured PD amplitude. Three example test objects with void diameter of 10 mm
and void gap distance of 0.5 mm is presented. The measurements were done at 90 °C
and 50 Hz. The apparent repetition rate, indicated as coloured markers, are close to the
expected theoretical repetition rate n_0. The PD repetition rate per period for the three test
objects have a similar curve for the large PD magnitudes, whereas a larger spread for the
smaller PD amplitudes. The corresponding graphs for varying void diameter, tempera-
ture, voltage frequency, and voltage amplitude are comparable to the graphs presented in
Figure 5.5. These graphs are given in Appendix B.1.
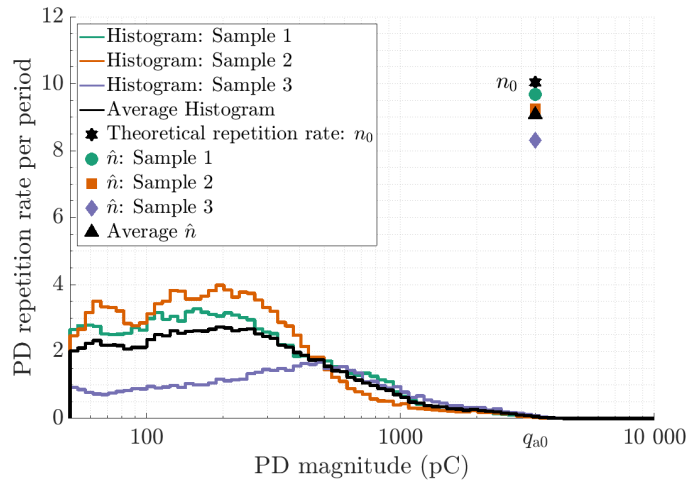
Figure 5.5: Measured PD repetition rate per period (histograms) as a function
of PD magnitude (solid lines) and expected PD repetition rate n_0 and apparent
repetition rate $\hat{n}$ for the same data (markers). Results were obtained at 90 °C at
50 Hz and 10 kV for three similar objects with void diameter of 10 mm and void
gap distance of 0.5 mm to show the reproducibility.

5.4 Distribution of PD Magnitude: Conductive Void Electrodes

The laboratory objects with equipotential void electrode surfaces (M3) have a behaviour similar to the other laboratory objects with insulating void electrodes (M1). This is presented in Figure 5.6, where both objects have a void diameter of 10 mm. The main difference between the two curves is that the objects with a void metal electrode have PD magnitudes around the expected value, whereas the objects with insulating void surfaces have a larger distribution.
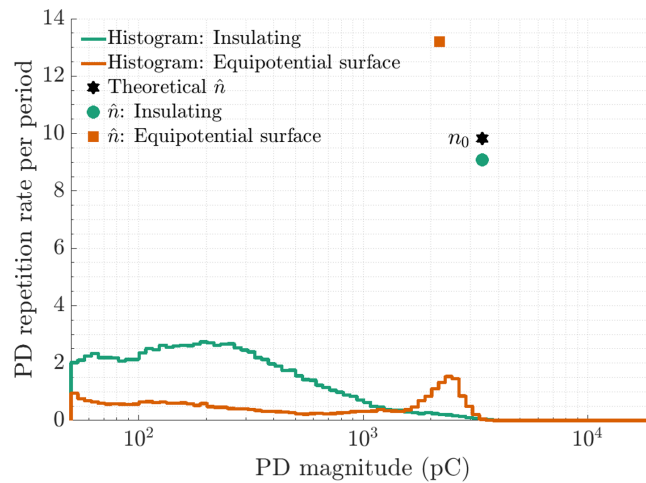
Figure 5.6: Measured PD repetition rate per period (histograms) as a function of PD magnitude (solid lines) and apparent repetition rate $\hat{n}$ for the same data (markers). Results were obtained at 90 °C and 10 kV at 50 Hz for objects with void diameter of 10 mm and void gap distance of 0.5 mm. Two laboratory objects with different void electrode surface are compared: an object with insulating surfaces (M1) and an object with equipotential surfaces (M3).

5.5 Maximum Apparent Charge in Laboratory Objects

Measured PD magnitudes are generally a distribution of magnitudes. The maximum measured apparent charge is often used as a measure on the PD activity. Figure 5.7 presents a typical example of measured maximum apparent charge as a function of estimated void voltage U_0 based on the impedance abc-model in Equation (2.9). The measurements in this example were performed on three test objects with void diameter of 10 mm at 90 °C, 10 kV, and 50 Hz. The measured trend was compared to Equation (2.10). The voltage dependency follows the same step function for all tested void geometries, temperatures, and voltage frequencies, but with a different amplitude as is shown in the next figures.
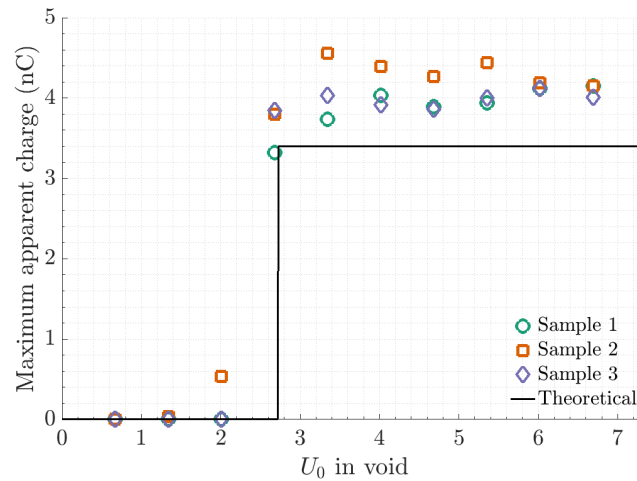
Figure 5.7: Measured maximum apparent charge as a function of voltage. The results were obtained at 90 °C for three similar objects with a void diameter of 10 mm at 50 Hz. The theoretical model is shown as a solid black line.

46

The temperature dependence of the maximum apparent charge at low frequencies is here
presented as a ratio between measured and expected numbers based on Equation (2.10)
in Figure 5.8. This choice neglects any influence of time lag and describes the simulta-
neously discharging void electrode area. The use of the ratio also enables a direct com-
parison between different void diameters as compared to the model. A value of 1 means
that the apparent charge is in line with the presented theory. All void diameters show an
increasing discharging void electrode area as a function of temperature. The largest voids
discharge only fractionally, whereas the two smallest voids seem to discharge 3-6 times
the actual void electrode area at 155 °C.
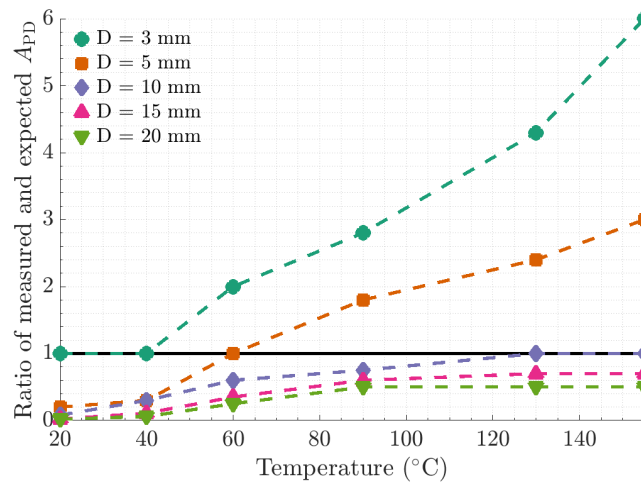
Figure 5.8: Ratio between measured maximum simultaneously discharged void
electrode area and the geometrical void electrode area as a function of temper-
ature. The results were obtained for laboratory object M1. The ratio of 1 is
indicated by a solid black line.

The smallest voids have a very high simultaneously discharging area at high temperatures.
Such large discharges can originate from noise from the test circuit, as was indicated in
the test without void in Appendix A.4. The objects with the smallest void diameters have
an expected low PD magnitude and are thereby more sensitive to such noise than the
objects with larger void diameters with higher expected PD magnitude.

The maximum apparent charge as a function of frequency at different temperatures and
the model in Equation (2.17) describing the effect of time lag on maximum apparent
charge are presented in Figure 5.9. The example is given for laboratory object M1 with
diameter $D = 10$ mm and a void gap distance $d_c = 0.5$ mm. There are two important
observations that can be made from these results:

1. The maximum apparent charge at temperatures below 90 °C is below the expected
   estimated value.

2. The maximum apparent charge is closest to the theoretical maximum value in the
   case of high test frequencies and high temperatures.
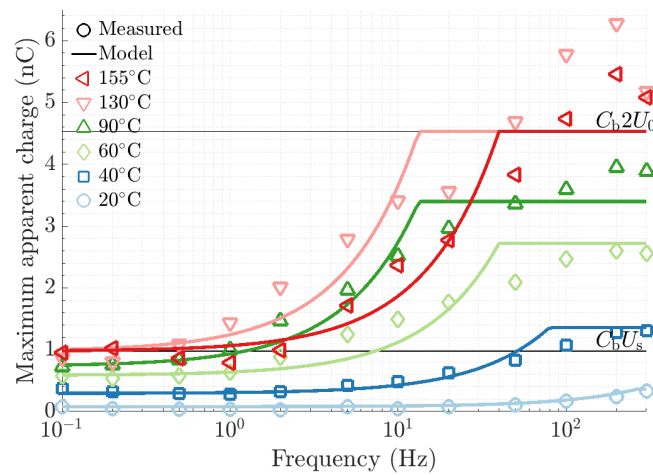
Figure 5.9: Measured maximum apparent charge as a function of frequency at in-
dicated temperatures. The measured values are compared to the model in Equa-
tion (2.17). Results are obtained for laboratory object M1 with a diameter of
10 mm and a void gap distance of 0.5 mm. The horizontal solid black lines rep-
resent the expected apparent charge for the cases when the void voltage is U_s and
$2U_0$.

5.6 Total Apparent Charge in Laboratory Objects

The total apparent charge per period is here presented and considered as a relevant quantity because PDs in a void are occurring with a magnitude distribution. Figure 5.10 presents a typical example of measured total apparent charge per period as a function of estimated void voltage U_0 based on the impedance abc-model in Equation (2.9). The measurements in this example were performed on three test objects with void diameter of 10 mm at 90 °C, 10 kV, and 50 Hz. The measured trend was compared to Equation (2.12). The measured total apparent charge per voltage period for all frequencies and temperatures and void dimensions follow the straight line versus voltage as is shown in Figure 5.10. Using this approach, it might also be possible to indicate estimated values of the capacitance C_b and the remanent voltage U_r.

Figure 5.10: Measured total apparent charge as function of voltage. Results are obtained for three similar objects and compared to the model fit of Equation (2.12). The void diameter was 10 mm and a void gap distance was 0.5 mm. The two cases with zero remanent voltage and remanent voltage equal to the Paschen voltage are indicated by dotted lines.

The measured total apparent charge per period as a function of frequency is presented in
Figure 5.11. The measured values are compared to a model including the increased PD
repetition rate given by Equation (2.13), caused by increased residual charge relaxation.
The purpose in this figure was to focus on the frequency dependency of total apparent
charge. The PD repetition rate in the model was therefore fixed at the value at 300 Hz,
and hence not including effects in the model that are temperature dependent and fre-
quency independent. The important model parameters are given in Table 5.2. The residual
charge relaxation time constant is, in addition to the estimated void conductivity, based on
measured dielectric response (shown in Chapter 5.1.2) inserted into Equation (2.14), and
shown in Figure 5.12. No frequency dependence of total apparent charge was observed
below 100 °C.

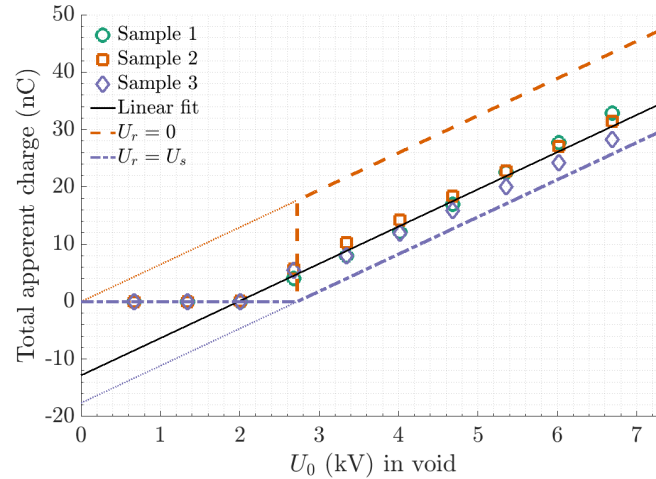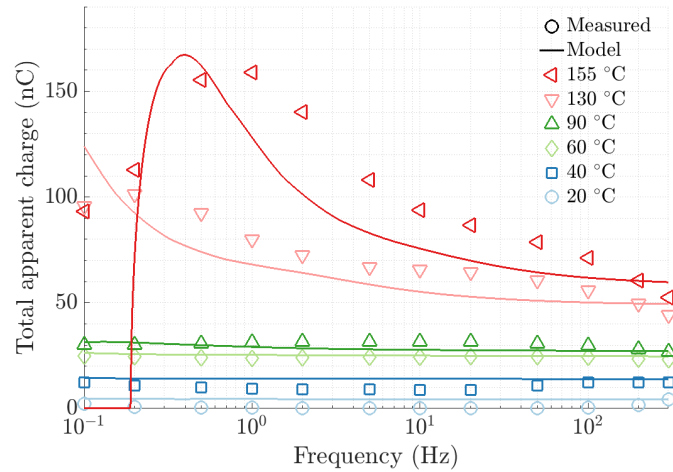

Figure 5.11: Measured total apparent charge per period as a function of fre-
quency. The measured values are compared to the model for total apparent
charge, based on the increased PD repetition rate found by using Equation (2.13).
The estimated values are based on measured dielectric response and calculated
void conductivity. Measured results were obtained for laboratory object M1 with
a void diameter of 10 mm and void gap distance of 0.5 mm.

Table 5.2: Residual charge relaxation parameter values. The insulation material
conductivity (b-values) were measured directly. The curve fit is comparable for
all void diameters, slightly varying τ and σ_c, when fixing the value at 300 Hz.

Parameter name	$\sigma_{\mathrm{b}}(20°\mathrm{C})$	E_{ab}	$\sigma_{\mathrm{c}}(20°\mathrm{C})$	E_{ac}
Unit	S/m	eV	S/m	eV
Value	$5 \cdot 10^{-15}$	0.44	$8.9 \cdot 10^{-15}$	0.9
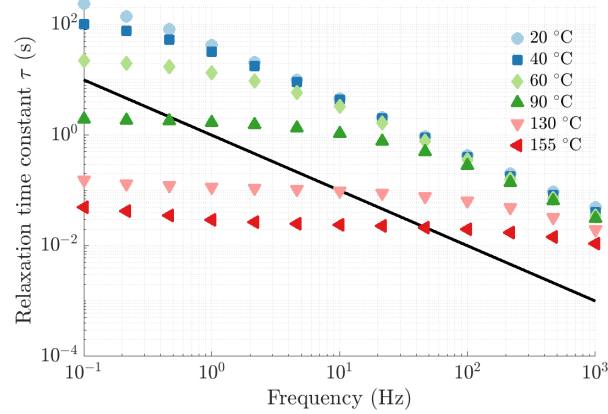
Figure 5.12: Calculated relaxation time constant as a function of frequency at indicated temperatures. The values are based on Equation (2.14) with the measured dielectric response and calculated void conductivity for the curve fit in Table 5.2. Values below the solid black line are time constants lower than the voltage period where relaxation is influencing the test results.

The measured total apparent charge is increasing with temperature and shown in Figure 5.13. Values at 300 Hz were chosen to neglect the increased PD repetition rate at low frequencies as shown earlier in Figure 5.11. The expected value based on Equation (2.11) is indicated by a black square marker. Measured results were obtained for laboratory object M1 with a void diameter of 10 mm and void gap distance of 0.5 mm, and other void geometries show a similar temperature dependency.
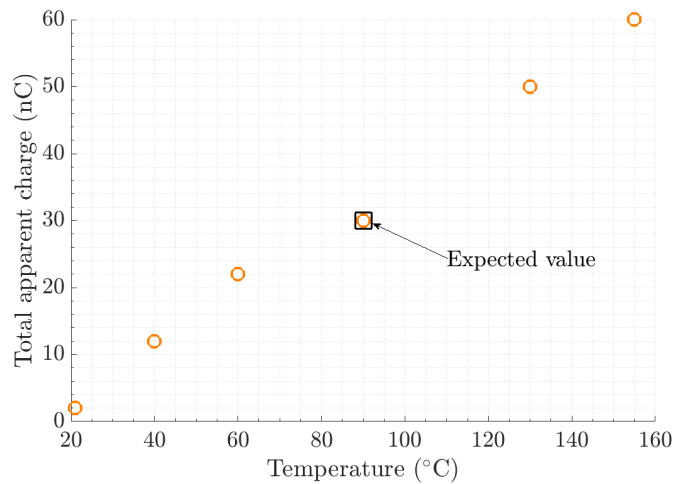
Figure 5.13: Measured total apparent charge per period at 300 Hz as a function of temperature. Measured results were obtained for laboratory object M1 with a void diameter of 10 mm and void gap distance of 0.5 mm. The expected value for a completely discharged geometrical void electrode is indicated.

Figure 5.14 presents the measured total apparent charge as a function of void diameter at indicated temperatures at 50 Hz. The measured total apparent charge at 90 °C follows the model for void diameters up to 15 mm. The PD activity for a test object with void diameter of 20 mm is lower than expected. The general temperature trend presented in Figure 5.13 for void diameter of 10 mm can also be found at all void diameters.
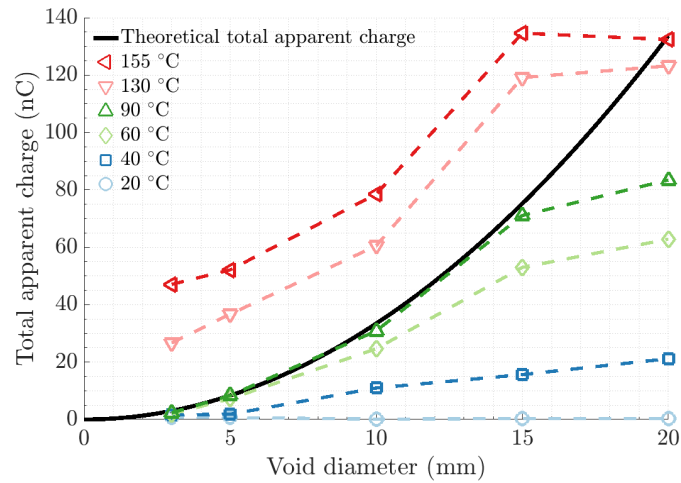
Figure 5.14: Measured total apparent charge per period as a function of the void diameter for indicated temperatures. The theoretical estimate is indicated as a solid black line.

Results from Service Aged Generator Bars

6.1 Material Characteristics

6.1.1 Material Conductivity of Generator Bar Insulation

The measured DC conductivity of sections of generator bar objects with a mechanical guard are presented in Figure 6.1. Three objects were measured as a function of voltage and measured only at room temperature (20 °C). The maximum voltage of 14 kV is equal to a field strength in the straight sections of 4.67 kV/mm with an insulation thickness of 3 mm. The conductivity is in the ohmic region from 0 to 8 kV. There is hardly any difference between the three different bar types. The conductivity in the generator bars at room temperature is about 50 times lower than in the laboratory object presented in Figure 5.1.
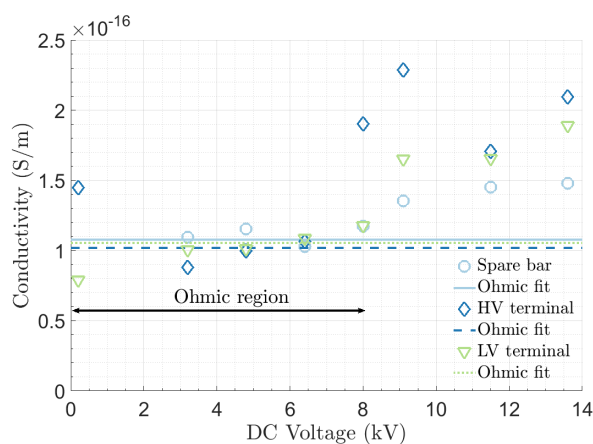
Figure 6.1: Measured DC conductivity as a function of applied voltage measured at room temperature of 20 °C for the three generator bars.

6.1.2   Dielectric Response of Generator Bar Insulation

The measured dielectric response with model fit as a function of frequency is presented in
Figure 6.2 for one generator bar. The real part of the permittivity increases with tempera-
ture at the lowest frequencies to high values. The results indicate that the imaginary part
of the permittivity is increasing with a temperature-independent slope for lower frequen-
cies. The dielectric response was here fitted to one Cole-Cole model, Equation (2.8), and
Table 6.1 presents the best fit parameters by combining both the real and imaginary part
of the permittivity. The results are similar for the other bars and, therefore, not included.
The dielectric response from bar sections and laboratory objects differ only slightly. The
influence from measured DC conductivity is negligible.

Table 6.1: Curve-fitted numbers in the Cole-Cole model to measured complex
permittivity.

Parameter	Mica/epoxy tape	Generator bar	Unit
$\varepsilon(f = \infty)$	4.42	3.79	1
$\varepsilon(f = 0)$	940	941	1
τ_0	$7.4 \cdot 10^{-9}$	$8.8 \cdot 10^{-9}$	s
$E_{a\tau}$	1.0	1.0	eV
α	0.42	0.49	1
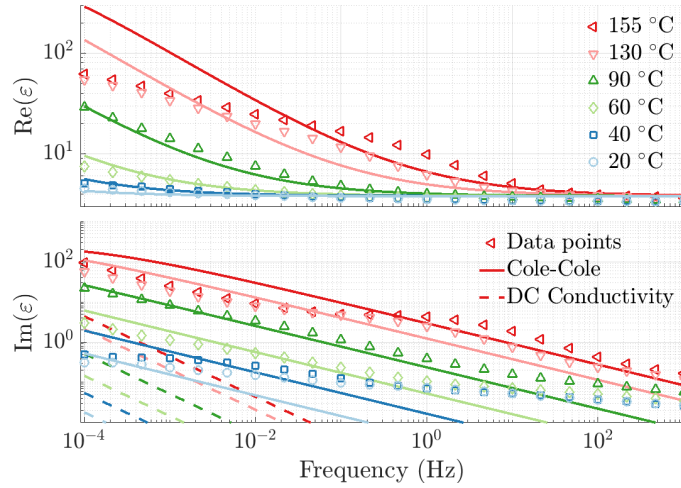
Figure 6.2: Measured real and imaginary part of the permittivity as function of
frequency at the indicated temperatures. The solid lines represent the Cole-Cole
model using curve fitted values.

54

6.2 PD Inception Voltage of Generator Bar Sections

Figure 6.3 presents the PDIV for the different generator bar types, GB1, GB2 and GB3, as a function of frequency for the indicated temperatures. The results were compared to the impedance abc-model with measured dielectric response (Chapter 6.1.2). The PDIV is frequency independent at temperatures below 90 °C. There are no significant differences between the different generator bar types.
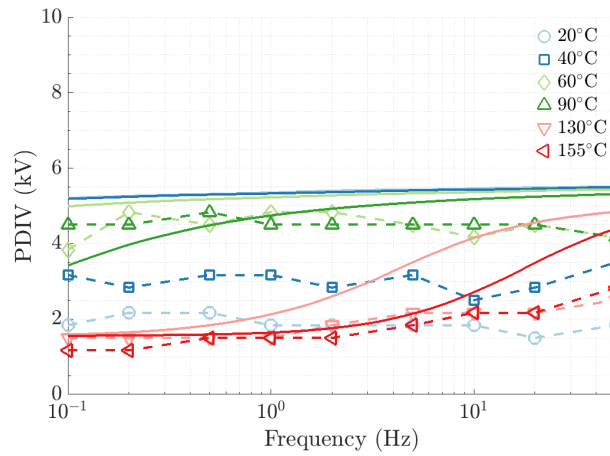
(a) Back-up bar objects (GB1)
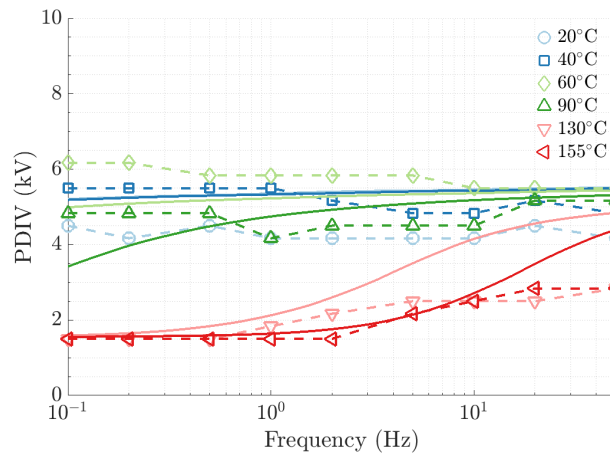
(b) Bars from close to high-voltage terminal (GB2). The graph for bars from close to neutral terminal (GB3) is similar.

Figure 6.3: Measured PDIV as a function of frequency at the indicated temperatures. The curve fits used ($d_{c} = 0.3$ mm) in the impedance abc-model.

6.3   Distribution of PD Magnitude in Bar Sections

The measured distribution of PD repetition rate per period for three bars from close to the neutral terminal are presented in Figure 6.4 at 50 Hz, 90 °C and 10 kV. Similar results were obtained for the other bar objects and, therefore, are not included here. The apparent charge magnitudes are comparable for the three similar objects. Many small magnitudes combined with a few large are typical for void discharges and the distribution is as expected from the literature. The corresponding graphs for varying temperature, voltage frequency, and voltage amplitude are comparable to the graphs presented in Figure 6.4. These graphs are given in Appendix B.2.
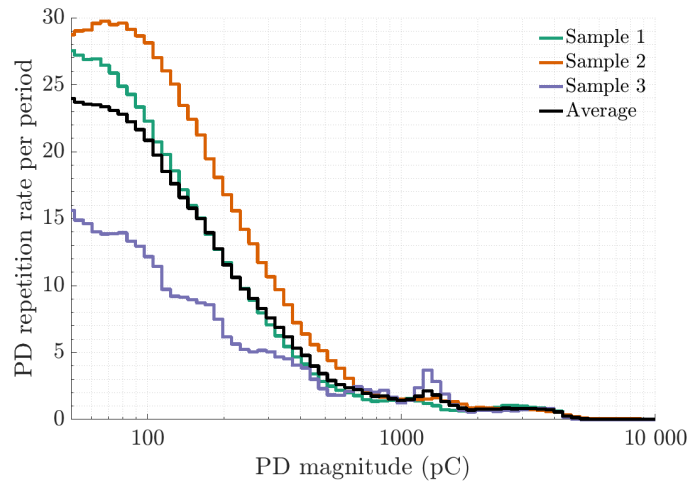
Figure 6.4: Measured PD repetition rate per period as a function of PD magnitude. Results were obtained at 90 °C at 50 Hz and 10 kV for three similar objects close to neutral terminal to show the reproducibility.

6.4   Maximum Apparent Charge in Bar Sections

Figure 6.5 presents a typical example of measured maximum apparent charge as a function of applied voltage. The measurements in this example were performed on one bar from close to high-voltage terminal at 90 °C, 10 kV, and 50 Hz. The measured trend was compared to Equation (2.10). This figure is highly representative as most of the corresponding graphs at different temperatures, frequencies, and bars are qualitatively equal. The maximum apparent charge increases with voltage.

The deviation from a step function in maximum apparent charge indicates that more void gap distances are present or that a larger fraction of the void discharges simultaneously at higher voltages.

Figure 6.5: Measured maximum apparent charge as function of voltage. Results were obtained at 90°C and 50 Hz for the bars close to high voltage terminal. The model is based on one void. The remant voltage is assumed zero becuase variations are difficult to distinguish from the capacitance C_{b}.

Figure 6.6 presents the maximum apparent charge as function of frequency for one typical bar close to the high-voltage terminal, together with a curve fit to the model. The measured maximum apparent charge was curve fitted to Equation (2.17) by finding the optimal time lag. Table 6.2 lists the relevant parameters. The fraction between maximum voltage and initiation voltage U_0/U_s is temperature independent and corresponds to a PDIV of 6 kV.

Table 6.2: Calculated parameters for three temperatures in Figure 6.6 for time delay as a function of frequency for test object HV terminal GB3(2).

Parameter	20 °C	60 °C	155 °C
$C_b U_s$	$0.54 \cdot 10^{-9}$	$1.08 \cdot 10^{-9}$	$2.16 \cdot 10^{-9}$
$C_b 2 U_0$	$1.8 \cdot 10^{-9}$	$3.6 \cdot 10^{-9}$	$7.2 \cdot 10^{-9}$
U_0/U_s	1.67	1.67	1.67
$\Delta t(\mathrm{ms})$	5	5	20
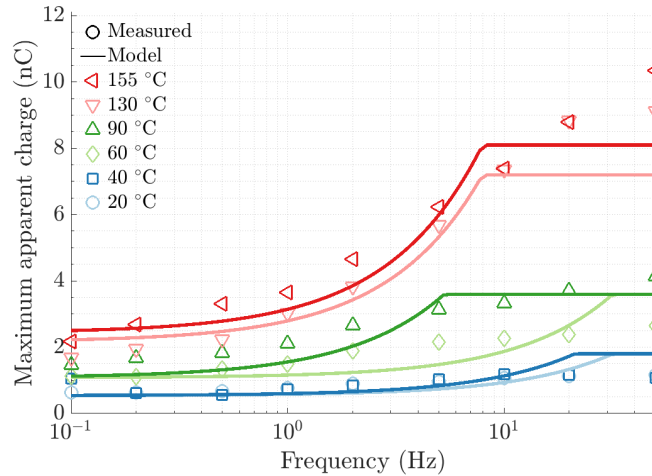
Figure 6.6: Measured maximum apparent charge as function of frequency at indicated temperatures. The measured values are compared to the model in Equation (2.18). Results were obtained using one bar close to neutral terminal at 50 Hz and 10 kV. The overall trends are comparable between the different bars.

6.5 Total Apparent Charge in Bar Sections

The total apparent charge as a function of voltage is predicted by Equation (2.12). Figure 6.7 presents one example taken from measurements at 90 °C at 50 Hz for one bar close to the high-voltage terminal. This figure is highly representative as most of the corresponding graphs at different temperatures, frequencies, and bars are qualitatively similar. The total apparent charge as a function of voltage is a straight line in accordance with the theory for one void.
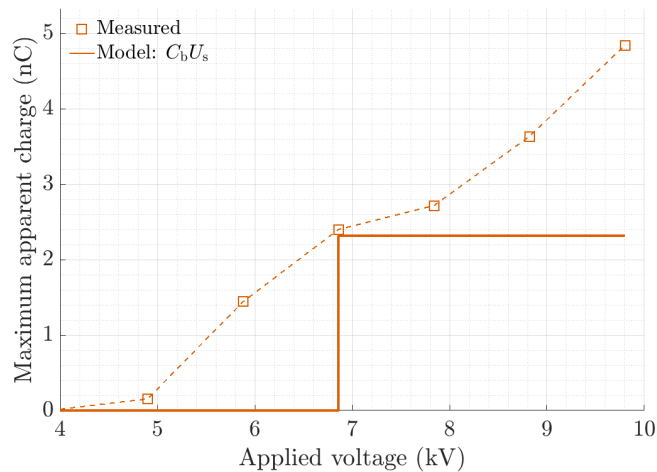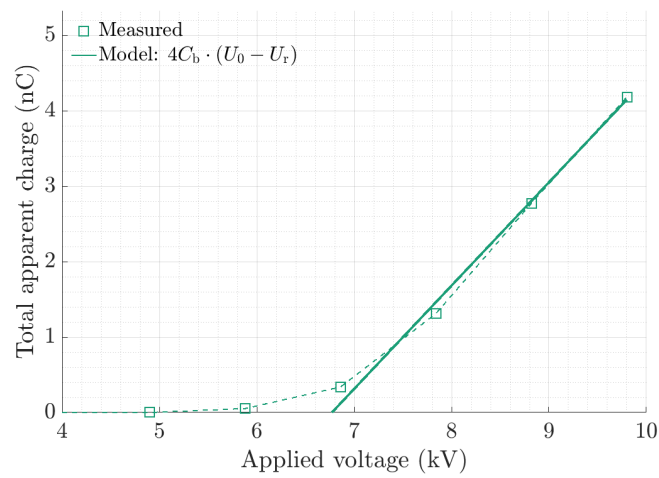

Figure 6.7: Measured total apparent charge per period as function of voltage. Results were obtained at 90°C and 50 Hz for the bars close to high voltage terminal. The model is based on one void.

The measured total apparent charge per period as a function of frequency is presented for one example bar close to the high-voltage terminal (GB3) in Figure 6.8 and in Figure 6.9 with a zoomed-in y-axis at the indicated temperatures. The measured values are compared to a model including the increased PD repetition rate given by Equation (2.13), caused by increased residual charge relaxation. The purpose in this figure was to focus on the frequency dependency of total apparent charge. The PD repetition rate in the model was therefore fixed at the value at 50 Hz, and hence not including effects in the model that are temperature dependent and frequency independent. The important model parameters are given in Table 6.3. The residual charge relaxation time constant is, in addition to the estimated void conductivity, based on measured dielectric response (shown in Chapter 6.1.2) inserted into Equation (2.14), and shown in Figure 6.10. The fraction $d_{\mathrm{b}}/d_{\mathrm{c}}$ was fixed at 9 based on the calculated void gap distance from the PDIV measurements (2.7 mm/0.3 mm). No frequency dependence of total apparent charge was observed above 1 Hz below 100 °C.
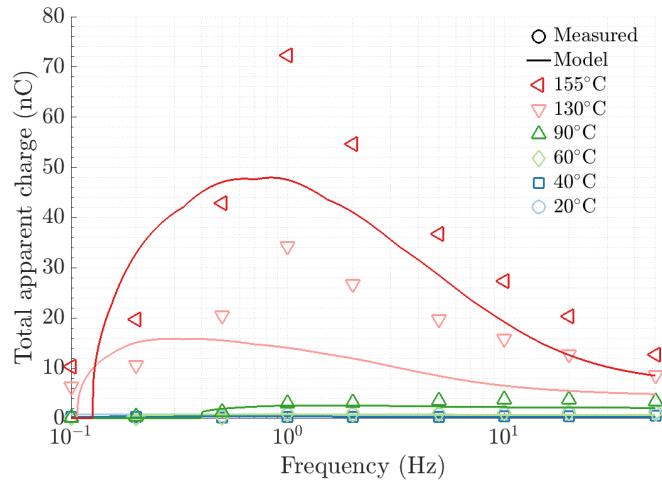
Figure 6.8: Measured total apparent charge per period as a function of frequency. The measured values are compared to the model for total apparent charge, based on the PD repetition rate found by using Equation (2.13). The estimated values are based on measured dielectric response and calculated void conductivity. Measured results were obtained for generator bars close to neutral terminal.
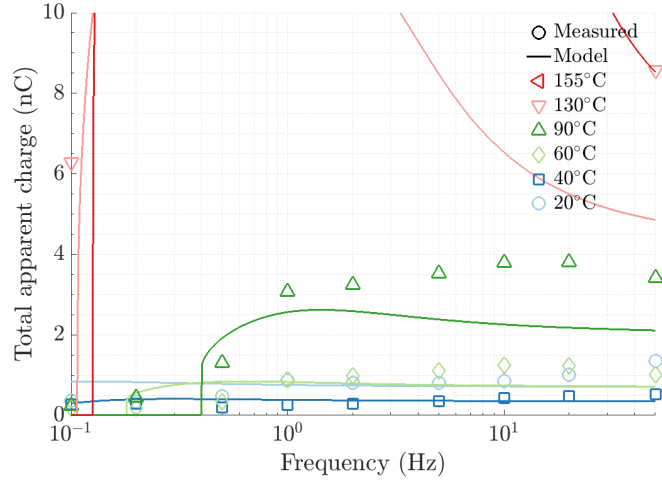
Figure 6.9: The same as Figure 6.8, but with a zoomed-in y-axis.
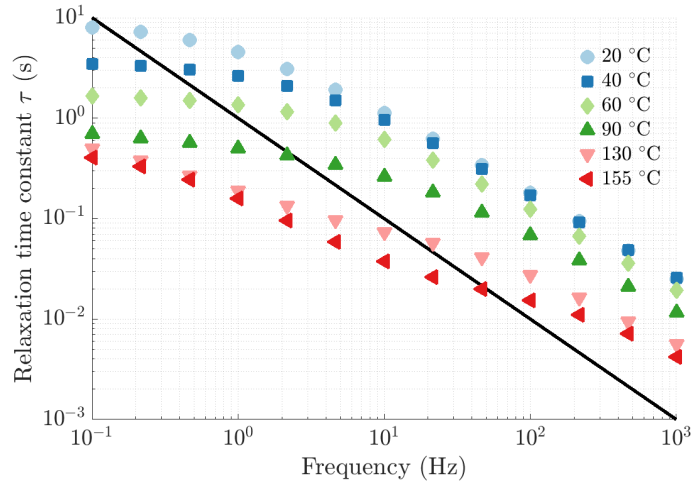
Figure 6.10: Calculated relaxation time constant as a function of frequency at indicated temperatures. The values are based on Equation (2.14) with the measured dielectric response and calculated void conductivity for the curve fit in Table 6.3. Values below the solid black line are time constants lower than the voltage period where relaxation is important.

Table 6.3: Residual charge relaxation parameter values.

Parameter name	$\sigma_{\mathrm{b}}(20°\mathrm{C})$	E_{ab}	$\sigma_{\mathrm{c}}(20°\mathrm{C})$	E_{ac}
Unit	S/m	eV	S/m	eV
Bar	$1 \cdot 10^{-16}$	0.44 [1]	$5.2 \cdot 10^{-15}$	0.9
Laboratory object	$5 \cdot 10^{-15}$	0.44	$8.9 \cdot 10^{-15}$	0.9

[1] From mica/epoxy tape used in the laboratory object.

6.6 Defects in the Cross-Sections of Sectioned Stator Bars

All nine generator bar objects were sectioned into twelve 1.5 cm thick pieces. The surfaces were sanded to get a smooth cross-section surface and then investigated with a microscope for voids. Figure 6.11 shows a typical cross-section. It is possible to identify the tape layers, epoxy filler, copper strands, and strand insulation.
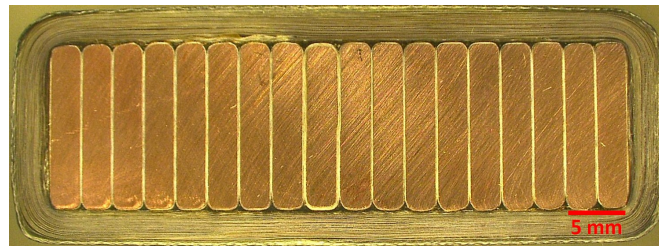
Figure 6.11: Photo of a typical cross-section in this thesis for the tested generator bars with 3 mm thick mica/epoxy insulation. It is possible to localise the copper strands with strand insulation, the mica/epoxy tape layers, and filler material between strands and tape.

The mica/epoxy tape in the main wall insulation were generally without voids, as indicated in Figure 6.12a. The complete insulation system in the back-up bars is intact, and no defects were found in Figure 6.12b. If voids are present, they would have a void gap distance below 0.03 mm, which according to Paschen law and Figure 2.8 have a PDIV above 10 kV and hence are not relevant in this study limited to 10 kV.
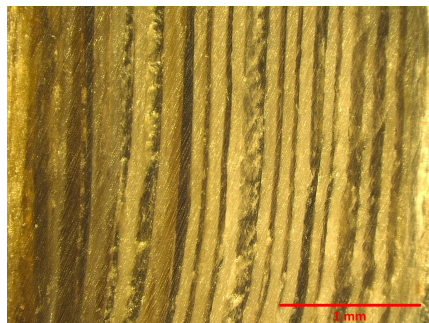
(a) Main wall insulation
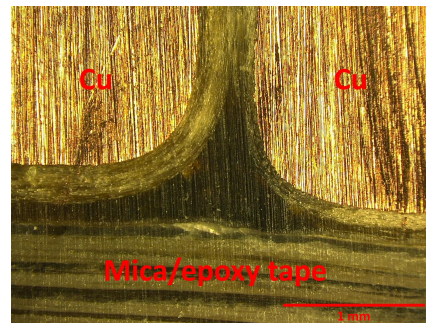
(b) Main wall insulation, filler material, strand insulation, and strands.

Figure 6.12: Photo of selected cross-sections of insulation, where no voids were detected. The epoxy filler is dark, whereas the light regions are mica.

The bars from service show brown crystals between the copper strands and the mica/epoxy tape layers, with several examples shown in Figure 6.13. These brown crystals occur close to the copper strands in both object types from service, that is, indications of no voltage needed to form those crystals. The formation of such crystals can, therefore, be correlated to the conductor temperature, which can be assumed equal in the stator. Some of these regions are already starting to crack and cause voids, Figure 6.13d, and it is probable that the region with brown crystals is weak.
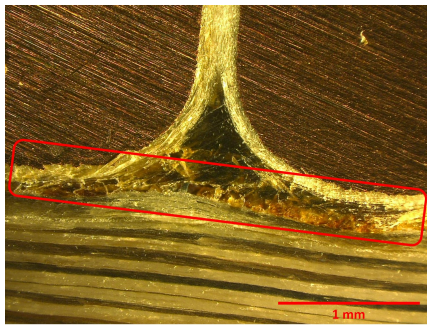
(a) Example 1
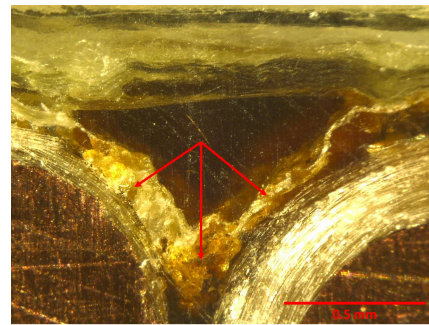
(b) Example 2
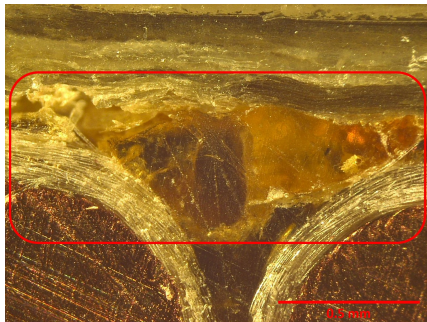
(c) Example 3
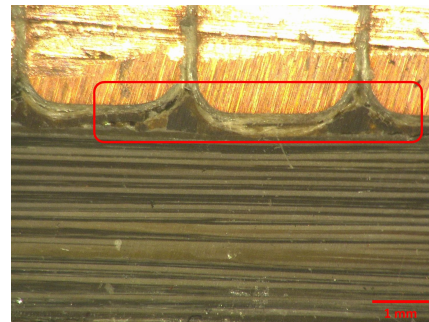
(d) Example 4

Figure 6.13: Selected photos containing brown crystals between tape and copper strands from service-aged bars. Example 4 additionally has cracks in the brown crystal region.

The bars from service showed voids between the copper strands and the mica/epoxy tape and delamination, as shown in Figure 6.14. Table 6.4 summarises the findings from the dissection. The maximum electric field in these voids is comparable to cylindrical voids as shown in a FEM simulation in Appendix A.2. No general conclusions should be drawn to voltage dependence in ageing due to the very limited number of bars investigated by microscope.

Table 6.4: Results from microscopy investigations of the bars.

Bar	#	Tape	Between strands and tape	Voids
Back-up bar	1	Good	Some brown crystals	No
	2	Good	Some brown crystals	No
	3	Good	Some brown crystals	Delamination[1]
Low	1	Good	Brown crystals	Much delamination
voltage	2	Good	Brown crystals	Much delamination
terminal	3	Good	Brown crystals	Yes - a few
High	1	Good	Brown crystals	Delamination[1]
voltage	2	Good	Brown crystals	Yes - a few spheres
terminal	3	Good	Brown crystals	Large voids in strand wedges

[1] The delamination was found at a location in the bar that were pressed together during voltage application. These voids are, therefore, expected not to influence electric PD results.
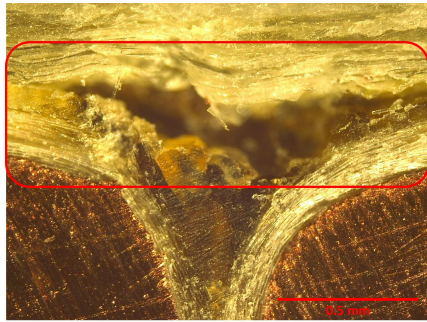
(a) Example 1: Void
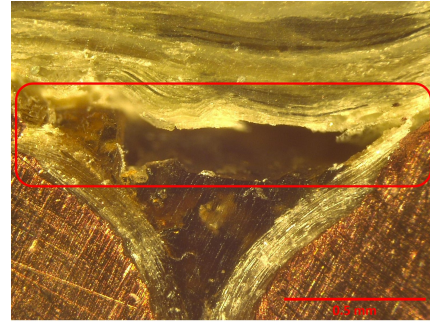
(b) Example 2: Void
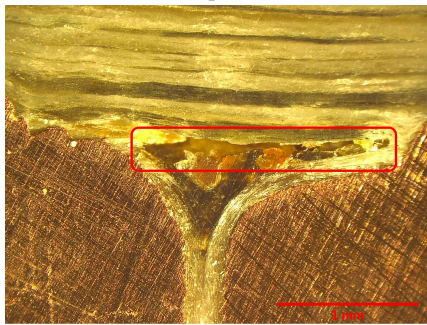
(c) Example 3: Void
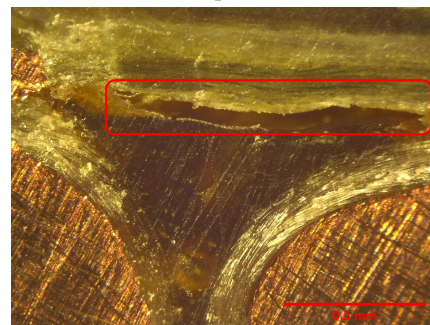
(d) Example 4: Void
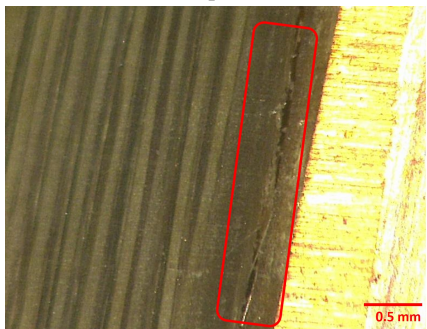
(e) Example 5: Delamination
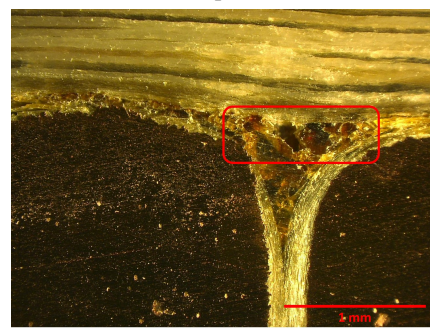
(f) Example 6: Void

Figure 6.14: Selected voids observed in the stator bar cross-section. The void gap distance in Example 2 is approximately 0.2 mm.

Chapter 7

Results Describing the Effect of Constant Voltage Application

7.1 Void Resistance Change due to PD Activity

The void resistance was measured using laboratory object M3 with copper wires to the outside at three instants correlated to one hour of voltage application at 20 °C. Table 7.1 presents the results, which show that the resistance decreases with PD activity and is restored when the object is grounded afterwards.

Table 7.1: Measured void resistance on laboratory object M3 as function of time.

Time (h)	Resistance (TΩ)	Comment
0	> 3	Before voltage application
1	1	2 min after 1 h voltage application at 50 Hz 10 kV
20	> 3	19 h with 0 V after 1 h voltage application

7.2 The Effect of Voltage Application on PD Activity

Based on the literature survey in Chapter 1.2, it is expected that PD activity will result in increased PDIV. One M1 laboratory object with a diameter of 10 mm and a void gap distance of 0.5 mm was, therefore, tested by increasing the voltage stepwise at 0.1 Hz without any preconditioning. This test demonstrated a PDIV of 5 kV.

The second PDIV test of four M1 laboratory objects succeeding the first complete frequency and temperature sweep did not produce any significant changes to the PDIV curves. Possible permanent surface changes due to the temperature and electric stress during the test do not seem to affect the PDIV.

The apparent PD repetition rate as a function of time during 1 h voltage application is shown in Figure 7.1. A vertical black line indicates the instant of 5 min that corresponds to the generally chosen preconditioning time in this thesis. The results show that the PD activity reduces as a function of time during voltage application. The reduction in the repetition rate is basically occurring during the first 10 min to 15 min. The experimental results at 20 °C are compared to the time dependence of void conductivity in Equation (2.6) with parameters $\sigma_0 = 10^{-12}$ S/m and $\tau = 0.01$ s inserted into Equation (2.5) for the voltage and Equation (2.15) for the repetition rate. It is seen that the model predicts a too high decrease rate and does not adequately describe the reduction in PD activity as function of time with PD activity.
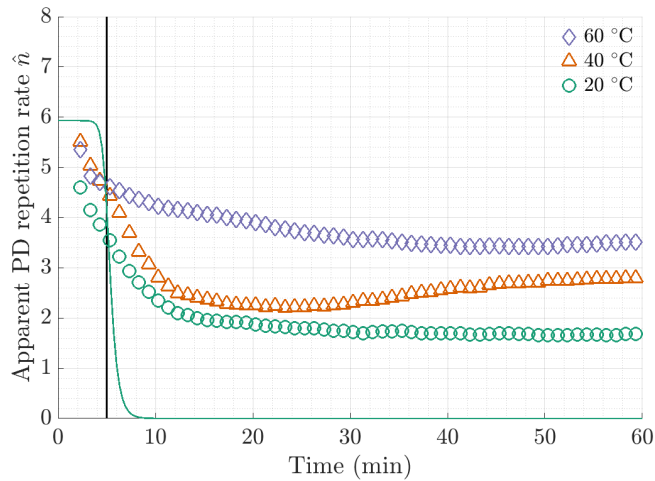
Figure 7.1: Apparent PD repetition rate $\hat{n}$ as function of time during the voltage application at 10 kV at indicated temperatures. The measured values are compared to the model at 20 °C (solid line).

The apparent PD repetition rate as a function of time after a 1 h voltage application period (gray shaded region in Figure 7.2a) and after a 5 min voltage application (Figure 7.2b) period are presented at 20 °C, 40 °C and 60 °C. The measured values were fitted to Equation (2.7) by choosing the optimal value for the void conductivity and relaxation time constant. The fit parameters are given in Table 7.2.
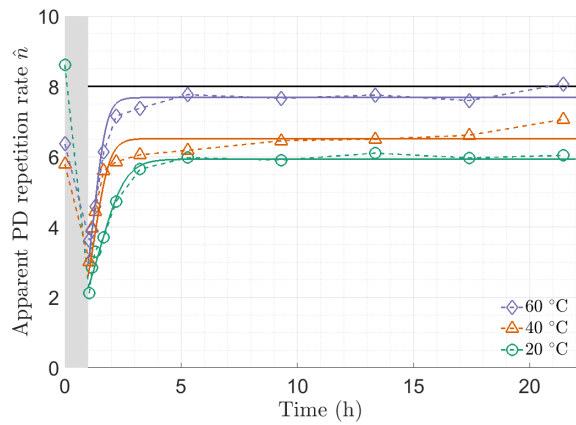
(a) Voltage application time of 1 h.
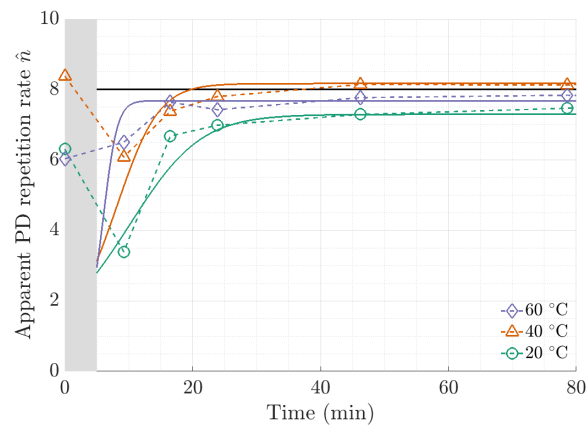
(b) Voltage application time of 5 min.

Figure 7.2: Apparent PD repetition rate at 50 Hz vs time as the average of three objects, D = 10 mm. The solid lines are model fit to Equation (2.7). The grey shaded area represents the voltage application period of 1 h.

Table 7.2: Measured void resistance on laboratory object M3 as function of time.

Parameter	Value for 5 min	Value for 1 h	Unit
σ_{c}	$1.2 \cdot 10^{-8}$	$1.2 \cdot 10^{-8}$	S/m
τ_{20}	10	60	min
τ_{40}	6	40	min
τ_{60}	2	30	min

7.3 Test Conditions during the Test Procedure

The total apparent charge from the 5 s intermediate conditioning periods at 50 Hz, described in the voltage procedure in Figure 4.7 between the PD tests at different voltage frequencies, were used as a measure on the stability of PD parameters at 50 Hz throughout the frequency sweep. The results presented here were obtained in one laboratory object M1 with a void diameter of 10 mm and a void gap distance of 0.5 mm are shown in Figure 7.3. This is a typical graph, representing the test objects. The values increase with sweep frequency at 20 °C and 40 °C, are stable at 60 °C and 90 °C, and decreases at 130 °C and 155 °C.
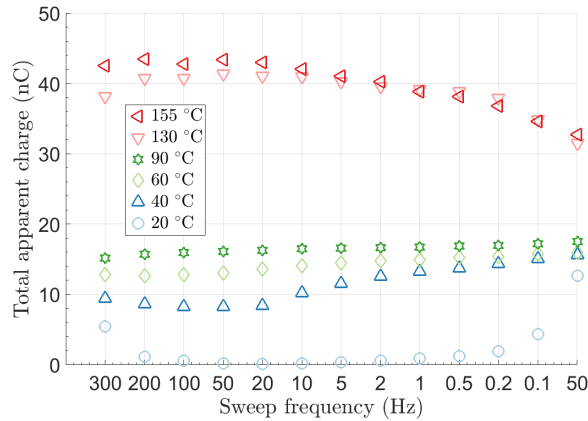
Figure 7.3: Measured total apparent charge per period during the 5-second intermediate condition periods at 10 kV 50 Hz (obtained before indicated sweep frequency). This is one example obtained for a laboratory object with a void diameter of 10 mm and a void gap distance of 0.5 mm.

Chapter 8

Discussion

This section starts by discussion the supplementary research questions regarding method development (Chapter 8.1) and test object applicability (Chapter 8.2). When those questions are sufficiently answered it is possible to discuss the main research question (Chapter 8.3) with less uncertainty with respect to test method and different object geometry. The discussion is summarised in Chapter 8.4 discussing possible applications of this work in condition assessment of hydropower generators.

8.1 Discussion of the Effect of PD Activity

This section discusses the supplementary research question: ***What is the effect of pre-conditioning on measurable PD quantities?*** Answering this question is needed in order to understand if the chosen test method facilitates time invariant void conditions throughout the frequency sweep. A time invariant void condition implies that any measured difference obtained from different test frequencies can be understood as a frequency dependence.

a) The Effect of a Long Voltage Application Time

Constant voltage application decreases the void resistance and, hence, the PD activity.

Chapter 7.1 describes results from resistivity measurements from before and after applying voltage at 10 kV for 1 h performed on laboratory object M3. Initially, the resistivity was above the equipment limit of 3 TΩ. This value was reduced to 1 TΩ immediately after the 1 h voltage application period.

The measured apparent charge magnitude and its repetition rate can be represented by the total apparent charge per period, as was done in this thesis. Chapter 7.2 describes

the results from the study concerning the effect of voltage application. Figure 7.1 shows the results for the total apparent charge per period at 50 Hz during 1 h 10 kV voltage application at 20 °C, 40 °C, and 60 °C. The apparent repetition rate decreases during the first 15 minutes. This decrease can be deduced to be correlated to PD by-products acting as charge carriers and increasing the void conductivity, which by Equation (2.9) reduces the void voltage.

The required conductivity increase after the 5 min voltage application to describe the reduction in PD activity is much higher than measured in for example Levesque et al. [40] for slot discharges obtained at a voltage much higher than PDIV. They observed a sufficiently high conductivity increase after 100-1000 hours. It is a contradiction between the literature description of a low increase in surface conductivity with PD activity and the explanation of experimental results by a greatly increased void conductivity. The void resistance was measured to decrease with PD activity, supporting that PD activity in cylindrical voids in this study had an increased void conductivity.

The effect of voltage application is here directly experimentally shown to reduce void resistance and to reduce PD activity.

b) The Effect of Voltage Application with Time without PDs present

The effect of constant voltage application vanishes with time after grounding the object.

Chapter 7.2 describes results from the study of the effect of voltage application after grounding the test object. Results in Figure 7.2 shows the total apparent charge per period at 50 Hz after 1 h of preconditioning at 50 Hz 10 kV at 20 °C, 40 °C, and 60 °C. The apparent repetition rate increases during the first two hours after the grounding of the test object and thereby more PDs occur in the system. The reduced total apparent charge vanishes faster at higher temperatures. The same trends are seen for the restoration after 5 min preconditioning but with shorter time constants. Hudon et al. [29] correlated an increased conductivity to PD by-products acting as charge carriers. Such by-products can be assumed to self-decompose at a higher rate at higher temperatures, especially nitric acid [58]. Testing at different temperatures shows different numerical values of convergence. This can be explained by a temperature-dependent equilibrium of the self-decomposition process. The charge carriers are self-decomposed to a greater extent at a high temperature than at a low temperature. However, the existence of such charge carriers was not measured explicitly, and the discussion here is based on their existence from literature and observed experimental effects.

The effect of voltage application is here shown to vanish with time after grounding the test object, in line with the model.

c) The Effect of Preconditioning the Test Objects

Preconditioning the test objects ensures similar start conditions for the different voltage frequency tests.

The purpose of preconditioning test objects is to obtain stable test conditions. Figure 7.3 shows results from the 50 Hz intermediate conditioning. The results show that the observed trend at 20 °C and 40 °C are increasing, but PD results in Chapters 5 and 6 show an opposite function of frequency. The same is seen at 130 °C and 155 °C. This indicates that the measured frequency dependency for typical PD parameters in this thesis describes a frequency dependency and not a time dependency caused by the test method.

The measured total apparent charge from the intermediate conditioning periods was stable, or of an opposite trend as was measured for PD quantities, throughout the frequency sweep. It is, therefore, reasonable that the used voltage application frequency sweep reveals a frequency dependence and not an effect of a time dependence of PD parameters.

8.2 Describing Test Objects with Unknown Void Content

This section discusses the supplementary research question: ***How can the measured PD parameters from generator bars be compared to voids with known geometry?*** Answering this question is needed in order to know how to adequately describe generator bars by the presented models.

a) Comparing the Void Electrode Area for Single Discharges to the Total Void Electrode Area

Only a fraction of the void electrode area discharges in each PD, but during a voltage period, the entire void electrode area is discharged.

The laboratory objects have voids with a defined geometry. This is not the case for the generator bars, where the results from cross section microscopy in Chapter 6.6 identified many voids with various dimensions that cannot be determined without performing destructive dissection. Delamination and voids with a large void electrode area were localised in the bar cross sections. It is reasonable, based on presented cross-sections in Figure 6.14, to approximate the observed large voids in the generator bars as parallel void electrodes separated by a void gap distance.

Figure 5.6 from Chapter 5.4 is repeated in Figure 8.1 and presents the difference between PD repetition rate as a function of PD amplitude for laboratory object M1 with insulating void electrodes and laboratory object M3 with conductive void electrodes. The results for

M3 have a few and large PDs located around the expected apparent charge magnitude. The corresponding PD magnitude distribution for M1 consists of a larger number of PDs, but they are smaller in magnitude. However, both test objects show comparable apparent repetition rate (M1: 9 vs M3: 13). This means that the total apparent charge per period is comparable for the case with a few large PDs closely related to the expected value and a distribution of PD magnitudes with more small magnitudes. The PD energy per period is therefore not affected by whether the void electrode is completely or partly discharged during one PD because partly discharged void electrodes have a higher PD repetition rate, but with smaller amplitudes.
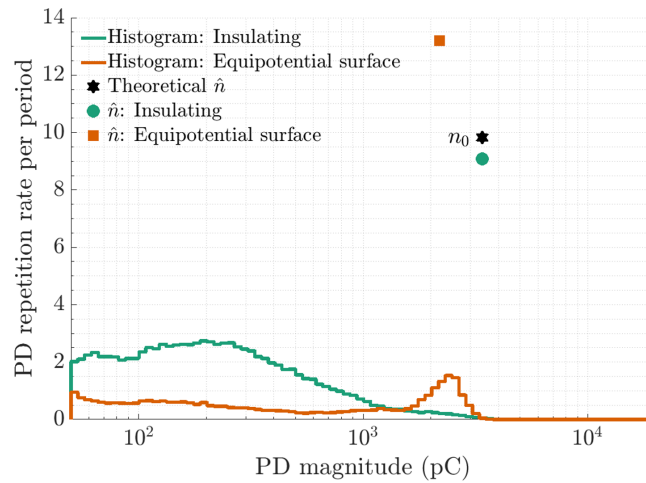
Figure 8.1: *Repetition of Figure 5.6*. Measured PD repetition rate per period as a function of PD magnitude (histograms in solid lines) and apparent repetition rate for the same data (markers). Results were obtained at 90 °C and 10 kV at 50 Hz for laboratory objects with void diameter of 10 mm and void gap distance of 0.5 mm. Two objects with different void electrode surface are compared: an object with insulating surfaces (M1) and an object with equipotential surfaces (M3).

The measured PD repetition rate per period as a function of PD magnitude for laboratory object M1 ($D = 10$ mm) in Figure 5.5 and generator bar sections in Figure 6.4 are shown together in Figure 8.2. The two curves are comparable, and even the single void with defined geometry produces a distribution. Such a distribution is expected from literature [41]. The large difference between results from the two objects is that the number of small PD magnitudes in the generator bar sections are significantly larger than those in the single void. This indicate that the generator bars have many small voids, which is reasonable with respect to the results from the cross-section microscopy. Both test objects have a distribution of PD repetition rate, rather than the expected repetition rate. This similarity suggests that there is no fundamental difference in the results from testing on one large void or many small voids. This is important because it enables the use of the super position principle for the presented theory for PDs.
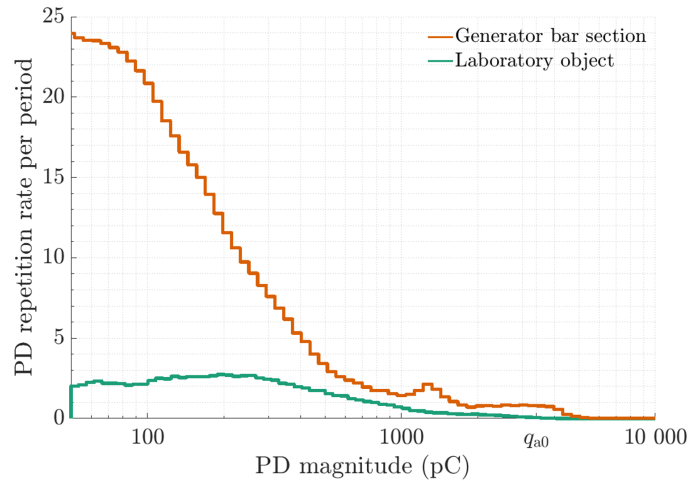
Figure 8.2: Measured PD repetition rate as function of PD magnitude. Results are given as a comparison of both laboratory object with a void diameter of 10 mm (average curve in Figure 5.5) and generator bars (average curve in Figure 6.4) at 50 Hz, 90 °C, and 10 kV.

The measured results for PD repetition rate as a function of PD magnitude for different voltage frequency, test temperature, void size, and maximum test voltage are presented in Appendices B.1 and B.2. The overall shape of all graphs is similar: A few large PDs and many small PDs. The differences are with respect to maximum PD and the size of PD repetition rate. The apparent repetition rate $\hat{n}$ was comparable to the theoretically expected repetition rate. This means that the PD repetition rate as a function of PD magnitude can be represented by an apparent repetition rate. The apparent repetition rate is equal to how many times, in total, the geometrical void electrode is discharged during a voltage period.

A ratio between the apparent repetition rate and the theoretical repetition rate clearly shows deviations from the expected value. This ratio as a function of both temperature and void diameter is presented in Figure 8.3 based on data at 300 Hz. It is seen that voids with a geometrical void electrode area larger than 5 mm in diameter are only partly discharged because the ratio is less than 1. However, at higher temperatures, this ratio increases. The voids with a diameter of less than 10 mm have a ratio larger than 1, indicating a larger void electrode area than the geometrical void electrode area. This high number can, however, be caused by PD noise from the measure system at high temperatures, as was measured in the M4 object without voids. The total apparent charge per period from the measure system was about 10 nC, whereas the measured total apparent charge for a void diameter of 3 mm was 40 nC at 155 °C. It is, therefore, possible that the insulation system unintentionally had a larger void than the geometrically defined 3 mm diameter.
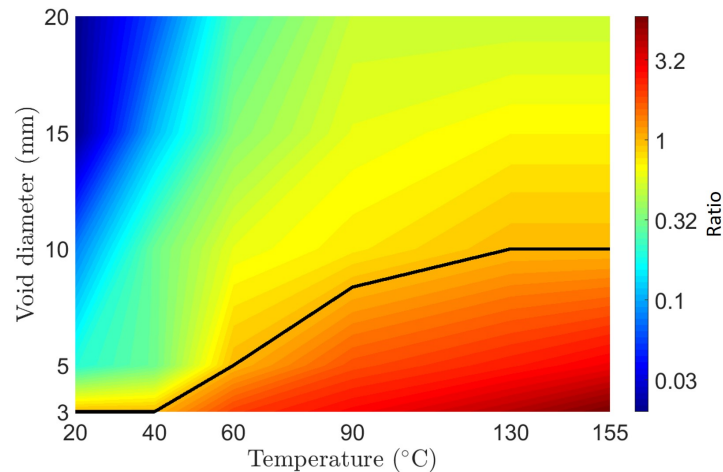
Figure 8.3: Ratio of measured apparent repetition rate and theoretical repetition rate as a function of temperature and void diameter. The ratio of 1 is indicated by the black line.

This research question is only partly answered here and can act as an introduction to further work describing the geometry and distribution of the generator bar voids in more detail. It is, however, sufficiently answered to understand that the presented models can be used for both tested objects.

Only a fraction of the void electrode area discharges in each PD. The apparent repetition rate is for many test parameter combinations found to correlate closely to the expected repetition rate. It is possible to correlate a high PD activity to that of PD occurring in a large void or many smaller voids with the same total void electrode area.

b) Comparing Dissection and Electrical PD Results

There is a correlation between measured PD parameters and void size and number in the test object.

Table 8.1 presents the estimated void gap distance and the total discharged void electrode area based on electrical PD measurements and Equation (2.12) and Equation (2.9), and estimated void content from cross section microscopy. Only values at 20 °C are considered to avoid possible temperature changes in void geometry because dissection happened at 20 °C. The estimates of void electrode area from both electrical PD measurements and cross section microscopy are showing the same trends. This means that the electrical PD measurements, together with the presented models, can indicate the generator bars with a high void content.

Table 8.1: Calculated void geometry compared to detected void type. Results were obtained for all tested generator bars GB1-3 at 20 °C. A_{TOT} represents the total discharged void electrode area based on PD measurements. The measured void gap distance from cross-section microscopy in the object from close to high-voltage terminal was approximately 0.2 mm. The total copper surface area was estimated to be 280000 mm^2.

Object		Estimates based on electrical measurement		Dissection
		Void gap	A_{TOT}	Void type
		mm	mm^2	
Back-up	1	0.11	84	None
bar	2	0.09	84	None
	3	0.11	56	Small/few
Low	1	0.20	**1340**	**Delamination**
voltage	2	0.20	**924**	**Delamination**
terminal	3	0.14	168	Small/few
High	1	0.08	224	Small/few
voltage	2	0.08	196	Small/few
terminal	3	0.22	**1430**	**Large voids**

The estimated maximum void gap distance from the microscopy pictures of the bar cross section in Chapter 8.2 ($\approx$ 0.2 mm) is in line with the results from electrical measurements ($\approx$ 0.2 mm). The generator bars with an increased void content, compared to those without voids, had correspondingly higher PD activity with an estimated high void electrode area. The comparison between voids found in cross-sections and experimental PD results in Table 8.1 indicates that the electrical PD measurements can localise the bars with voids.

There is a correlation between void size and number and measured PD properties.

8.3 Voltage Frequency and Temperature Dependence of Measurable PD Parameters

It is known from the literature, for example IEEE std 322 [9], Forssén et al. [24], [20], and Illias et al. [25], that the PD results obtained from 0.1 Hz tests might significantly differ from those at 50 Hz. The frequency and temperature dependence of experimental results presented in this thesis can be explained by features in the impedance abc-model (Model 3).

This section discusses the results addressing the main research question: ***Why are the measurable PD parameters different when applying a voltage frequency at power frequency (50 Hz) compared to very low frequency (0.1 Hz)?*** It is first necessary to elucidate if the PD features are frequency and temperature dependent, as literature shows for other materials. Second, to discuss the frequency and temperature dependence of important material properties that influence the models describing measurable PD features. After this, the estimated void voltage for different test conditions are discussed. Having established the frequency and temperature dependency of the void voltage, it is easier to discuss the measurable PD parameters, such as the maximum apparent charge, total apparent charge, remanent voltage, and finally a discussion of the validity of the models for different void geometries.

a) Frequency and Temperature Dependency of the Measured PD parameters.

PD parameters are frequency-dependent in the case of generator bar insulation.

Experiments from literature show a voltage frequency dependence of PD parameters, giving rise to the main research question. Those experiments were performed in polycarbonate and epoxy resin objects including a cylindrical and a spherical void [24] [25]). These objects are comparable, but not identical, to the generator bar insulation with voids studied in this thesis. It was, therefore, necessary first to establish whether the studied voids produced frequency-dependent PD parameters.

The main results presented in Chapter 5 and Chapter 6 are summarised here to support the hypothesis stating that there is such a frequency dependence.

The measured PDIVs are generally frequency independent at temperatures below 100 °C for the generator bars. The PDIVs for voltage preconditioned cylindrical voids are frequency dependent at 20 °C, 40 °C, and 60 °C, where the PDIVs at low frequencies are higher than the maximum applied voltage. The PDIVs at 130 °C and 155 °C for both test objects are low at low frequencies. The PDIV changes with temperature and frequency

but is frequency independent at 90 °C only in the tested voltage frequency range of 0.1 Hz to 300 Hz.

The measured maximum apparent charge is increasing with frequency. This effect becomes stronger with temperature, lowering the cut-off frequency.

The measured total apparent charge per period is frequency independent above 1 Hz and below 100 °C for both objects. This was observed as a frequency dependence at 130 °C and 155 °C with a peak at 1 Hz.

PD parameters obtained from voids in generator bar insulation are frequency-dependent for some test temperatures and frequency ranges, whereas frequency independent for other test temperatures and frequency ranges.

b) The Temperature Dependence of Insulation Material Conductivity and Dielectric Response

The insulation material conductivity and dielectric response function vary with temperature.

Chapter 5.1.1 describes measured material DC conductivity for the laboratory object M4 without a void. The temperature dependence of the DC conductivity is well described by an Arrhenius relation ($\propto \exp(-E_{\mathrm{a}}/k_{\mathrm{B}}T)$).

Chapter 5.1.2 and Chapter 6.1.2 describe the measured dielectric response as a function of frequency for the void-free laboratory object M4 and one generator bar, respectively. Results showed that the material dielectric response in both cases is comparable to a function of frequency and temperature. The dielectric response as a function of frequency at different temperatures are well described by one Cole-Cole mechanism with a temperature dependence in the relaxation time τ in Equation (2.8) in accordance with an Arrhenius relation.

The insulation material conductivity and dielectric response vary with temperature. The temperature dependence is modelled by an Arrhenius relation for the conductivity and an Arrhenius relation in the relaxation time τ in the Cole-Cole model describing the complex permittivity.

c) Estimated Void Voltage

The three presented abc-models are suitable to describe measured PDIV.

The presented theory in this thesis has three variants of the impedance abc-model:

Model 1: The classical capacitive model.

Model 2: The capacitive and resistive model.

Model 3: The impedance abc-model including dielectric response.

The three models require different material properties, where Model 1 only requires the permittivity, Model 2 requires both permittivity and conductivity, and Model 3 requires the conductivity and frequency-dependent complex permittivity. Figure 8.4 shows the frequency and temperature dependence of PDIV for laboratory object and generator stator bars compared to the three impedance abc-models (See also Figure 5.4a and Figure 6.3b for the presentation of the results). The void voltage is determined by the Paschen law at PDIV, which means that all model parameters except void conductivity can be determined if the void geometry is known. The frequency independent PDIV, Model 1, can be used for both test objects above 20 Hz at all temperatures and at all measured frequencies at 90 °C (laboratory object) and below 90 °C (generator bars). Resistive elements included in Model 2, are needed to explain the increased PDIV at low frequencies at temperatures below 90 °C in the laboratory objects. Similarly, the dielectric response included in Model 3 is needed to describe PDIV at 130 °C and 155 °C at frequencies below 20 Hz.
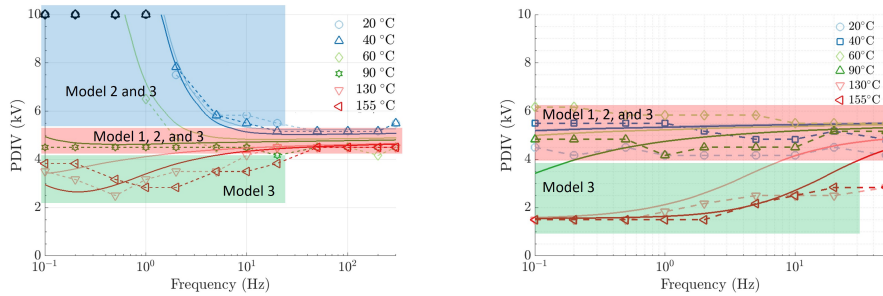
(a) Typical PDIV curve for Laboratory object M1. This example has $D = 10$ mm and $d_\mathrm{c} = 0.1$ mm.

(b) Typical PDIV curve from generator bars. This example is from a bar close to high voltage terminal.

Figure 8.4: Selected PDIV figures. The different coloured areas indicate in what regions the models are valid.

The PDIV is well described by one of the three models. This means that the temperature and frequency dependence of PDIV are determined by the temperature and frequency dependence of the dielectric response and DC conductivity. It is, therefore, possible to

determine which model it is necessary to use by knowing the dielectric response and DC conductivity and their temperature dependence in advance.

The different regions, in which the different abc-models apply in Figure 8.4, are summarised in Figure 8.5 as a function of temperature and frequency. The example shown here includes the laboratory object. A similar graph was obtained for the generator bars, but not shown. The main difference is slightly changed borders between the indicated regions.
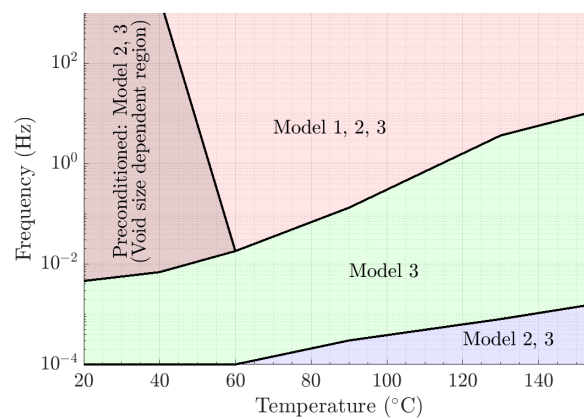
Figure 8.5: Model regions for different impedance abc-model approximations based on measured dielectric response.

The effect of electrical preconditioning was to decrease PD activity (as discussed in Chapter 8.1), which is here modelled by an increase in the equivalent void conductivity in the impedance abc-model. The generator bars and large voids without electrically stressed side walls did not show an increased PDIV at low frequencies at temperatures below 90 °C. From this, two important observations can be made:

1. PD activity increases the void surface conductivity, hence voids without electrically stressed side walls does not show an increased void conductivity.

2. The PD activity in an object with many small voids is not affected by the voltage precondition as is the case for larger voids.

The impedance abc-model can be used to calculate the relation between the applied voltage and the void voltage with Equation (2.9). Knowing the permittivity and void geometry enables a simple prediction of PIDV, with the void voltage assumed to be the Paschen voltage. The dielectric response is additionally needed to predict PDIV at 130 °C and 155 °C when testing at voltage frequencies above 0.1 Hz. The high estimated void conductivity at temperatures below 90 °C is likely to be caused by the PD activity and is therefore not possible to determine before doing experiments.

d) The Measured Maximum Apparent Charge

The maximum apparent charge is frequency-dependent and is modelled by a time lag.

The maximum apparent charge as a function of voltage is expected to follow a step function, as described in Equation (2.10). This was the case for all laboratory objects with one single void at all voltage frequencies and temperatures, as shown in Figure 5.7. The generator bars with many unknown voids showed a linear increase in voltage instead, as illustrated in Figure 6.5. This might indicate that either the different voids in the generator bars are more likely to simultaneously discharge than the large void in the laboratory objects when increasing the voltage, or that voids with different inception voltage and void electrode area was present in the generator bars. This was, however, not investigated in detail.

The maximum apparent charge as a function of frequency at different test temperatures was found experimentally and is presented in Chapter 5.5 for variants of laboratory object M1 and in Chapter 6.4 for generator bars. The experimentally detected frequency dependences at different temperatures for the two test objects are comparable. No general dependency of PD parameters as a function of the void diameter was seen in the laboratory objects. A cut-off frequency that describes the lowest frequency without influence of a time lag is given in a temperature-void diameter map in Figure 8.6. From the figure it is seen that the time lag is insignificant at temperatures below 40 °C but significant at higher temperatures where it influences all frequencies above 1 Hz. The experimental results fit the model describing an increase in calculated time lag from 1 ms to 10 ms when increasing the temperature from 20 °C to 155 °C.
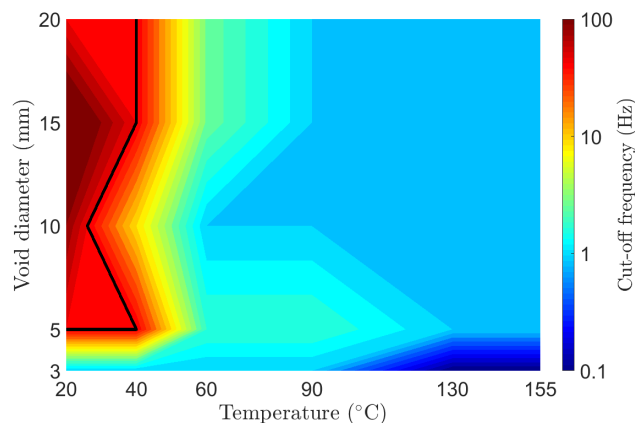
Figure 8.6: Cut-off frequency map for the time lag as a function of void diameter (y-axis) and temperature (x-axis). The time lag is important *above* the indicated cut-off frequency. The cut-off frequency of 50 Hz is indicated by a black line.

Gäfvert et al. [54] used a statistical time lag of 0.1 ms, whereas the presented results in this thesis indicate that a time lag of 1-10 ms yields the best fit to observations. A time lag of more than 1 ms was also found by Illias et al. [27] to describe their experimental results in small spherical voids. The time lag was also found to be dependent on temperature in this thesis, which is also found by Illias et al.

Figure 8.7 presents the measured ratio between measured maximum simultaneously discharged void electrode area and the geometrical void electrode area as a function of temperature for the laboratory objects. This was obtained by using the measured maximum apparent charge at 0.1 Hz, assuming no influence of the time lag at 0.1 Hz. It is seen that the discharged void electrode area increases with temperature. This can be correlated to the calculated high void conductivity from PDIV measurements and the impedance abc-model at temperatures below 90 °C. This was not further examined in this work.
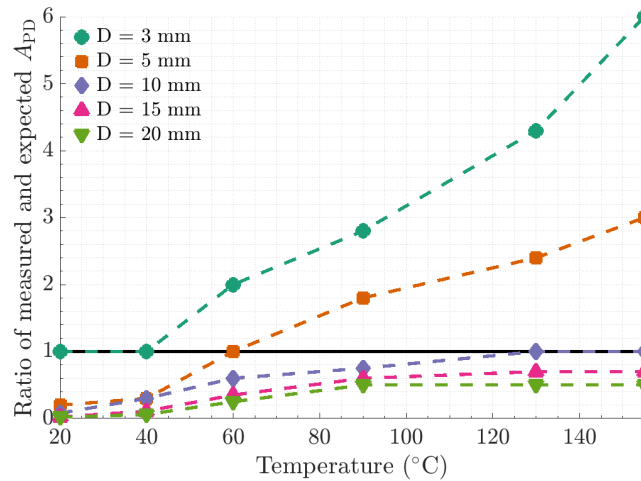
Figure 8.7: *Repetition of Figure 5.8.* Ratio between measured maximum simultaneously discharged void electrode area and the geometrical void electrode area as a function of temperature. The results were obtained for laboratory object M1. The ratio of 1 is indicated by a solid black line.

The maximum apparent charge is higher at higher frequencies. The transition from low to high frequencies is here modelled by a time lag in the range of 1 ms to 10 ms for all temperatures. The discharged void electrode area is smaller at temperatures below 90 °C, which can be correlated to a high void conductivity.

e) Total Apparent Charge

The PD repetition rate per period is frequency independent.

The total apparent charge as a function of voltage is expected to be linear, as described in Equation (2.12). This was measured to be the case for all test objects at all voltage frequencies and temperatures, as seen in Figure 5.10 and Figure 6.7. This implies:

1. The voltage dependency of total apparent charge per period is not influenced by a partly discharged void electrode area because the total apparent charge is a linear function of voltage for both test object types.

2. One void gap distance (d_c) is dominating in the generator bar objects. A non-linear dependence is expected if a distribution of void gap distances are present due to different inception voltage for those void gap distances.

In practice, the void electrode area is impossible to estimate for the generator bar objects by any known technique. It is, therefore, not possible to estimate the apparent repetition rate $\hat{n}$ because the capacitance C_b is unknown. The measured total apparent charge per period as a function of frequency at different temperatures is presented in Chapter 5.6 for laboratory objects and Chapter 6.5 for generator bars. The overall trend is that the total apparent charge is frequency independent above 1 Hz and below 100 °C for both test objects. Both test objects have a higher and frequency-dependent total apparent charge above 100 °C. Both situations are described by the presented theoretical model in Equation (2.13) including residual charge relaxation and dielectric response. The dielectric response is, however, only sufficiently large at temperatures above 100 °C to significantly influence the charge relaxation, as indicated in the temperature - void diameter map in Figure 8.8.
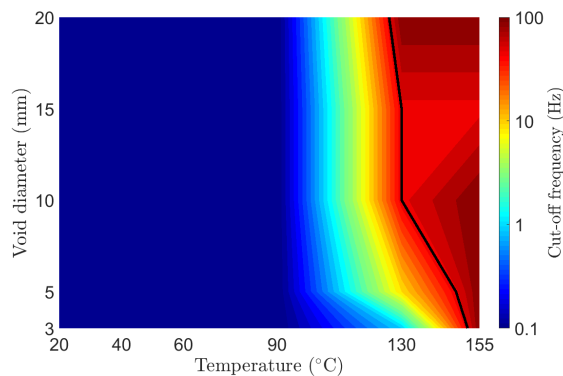
Figure 8.8: Cut-off frequency as a function of void diameter (y-axis) and temperature (x-axis). The charge relaxation is important *below* the indicated cut-off frequency. The cut-off frequency of 50 Hz is indicated by the black line.

83

The temperature dependence of total apparent charge increases linearly with temperature, as exemplified in Figure 5.13 for the laboratory object M1. The values were selected at 300 Hz to neglect the frequency-dependent increase in total apparent charge. The temperature dependence of maximum apparent charge below 90 °C was also linear. This was likely due to the high void conductivity that decreases the void voltage. The further increase above 90 °C is not explained, as the complete void area discharges at 90 °C.

These results indicate that the total apparent charge can be considered frequency independent at the combination of numbers below 100 °C and above 1 Hz for the tested objects. The frequency-dependent total apparent charge at 130 °C and 155 °C is here modelled by including the measured high dielectric response at those temperatures.

f) Void Geometry Dependence of Calculated Quantities

PD parameters are dependent on the variation in void gap distance and void diameter.

The total apparent charge is a linear function with voltage. By using Equation (2.12), it is possible to estimate the remanent voltage and series capacitance with the void (void electrode area). Performing this calculation on the measured total apparent charge per period gives a remanent voltage as a function of void diameter as shown in Figure 8.9a and as a function of void gap distance in Figure 8.9b. The presented results were obtained at 90 °C. Similar figures were obtained at different temperatures. The calculated remanent voltage follows the Paschen voltage. This means that any deviation in total apparent charge from theory with void dimensions can be associated with a change in the series capacitance C_b (void electrode area).
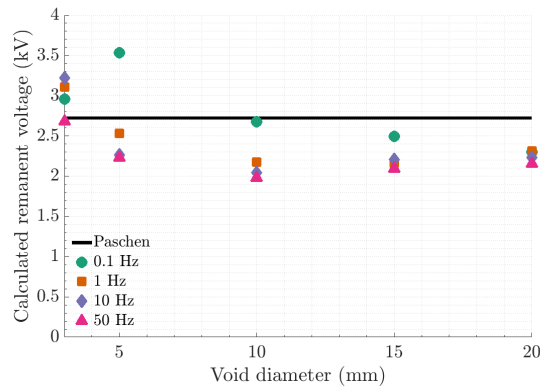
(a) Calculated remanent voltage as a function of void diameter.
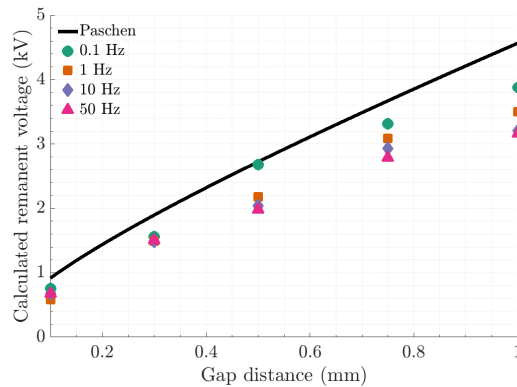
(b) Calculated remanent voltage as a function of void gap.

Figure 8.9: The presented remanent voltage was calculated from curve fits of measured total apparent charge as function of voltage to Equation (2.12). Results were obtained at 90 °C at the indicated voltage frequencies.

A comparison between the measured total apparent charge and calculated series capacitance is presented in Figure 8.10. The overall trends as a function of void diameter are identical for the two quantities. No significant frequency dependence was observed at temperatures below 90 °C.
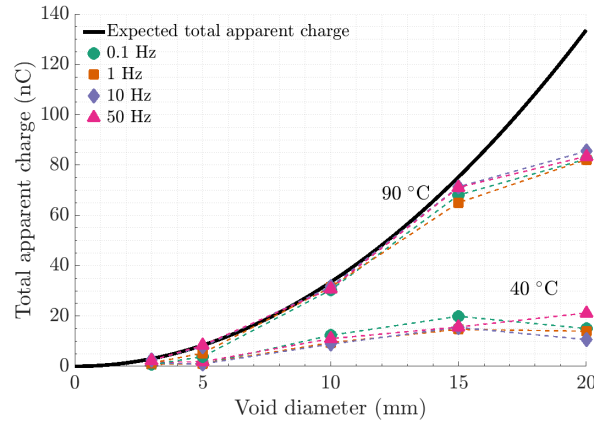
(a) Measured total apparent charge per period as a function of void diameter at 10 kV.
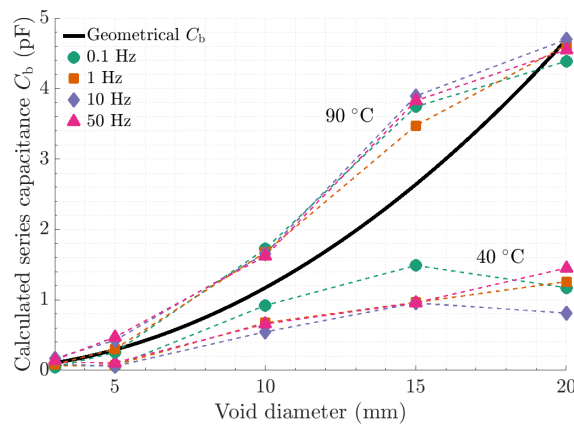
(b) Calculated series capacitance C_b as a function of void diameter.

Figure 8.10: A comparison of the measured total apparent charge per period and calculated series capacitance at the indicated frequencies and temperatures.

Voids with a diameter larger than 15 mm discharge a smaller void electrode area than expected by the geometrical value. This might indicate the existence of a maximum void electrode discharge area.

The presented PDIV figures for laboratory objects in Figure 5.3 and Figure 5.4 show a different frequency dependence of PDIV for different temperatures. Therefore, it does not exist a simple figure to adequately present the temperature and void geometry dependence of PDIV in general. The frequency dependence is here represented by the calculated void conductivity from a curve fit to the impedance abc-model in Equation (2.9). This is a single number representing the frequency dependence together with the equation. The calculated void conductivity is representing the frequency dependence of PDIV and is presented in Figure 8.11 as a function of temperature at indicated void diameters. The corresponding figure for different void gap distances show the same trend and, therefore, not included. The minimum calculated void conductivity was $4 \cdot 10^{-12}$ S/m, which corresponds to a cut-off frequency at the lowest test frequency of 0.1 Hz. The Arrhenius relation of the void conductivity in all void geometries shows decreasing values with temperature for all object geometries. This is the opposite of what is measured for the insulation material where the conductivity increases with temperature. This effect was explained in Chapter 8.1 by faster relaxation of conductive PD by-products at higher temperatures. The curves in Figure 8.11 support this statement. Only one indication of geometrical dependence was seen: The void diameters of 3 mm and 5 mm showed a high calculated void conductivity at all temperatures, opposite to the larger void diameters with only a high void conductivity at low temperatures. This might indicate a different dynamic of residual charges in the small voids.
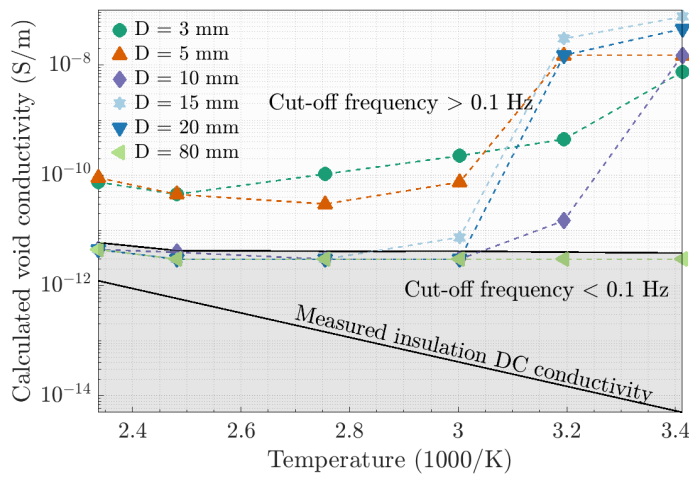
Figure 8.11: Calculated void conductivity as function of inverse temperature for indicated void diameters D.

Measured and calculated PD parameters follow the model including geometrical dimensions of the void. No other geometrical dependence was seen.

8.4   How Voltage Frequency and Temperature Dependence of PD Activity Can Be Used to Improve the Condition Assessment of Generators

Material properties, such as resulting complex permittivity and conductivity, have been measured for both laboratory objects and generator bars. The frequency and temperature dependence in the complex permittivity alone can, to a large extent, explain the different observed trends of PD features from the different test objects. Non-measurable quantities, such as void conductivity, time lag, and discharging void area, were based on a fit of measured values to the parameter of the proposed impedance abc-model.

Two testing approaches are suggested:

1. Testing at a single voltage frequency: Tests should measure the total apparent charge per period as a function of voltage. This quantity is frequency independent above 1 Hz and below 100 °C for the tested objects in this thesis. The total apparent charge as a function of voltage can estimate the capacitance in series with the voids and remanent voltage by a curve fit to the total apparent charge in Equation 2.12:

$$\sum q_{\mathrm{a}} = 4C_{\mathrm{b}}\left(U_0 - U_{\mathrm{s}}\right),$$

   where C_{b} is the related to the total discharged void electrode area, U_0 is the maximum void voltage amplitude, and U_{s} is the remanent voltage.

2. Testing at several voltage frequencies: Tests should measure the total apparent charge per period as a function of voltage and frequency. A frequency sweep can eliminate the uncertainty regarding frequency dependence and can, therefore, be beneficial. It can reveal more of the involved void physics and reduce the uncertainty from testing only at one voltage frequency. It is possible to estimate expected void conductivity from frequency-dependent values of the PDIV.

Chapter 9

Conclusions

Main Research Question:

RQ1 **Why are the measurable PD parameters PDIV, apparent charge and PD repetition rate different when applying a voltage at power frequency (50 Hz) compared to very low frequency (0.1 Hz)?**

PD parameters, such as the PDIV, maximum apparent charge, and total apparent charge are frequency and temperature dependent. The material conductivity and frequency-dependent dielectric response also varies with temperature. In the studied materials, the material conductivity contributed less ($\approx 10^3$ times) than the dielectric response and can be neglected.

The frequency and temperature dependence of PDIV can be described by the presented impedance abc-model including measured material dielectric response and calculated void conductivity. The temperature and frequency dependency of the dielectric response directly influenced the frequency dependence of the PDIV at 130 °C and 155 °C. A high dielectric response influences the voltage distribution in the insulation system with a void and effectively short-circuit the insulation material, leaving all applied voltage across the void. A high void conductivity was needed in the model to explain the high PDIV at low frequencies and temperatures below 90 °C in the laboratory objects. This high void conductivity can be related to PD by-products acting as charge carriers. The PDIV can for most cases at 50 Hz be modelled by the capacitive abc-model.

The maximum apparent charge is lower at 0.1 Hz than at 50 Hz. This frequency dependence was well modelled by a time lag in the range of 1 ms to 10 ms in the temperature range of 20 °C to 155 °C.

The total apparent charge per period was shown to be frequency independent at

temperatures below 90 °C and at frequencies above 1 Hz, whereas it was frequency-dependent at higher temperatures caused by a frequency dependence in the apparent repetition rate. This frequency dependence was modelled by relaxation of residual charges, which enables a faster recovery of the void voltage and hence more PDs during the same period. The relaxation model was based on measured dielectric response and explained the observed trend well.

Supporting Research Questions:

RQ2 **How can the measured PD parameters PDIV, apparent charge and PD repetition rate from generator bars be compared to voids with known geometry?**

Only a fraction of the void electrode area discharges in each PD. This means that there is no major difference in measuring PD activity on objects with one large discharging void electrode area or many small voids with the same total void electrode area. The use of the apparent repetition rate enables this comparison. There is a correlation between void geometry and measured PD parameters, enabling void geometry estimates based on measured PD parameters. This correlation was also indicated valid for the generator bars based on cross section microscopy.

RQ3 **What is the effect of preconditioning on measurable PD quantities?**

Voltage preconditioning lowers the PD activity. This effect vanishes as a function of time without voltage application. The time dependent effect of preconditioning was reduced to a minimum in the chosen test method and similar start conditions for the different voltage frequency tests were assumed. The chosen frequency sweep test method was, therefore, assumed to adequately show a frequency dependence of PD parameters.

Chapter 10

Suggestions for Further Work

Correlate the Creation of Voids with Ageing

This thesis did not study how different voids are created during ageing; it studied only the measurable effect from voids already present. Finding such correlations would strengthen the interpretation of test results for condition assessment.

Conduct an In-Depth Bar Dissection Study

The void distribution in generator bars should be investigated in detail. Limited available time did not enable this study in this thesis. Only void content indications based on a few cross-sections were performed.

Test Other Insulation Materials and Void Shapes

This thesis has focused on describing the frequency and temperature dependence of two insulation systems based on one material by selected models. It would strengthen the model if it were tested for more materials. It would be interesting to test a material with higher dielectric response to test an extremal situation. Other void geometries could be beneficial to test to find the limitations to the model in void geometry. It would be interesting to investigate voids in, for example, cables and see the validity for those cases, because cables are tested at 0.1 Hz due to their large capacitance but are operated at 50 Hz in service. Additionally, it would be interesting to investigate insulation systems with many known voids. This should be compared to an insulation system with one void with the same area in total. This study can reveal if it is possible to distinguish between many small and one large void with the same void electrode area.

Measure the Void Voltage

In this thesis, evidence was found that residual charges decay quickly at high temperatures, but no direct measurements were performed of this void voltage. One attempt was made to measure the void voltage, without success. Because of limited PhD time, this was not prioritised in this thesis. It could be interesting to validate the void voltage variation by experiments, as only sketches and simulations have been seen in the literature.

Measure the Void Surface Conditions

Hudon et al. [29] measured PD by-products at a plain epoxy surface. It would strengthen the model if the same were done on enclosed voids in both model insulation and bars as a function of time before and after grounding the object. It would also be interesting to correlate PD activity energy $\mathcal{E}_{PD}$ directly to a given void condition. One hypothesis is that the void conductivity is not homogeneous but have a geometrical dependency.

The almost temperature-independent time lag indicates a strong surface charge decay at high temperatures. This mechanism would be nice to measure directly to verify the model, to understand more than the indication provided here.

Investigate in Detail the Effect of Preconditioning

The effect of preconditioning was shown in this thesis to be important. It is therefore interesting to investigate the effect of preconditioning in more detail than was done here. This includes the effect of PD energy, voltage frequency, and void geometry.

Study the Partial Discharge Magnitude Histogram

This thesis has focused on the total and maximum apparent charge. It would be interesting to study PRPDA, as was done in [45] and PD magnitude histograms as briefly mentioned in this thesis.

Appendices A-D

Appendix A

Methodology Development

A.1 Ensure Homogeneous Electric Field in the Void

The abc-model requires a homogeneous electric field. It was, therefore, needed to do preliminary calculations to test the required size of the voids to avoid inhomogeneity. However, edge effects and inhomogeneity are generally accepted and treated by complex FEM models in the literature, [20], [25], and [59], instead of the simpler abc-model as is tested in this thesis. It was, therefore, more important to achieve a homogeneous electric field in this thesis than in the works comparing experimental results to complex FEM models.

A basic FEM simulation of the electric field in a cylindrical void was performed in COMSOL at capacitive conditions (50 Hz). The void gap distance was 0.5 mm and the electrode separation were 3 mm. The relative permittivity was 4.4, corresponding to epoxy in [60]. The insulation system was constructed using two perfect cylinders, with an air cylinder inside a mica/epoxy cylinder. A voltage difference between top and bottom of the mica/epoxy cylinder was applied.

The results from the basic FEM calculation of the electric field in a cylindrical void at the lines at top and middle of the cylindrical void is given in Figure A.1 for different void diameters when the gap distance fixed at 0.5 mm with 3 mm electrode separation. The field change is only present in a very small region, covering a section of approximately the outer 0.1 mm of the radius. The field enhancement at the edges are almost independent of void radius. This makes the average electric field increase with increasing void radius. Therefore, the void voltage is in this thesis assumed homogeneous for void diameters above 3 mm.
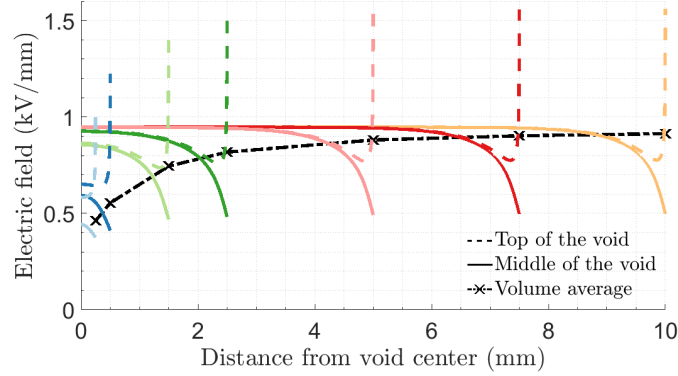
Figure A.1: Absolute value of electric field strength from FEM calculations as function of radial direction at the top and middle of a void. The object void has a void gap distance of 0.5 mm when applying 1 kV in an insulation system with a total thickness of 3 mm. The calculated volume average is indicated by a cross at the respective void radius.

The PDIV for a void gap distance of $d_c = 0.5$ mm at different void diameters was, therefore, tested at 100 Hz after preconditioning at 50 Hz for 5 min according to the preconditioning choice. The high test frequency should ensure capacitive conditions without the influence of any resistive or dielectric response parts. The temperature was varied between 20 °C and 155 °C. The results are given in Figure A.2. Despite the high frequency, results from 20 °C and 40 °C are not included due to a high PDIV, most likely caused by a high void conductivity after the preconditioning. The results show a minor void diameter dependence, meaning that the electric field in the void can be considered homogeneous at void diameters above 3 mm.
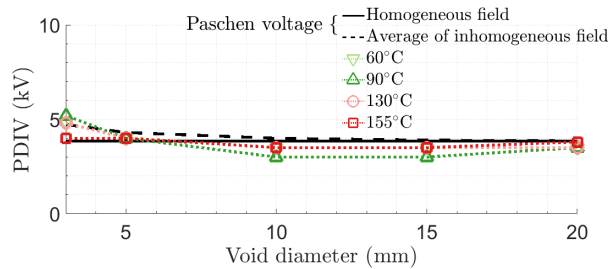
Figure A.2: Measured PDIV as a function of void diameter. The values were selected from 100 Hz measurements to reduce the influence from void conductivity and study only the electric field. The Paschen voltage based on both the homogeneous and inhomogeneous field is indicated.

A.2 Electric Field Calculation on Void Geometries Found in Generator Bars

A finite element method calculation was performed in COMSOL on a void geometry similar to the one shown in Figure 6.14a. The relative permittivity of the mica/epoxy tape was set to the measured value 3.8, including the measured strand edge radius of 0.6 mm. Figure A.3 and Figure A.4 show the result. The geometry of this void shows a field enhancement comparable to the cylindrical void in Figure A.1. This makes the electric field in the void above the Paschen field during laboratory tests, and PDs are, therefore, probable to initiate in such voids. The electric field is inhomogeneous, which is not in line with the assumption of discharging equipotential surfaces in the abc-model. The delamination in Figure 6.14e, on the other hand, is close to the parallel plane case studied by the cylindrical void.
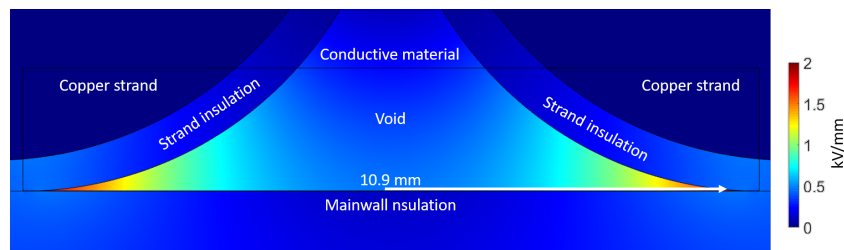
Figure A.3: Calculated electric field distribution in a void, inspired by the voids in Figure 6.14a when applying 1 kV. The mica/epoxy tape thickness is 3 mm.
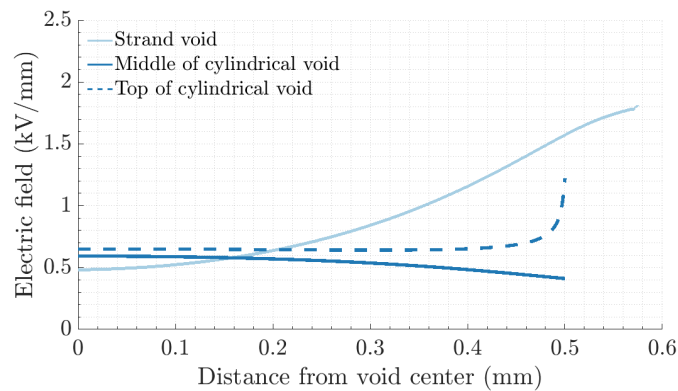
Figure A.4: Calculated electric field distribution as function of radial location. Results were obtained applying 1 kV between the copper strands and mica/epoxy tape (the lower part of Figure A.3 indicated by a white arrow) as a function of distance from the void centre (at the mica tape).

A.3 Derivation of Time Dependent Void Conductivity

Due to variations in PD activity and different ageing mechanisms occurring in the void, void parameters can change with time. Hudon et al. [29] showed that PD activity increased the epoxy surface conductivity. Later, they found this to be caused by a variety of PD by-products, such as different acids that reacted with the void air and void surface [61]. It is, therefore, expected that the PD activity reduces the void surface resistance. Such acids self-decompose with time, in particular, nitric acid [58], which means that the effect of such by-products is expected to fade with time. This means that, as a first approximation such variations are here modelled as a time-dependent void resistance $R_\mathrm{c}(t)$.

The surface conductivity is here assumed to be proportional to the concentration of free charge carriers $\mathcal{N}$ at the surface

$$\sigma_\mathrm{c} = \mathcal{N} q \mu, \tag{A.1}$$

where q is the species charge and μ the mobility. The increase in the concentration of charged species can be assumed proportional to the dissipated PD energy per unit time $\mathcal{E}_\mathrm{PD}$ as a first approximation. Additionally, the gas and surface molecules reacting to form the conductive species might be exhausted with time, and the concentration might be limited by relaxation processes. Such relaxation processes can be modelled by a relaxation time constant τ. In total, the concentration of conductive species is expected to follow the simplified differential equation based on a source term and a decay term:

$$\frac{\mathrm{d}\mathcal{N}}{\mathrm{d}t} = \mathcal{E}_\mathrm{PD} - \mathcal{N} \cdot \frac{1}{\tau}. \tag{A.2}$$

The energy source term $\mathcal{E}_\mathrm{PD}$ disappears when the object is grounded as no further PDs occur, and no new charge carriers are formed. Solving Equation (A.2) with the source term gives the build-up process when the voltage is on with a time constant τ_PD as

$$\mathcal{N}(t) = \mathcal{N}_0 \left(1 - \exp\left(-\frac{t}{\tau_\mathrm{PD}} \right) \right), \tag{A.3}$$

where $\mathcal{N}_0 = \mathcal{E}_\mathrm{PD}/\tau_\mathrm{PD}$ is the equilibrium of charged species. This equilibrium of charged species from the time with PD activity is the start value for the relaxation process after grounding the object decaying with a time constant τ_GND:

$$\mathcal{N}(t) = \mathcal{N}_0 \cdot \exp\left(-\frac{t}{\tau_\mathrm{GND}} \right). \tag{A.4}$$

A time dependent void conductivity is obtained by combining Equations (A.3) and (A.4) by Equation (A.1)

A.4   Partial Discharges from a Reference Object without Voids

The electrode arrangement was tested with insulation without voids to clarify whether the electrode arrangement itself could produce PDs. Figure A.5 presents the results from a standard frequency sweep for different temperatures. It is seen that there is no influence on PD below 130 °C, but there is some influence above. This means that voids that produce small and few PDs cannot be measured accurately at 130 °C and 155 °C. Larger voids are expected to have larger PD activity, which can mask this noise effect.

PDIV in the laboratory object without voids was above 10 kV for temperatures below 130 °C at all voltage frequencies, whereas at 130 °C and 155 °C PDIV was approximately 5 kV, which is approximately the expected PDIV for the voids.
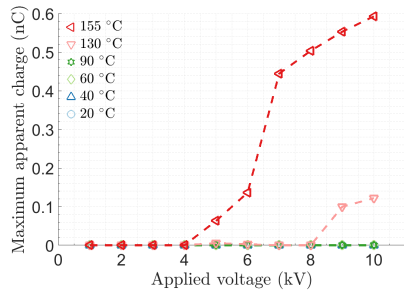
(a) Maximum apparent charge at 50 Hz as a function of applied voltage.
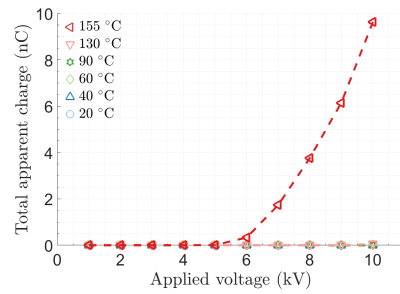
(b) Total apparent charge per period at 50 Hz as a function of applied voltage.
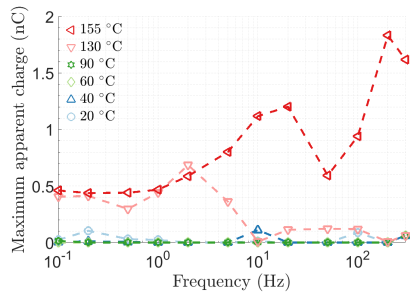
(c) Maximum apparent charge at maximum applied voltage as a function of voltage frequency.
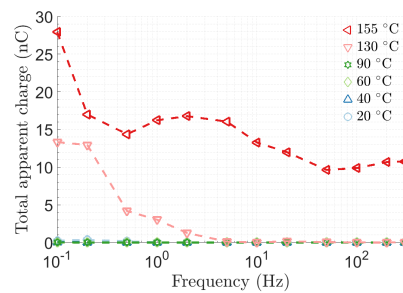
(d) Total apparent charge per period at maximum applied voltage as a function of voltage frequency.

Figure A.5: Measured total apparent charge per period and maximum apparent charge in the case of an insulation system without voids. The total insulation thickness is 3 mm.

B

Additional Experimental Results

This chapter presents additional results that are interesting, but not selected to be presented in the main results section.

B.1   Distribution of PD Magnitude in Laboratory Objects

Different void diameters produce different PD magnitude distributions, as presented in Figure B.1. The distribution of PD repetition rate per period increase in both number and maximum amplitude for increased void diameter. The apparent repetition rate, indicated by coloured markers, are almost 9 for laboratory objects with with a diameter of 5 mm, 10 mm, and 15 mm, and 20 % - 30 % lower for the cases with a void diameter of 3 mm and 20 mm. The lower apparent repetition rate for a void diameter of 3 mm can be correlated to a lower void voltage, as seen in the field calculations in Appendix A.1.
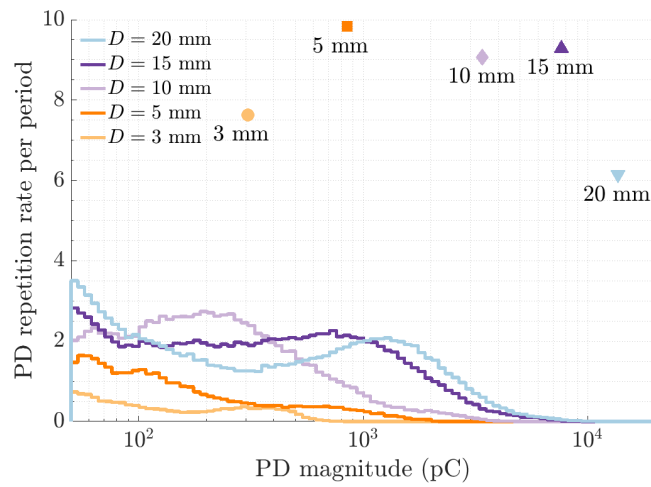
Figure B.1: Measured PD repetition rate per period (histograms) as a function of PD magnitude (solid lines) and apparent repetition rate for the same data (markers). Results were obtained at 90 °C at 50 Hz and 10 kV for objects with indicated void diameters and void gap distance of 0.5 mm.

Figure B.2 presents the PD repetition rate per period as a function of PD magnitude at indicated temperatures. The example test object was chosen to the same as before with void diameter of 10 mm and void gap distance of 0.5 mm. The overall trend is that the apparent repetition rate increases with temperature, and that the measured PD repetition rate increases in both number and maximum amplitude. Similar trends were found in the other objects with other void dimensions.
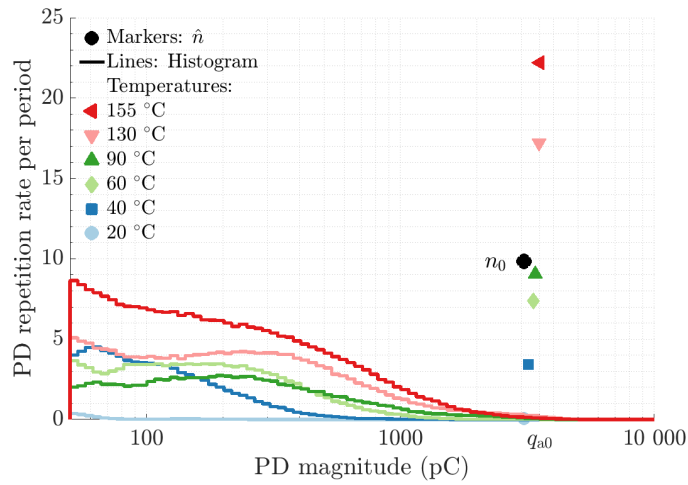
Figure B.2: Measured PD repetition rate per period (histograms) as a function of PD magnitude (solid lines) and apparent repetition rate for the same data (markers). Results were obtained at indicated temperatures at 50 Hz and 10 kV for objects with void diameter of 10 mm and void gap distance of 0.5 mm.

Figure B.3 presents the PD repetition rate per period as a function of PD magnitude at indicated frequencies. The example test object was chosen to the same as before with void diameter of 10 mm and void gap distance of 0.5 mm. The overall trend is that the apparent repetition rate is frequency independent. The measured PD repetition rate as function of PD magnitude changes with frequency. The repetition rate distribution at low frequencies has many small PDs and no large PDs. This changes as the frequency increases, to a distribution containing fewer small PDs, but correspondingly more large PDs. Similar trends were found in the other objects with other void dimensions.
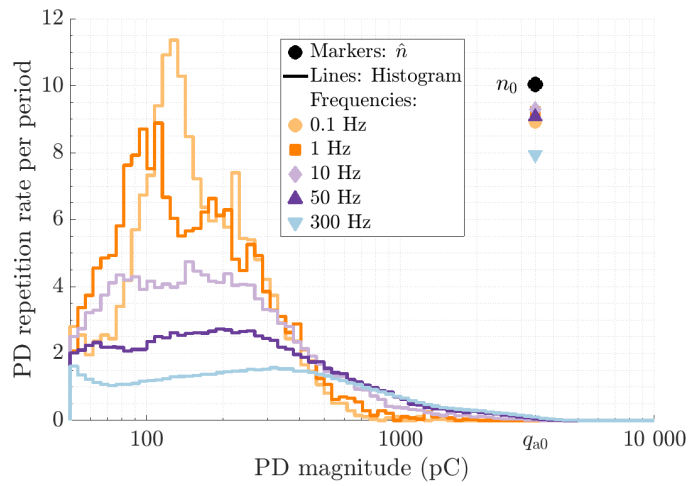
Figure B.3: Measured PD repetition rate per period (histograms) as a function of PD magnitude (solid lines) and apparent repetition rate for the same data (markers). Results were obtained at 90 °C and 10 kV at indicated frequencies for objects with void diameter of 10 mm and void gap distance of 0.5 mm.

Figure B.4 presents the PD repetition rate per period as a function of PD magnitude at indicated voltage amplitudes. The example test object was chosen to the same as before with void diameter of 10 mm and void gap distance of 0.5 mm. The overall trend is that the measured PD repetition rate below 1000 pC increases, but the distribution at larger amplitudes is voltage independent. Similar trends were found in the other objects with other void dimensions.
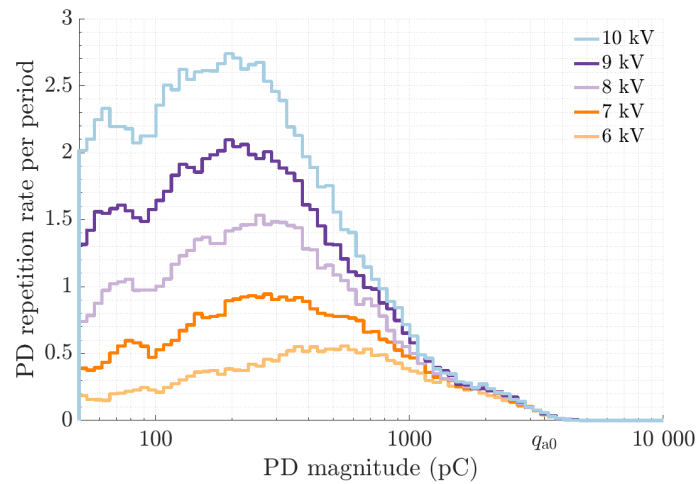
Figure B.4: Measured PD repetition rate per period (histograms) as a function of PD magnitude. Results were obtained at indicated voltage levels at 90 °C at 50 Hz for laboratory objects with void diameter of 10 mm and void gap distance of 0.5 mm.

B.2   Distribution of PD Magnitude in Generator Bars

The measured distribution of PD repetition rate per period for bars from close to the neutral terminal at the indicated temperatures are presented in Figure B.5 at 50 Hz and 10 kV. The larger magnitudes increase more in number with temperature than the smaller magnitudes. The change is similar to what was measured for the laboratory objects.
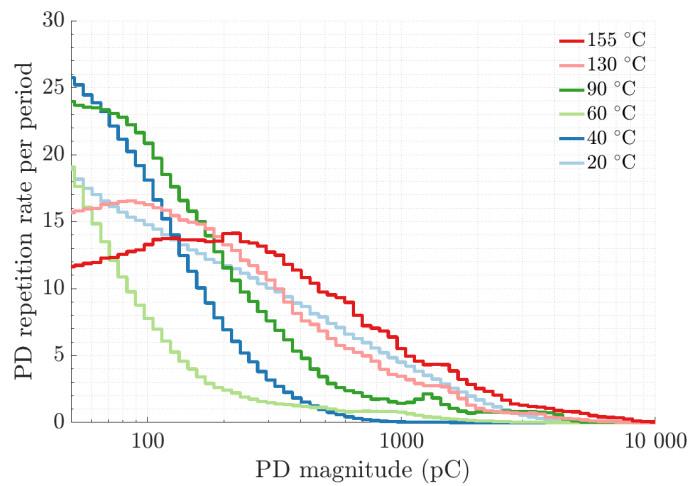
Figure B.5: Measured PD repetition rate per period as a function of PD magnitude at indicated temperatures. Results were obtained at 50 Hz and 10 kV as the average of three similar objects close to neutral terminal.

The overall shape of the apparent charge distribution increases slightly as a function of frequency, as shown in Figure B.6. The change is similar to what was measured for the laboratory objects.
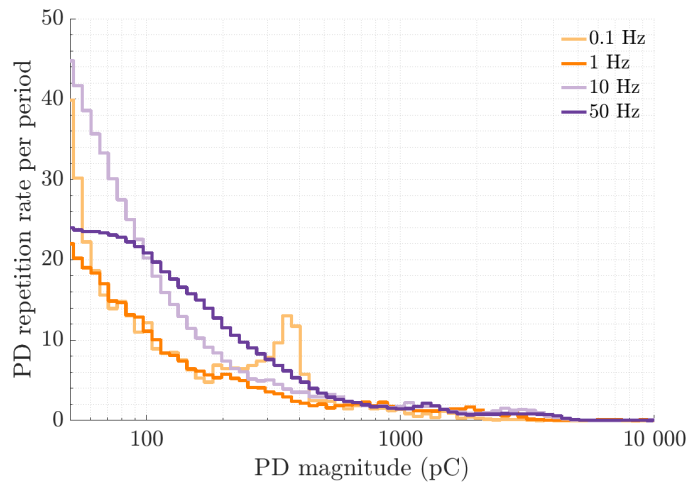
Figure B.6: Measured PD repetition rate per period as a function of PD magnitude at indicated frequencies. Results were obtained at 90°C and 10 kV as the average of three similar objects close to neutral terminal.

The apparent charge distribution increase as a function of voltage as seen in Figure B.7. The change is similar to what was measured for the laboratory objects.
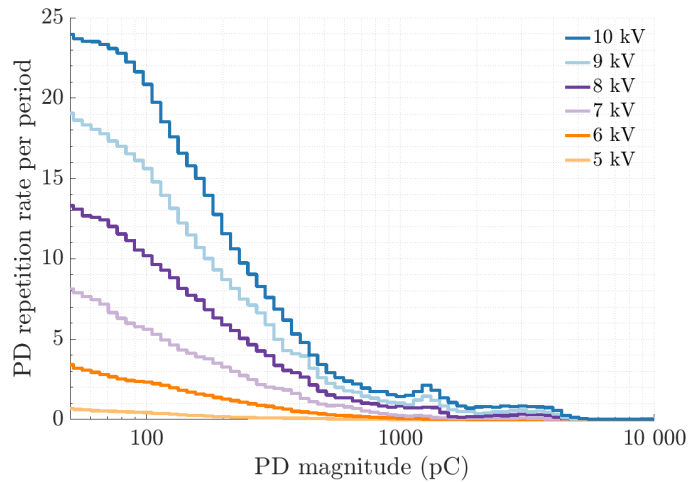
Figure B.7: Measured PD repetition rate per period as a function of PD magnitude at indicated voltages. Results were obtained at 90°C and 50 Hz as the average of three similar objects close to neutral terminal.

Appendix C

Numerical Verification of Developed Analytical Equations

C.1 Increased PD Repetition Rate in Frequency Domain

The equation describing the void voltage when including a residual charge relaxation is

$$U_0^* = U_0(t) - U_q \sum_{i=1}^{n} \exp\left(-\frac{t - t_{\mathrm{PD,i}}}{\tau}\right) \cdot u\left(t - t_{\mathrm{PD,i}}\right), \qquad (C.1)$$

where $U_0(t)$ is the sinusoidal void voltage without PDs, U_q the voltage from residual charges created in the PD events, which decay with a time constant τ, and $u\left(t - t_{\mathrm{PD,i}}\right)$ is the unit step function. The effect of residual charge relaxation is that the number of PDs are expected to increase according to the relation

$$n = n_0 \cdot f\left(\omega, \tau\right) \qquad (C.2)$$

where n_0 represents the situation without residual charge relaxation. An analytical approach to determine the function $f\left(\omega, \tau\right)$ failed. An empirical relation was therefore chosen to describe the PD repetition rate in frequency domain:

$$n = n_0 \cdot \frac{\varphi_0}{\varphi_\tau} = n_0 \cdot \frac{\left(1 - \frac{2}{\pi} \arcsin \frac{U_0}{U_s}\right)}{\frac{2}{\pi} \arctan\left(\omega \tau \cdot \frac{\pi}{2}\right)}. \qquad (C.3)$$

The nominator φ_0 represents the available time during a voltage period with a higher voltage than U_s and the denominator φ_τ represents the reduced time between PDs caused by a residual charge relaxation time constant τ. The denominator is coincidentally equal to the normalised phase difference between capacitive and resistive parts of the current in

the Thévenin equivalent of the charged void. The resistive part is caused by the charge relaxation. The validity of Equation (C.3) is shown later in this chapter by iteratively solving Equation (C.1).

C.2   Analytical Representation in Matlab

An analytical approach was developed in the theory sections to find the influence of residual charge relaxation time constant τ and time delay Δt on $q_{a,max}$ and $\sum q_a$. Because these equations were not found in the literature but developed for this thesis, a numerical approach to support the findings is provided here. Figure C.1 sketches the basic elements of the simulation:

1. The applied sinusoidal voltage with a voltage divider based on the capacitive and resistive abc-model in Equation (2.9).

2. A time lag, Δt, from the void voltage reaches the Paschen voltage U_s and the PD event happens in Equation (2.16). The time lag was implemented by using an exponential distribution $P(\Delta t) = (\Delta t_0)^{-1} \exp(-\Delta t/\Delta t_0)$ [54].

3. The PD event establishes a residual charge voltage in the void that neutralises the applied sinusoidal voltage and fixes the void voltage at a remanent voltage U_r.

4. The residual charge voltage decays with a time constant τ; $\exp(-t/\tau)$.

Table C.1 presents the parameter variation used in the simulations in this thesis. The simulation ran for 100 periods at each frequency, and the maximum apparent charge during these 100 periods and the total apparent charge per voltage period were stored and used in the analysis.
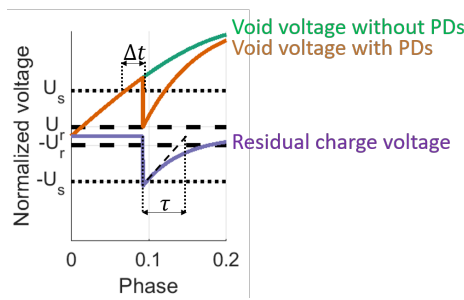
Figure C.1: Sketch of the core elements of the simulation, including time lag and residual charge relaxation.

Table C.1: Simulation parameters

Parameter name	Value	Unit
Frequency f	10^{-1} to 10^3	Hz
Relative void voltage U_0/U_s	1.87 and 4.68	1
Time delay $(\Delta t)_\mathrm{PD}$	10^{-4}, 10^{-3} and 10^{-2}	s
Relaxation time constant τ	0.01, 0.1 and 1	s

C.3 Matlab Code in Detail

Figure C.2 presents the core part of the Matlab code. Here, the main iteration is done over `nPERIODS` with `nperPERIOD` iterations per period. `Uvoid` is the void voltage as a superposition of the geometrical sinusoidal applied voltage `Uvoid0` and the residual charge voltage `Ures`. If the void voltage is greater than the pre-set threshold `BD` (e.g., based on Paschen) and a random number `rand()` is greater than a pre-set limit `rnd` representing Δt, then a void voltage collapse occurs, and the voltage is reset to the remanent voltage `Urem`. Lastly, the residual voltage decay with a time constant `tau` with the numerical time step `dtx`.

```
1  for m = 1:nperPERIOD*nPERIODS
2      Uvoid(m) = Uvoid0(m) + Ures;
3      if Uvoid(m) > BD && rand() > rnd
4          Ures = Ures − Uvoid(m) + Urem;
5      elseif Uvoid(m) < −BD && rand() > rnd
6          Ures = Ures − Uvoid(m) − Urem;
7      end
8      Ures = Ures *exp(−dtx./tau);
9  end
```

Figure C.2: Main part of the numerical Matlab code for void voltage and generating PDs.

C.4   Simulated Maximum Apparent Charge

The simulated maximum apparent charge as a function of frequency at two different applied voltages both fit well to the expected limits proportional to U_{s} at low frequencies and to $2U_0$ at high frequencies, as seen in Figure C.3.
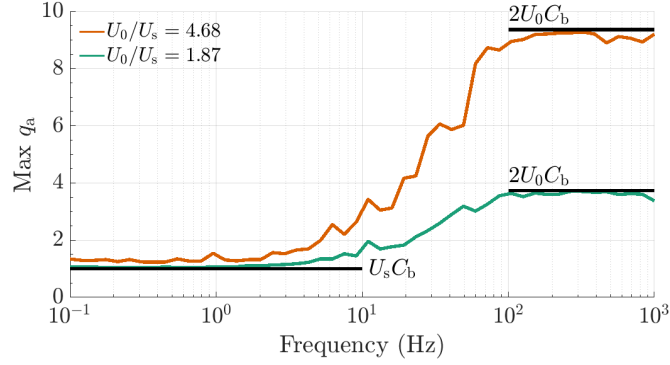
Figure C.3: Simulated maximum apparent charge as a function of frequency. Selected time lag of $\Delta t = 1\mathrm{ms}$ with a normalised maximum apparent charge of $U_{\mathrm{s}}C_{\mathrm{b}} = 1$.

Figure C.4 presents the simulated maximum apparent charge as a function of frequency for three different time lags together with a model fit. The transition from a low-frequency to a high-frequency limit is well described by Equation (2.17). The equation can, therefore, be concluded to be a good representation for the idealised void fitting the abc-models.
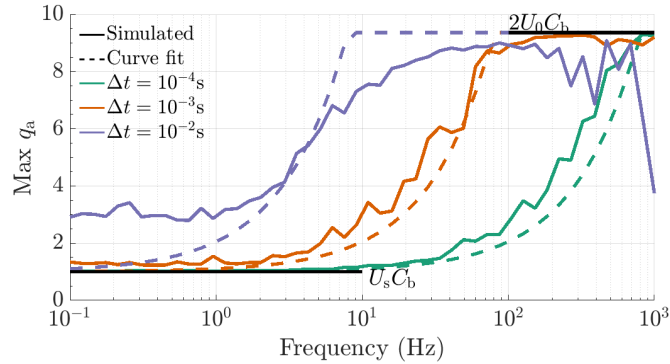
Figure C.4: Simulated maximum apparent charge as a function of frequency. Selected applied voltage of $U_0/U_{\mathrm{s}} = 4.68$ for indicated time delays together with an empirical curve fit to Equation (2.17). The empirical curve fits equally well at $U_0/U_{\mathrm{s}} = 1.87$.

C.5 Simulated Apparent Repetition Rate

Figure C.5 presents the simulated apparent repetition rate per period (proportional to total apparent charge) as a function of frequency together with the numerical model based on Equation (C.3) with no charge relaxation via RC decay in the void. The developed equation fits well to the simulated case in the idealised void. This proves numerically the use of Equation (C.3) as function of frequency to represent the fundamental Equation (C.1) describing the void voltage in time domain including n PD events.
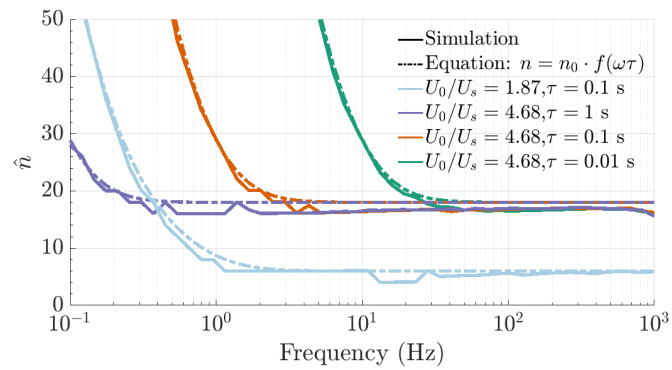
Figure C.5: Simulated apparent repetition rate as a function of frequency compared to the suggested empirical equation.

Published Papers

Paper I

T. G. Aakre, E. Ildstad, S. Hvidsten, and A. Nysveen. Review of partial discharge and dielectric loss tests for hydropower generator bars. In *2017 Nordic Insulation Symposium (NordIS)*, volume 25, 2017

Review of Partial Discharge and Dielectric Loss Tests for Hydropower Generator Bars

Torstein Grav Aakre*, Erling Ildstad*, Sverre Hvidsten** and Arne Nysveen*
*NTNU/Department of Electrical Power engineering, Trondheim, Norway
**SINTEF Energy Research, Trondheim, Norway

Abstract

Condition assessment of hydropower generators is important to ensure high serviceability of power stations. Many of the in-service generators are old and current load operation schemes demands more than the design load, which makes the remaining lifetime of the generators uncertain. The reviewed literature shows many works regarding identifying signature PRPDA patterns for different relevant defects in the generator. Calibration is however impossible, due to variable signal propagation in the generator from the partial discharge source. The results regarding complex permittivity as function of frequency as a measure on water ingress are promising. However, the field grading paint at the ends of the bars are affected by the low frequency and gives a variable capacitance. The literature is still focused on qualitative measurements without giving quantitative answers.

1. Introduction

The majority of the Norwegian hydropower generators was installed between 1960 and 1990, and many of these will soon reach their expected lifetime and therefore refurbishment is needed [1]. In addition to age, new operation loading schemes demands more than the design load, with frequent starts and stops that reduces the lifetime with an unknown quantity. To plan any replacement, it is important to know whether the bars are in a good shape, should be considered replaced or if refurbishment should be performed.

The main purpose of this review is to describe important methodologies to investigate insulation deterioration electrically. First, a description of the failure mechanisms is presented before an evaluation of the most important off-line electrical detection methods are given.

2. Electric design

Previously, until the 1970s, engineers designed generators based on experimentally based handbooks and analytical calculations. The quality of the material used were uneven and the design was therefore often over dimensioned. This can be illustrated by the fact that some generators that were installed as early as in 1920s are still in service [2]. Since then, the material quality and design tools have developed and the ratings are more accurate related to the specified operation conditions.

A detailed historical overview can be found in the review of Boulter and Stone [2]. The most important aspects are summarized in the following paragraph. The first available insulation was based on natural deposits of fibers of cellulose, silk, flax, cotton, wool and natural resins derived from trees, plants and insects and from petroleum. Mica in different shapes become popular due to its excellent withstand strength to partial discharge activity, which is inherit present in stator insulation. It was combined with different kinds of resins, in the beginning asphalt was used, and today refined and synthetic materials, such as epoxy or polyester resins are used. The mica has developed from simple mica splittings to mica paper, a product where the mica is refined and has even better properties. This development has led to thinner insulation, operating at higher electric stress with smaller safety margins.

The modern groundwall insulation in hydropower stators consists of three major parts; a barrier, a support and a filler. It is constructed as a thin tape, wrapped around the conductor in many layers, see Figure 1. The barrier material is usually mica flakes or mica paper, which has a strong resistance to partial discharges, but need mechanical support, usually provided by glass fiber, PETP film or polyester fleece. To avoid air bubbles in the tape and between the tape layers, a binder material of polyester or epoxy resin is used. The resin is usually impregnated to the rest of the insulation under vacuum and pressure, or just heated and pressurized. Additionally, the insulation system consists of outer and inner corona protection, as well as filler between the copper strands and inner corona protection layer, to reduce corona activity and preserve the shape.
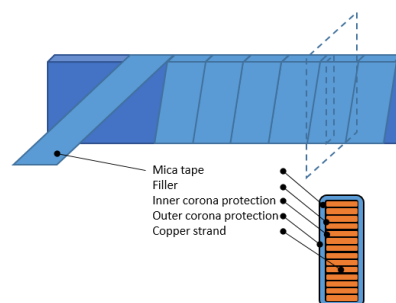

Figure 1: Physical structure of the main part of a generator bar.

3. Failure mechanisms in stator insulation

It is important to distinguish between fast and slow deterioration mechanisms to take correct action to prevent breakdown. Defects might originate during production or during service. Several different external stresses facilitate deterioration that could cause breakdown. They can be categorized in four; thermal, electric, ambient and mechanical – TEAM. These stresses, which could initiate ageing, happen often in combination, which enhances the deterioration process. The ageing process introduces localized defects and also weaken the whole material in general. It is common that stresses in combination with electric stress results in detectable partial discharges (PDs). Internal voids are impossible to avoid during the impregnation process, in which voids can cause internal discharges during voltage application. The PD from internal voids could become harmful over time. An overview of the breakdown steps caused by external stresses is given in Figure 2.
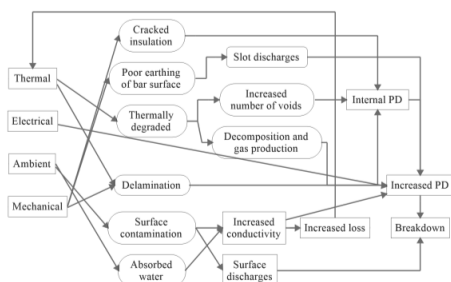

Figure 2: Different kinds of external stresses can lead to electrical breakdown via different processes.

One attempt to reveal the most frequent failure mechanisms was done by Cigré working group A1.10, who conducted a worldwide survey [3] in 2009. Sixteen utilities and one manufacturer in total of five countries replied to the questionnaire. Insulation damage, which mainly include the groundwall insulation of the winding, was reported as the largest cause of failure. The damages were mainly correlated to stator fault, 45 %, followed by insulation burning, 13 %, surface erosion, 12 %, and rotor fault, 12 %. The root cause of the insulation failure was reported as follows; 30 % suffered from ageing, 25 % had contaminations, 22 % suffered from internal partial discharge, 10 % had loosening of bars and 7 % had reported thermal cycling or overload. Fatigue of materials was reported in 16 % of the failures and loosening of rotor parts was reported in 13 %.

The most relevant standard for condition assessment of the stator insulation. is IEEE std 1434, IEEE Guide for the Measurement of Partial Discharges in AC Electric Machinery [4]. It defines three types of PD activity that are considered the most severe:
  a. Discharges in voids or delaminations within the insulation
  b. Discharges occurring between the surface of the

coil/bar and the stator core, commonly known as slot discharge
  c. Discharges in the end-winding area and circuit ring bus bar

Partial discharges are inherently present in stator insulation due to voids from the impregnation process. The most important diagnostic goal is therefore to distinguish these three harmful PD activities from the less harmfully present PDs, as the voids in aged insulation may have different behavior than voids in new insulation. Hudon et al. [5] found that no voids were observed inside the lateral side of the groundwall. All voids were at or close to the corner of the bars. This coincides with where the field enhancement occurs.

4. Diagnostic techniques used today

There exist several common methods online or offline of detecting deteriorations in insulation. Online techniques can monitor and discover trends in temperature, PD, ozone production, end winding vibration and leakage current, see e.g. the review in [6]. These monitoring techniques identifies changes in the measurements and by that indicate if the insulation deteriorations are beyond the preset safety limits. Online tests are limited by the operating voltage and measurements on a complete generator. Offline measurements with significant dismantling allows other electrical stresses to be applied, and isolating different parts of the generator from each other. Research on different mechanisms is mainly done on single bars or simple insulation systems to control the parameters. Strong offline tests include visual inspection, surface DC resistance test, PD test, $\tan\delta$ at $0.2U_N$, $0.6U_N$, $0.8U_N$ and U_N, polarization/depolarization measurements and dielectric spectroscopy. These methods have the possibility to distinguish between different failure mechanisms and indicate the severity level.

Most of the electric tests are made to describe operation at 50 Hz. A few tests consider lower frequencies, and one standard exists for this measurement [7]. However, the comparison factor between 50 Hz and 0.1 Hz are based on empirical numbers from asphalt systems and are not necessarily useful on other insulation systems.

There exist many relevant test standards, some of the most relevant are mentioned in this paper. Relevant PD tests for stator are briefly described and discussed by Stone et al. [8] in a format of a simple FAQ for a broad audience. Standardized test methods can be found in IEEE std 1434-2014 [4] and IEC 60034-18-34 [9].

The electrical tests will be empathized here. The dielectric dissipation factor and complex permittivity as function of frequency provides no indication of the distribution of the loss within the bar, whereas PD tests can give indications to which defects that are present due to their partial discharge phase resolved pattern signature (PRPDA).

5. Experience with partial discharge tests

Each defect has its own unique phase resolved partial discharge amplitude pattern (PRPDA) [10]. This and the magnitude of the PD help to identify the PD source and decide if it is necessary to take action, and it is not surprising that detection of PDs is a popular diagnostic method. Hudon et al. [10] have performed several studies regarding correlation between PRPDA and the specific defects and created a large database in Hydro Quebec as a reference for new PD measurements. A summary of the findings are compiled in Figure 3. However, the PRPDA from different sources might overlap each other when measuring on a bar or generator. This makes it difficult to uniquely determine the main PD source. IEEE std 1434 states that the user should be cautioned that no technology exists today that can uniquely identify the exact source of the defect causing PD, based on the PRPDA.

In order to get comparable results, calibration is important in all test methods. However, calibration in hydropower windings is difficult. IEC 60034-27 [11] states that it is not possible to calibrate the PD signal from the windings in machines due to pulse propagation, resonance and mutual cross coupling. This is why rotating machines are one of the few items of high-voltage equipment that do not have PD specifications [4]. Calibration procedures are then changed to normalization procedures that gives a normalized signal referred to a signal originating at the measurement spot. Absolute numbers are therefore difficult to compare between different machines due to many different designs and signal modification during signal propagation. Pattern recognition and trending are therefore preferable for diagnosis of hydropower windings.

Bélec et al. demonstrated how PD monitoring can be used to plan re-winding of a 202 MVA hydro generator [12]. The PD rate and maximum PD amplitude were stable until 2004 when it rapidly started to increase. They read this as a pre-warning and three years later, the generator was re-winded. As a comparison, the same group described another case in [13], a 184 MVA generator that suffered from slot PD. The PD monitoring showed, however, stable and high PD numbers until failure. The

PD rate and magnitude fell after re-winding, but slowly increased for 6 years until the article was published. This illustrates that PD monitoring is not always informative if the PD rate and magnitude changes slowly and are interpreted as constant. Despite this, continuously monitoring is beneficial, especially on large generators in remote areas where it is very costly to transport personnel for routine tests [14] and there is a high cost of repair.

To understand the PD mechanisms, it is necessary to investigate single bars to reduce the number of unknown variables as much as possible. Therefore, many researchers focus on varying a few parameters on single bars or model insulation systems. The variations try to mimic realistic stress that the bars might encounter during service. Hopefully, these artificial defects can give recognizable PD patterns that can give a relevant reference for later measurements with unknown source.

Generator windings are exposed to a high service voltage. An accelerated electric test could be a voltage endurance test at a higher voltage than the rating. An example of that was a test performed at 59.5 kV, both AC and DC, for up to 2200 hours until breakdown at a constant temperature of 110 °C, on six Roebel bars rated 13.8 kV [15]. PRPDA tests were performed at 8 kV AC. For AC voltage endurance, the PD count as function of time increased between 7 % and 180 % for the different bars, whereas for DC voltage endurance tests, the PD count decreased between 35 % and 60 % on the different tested bars. This indicates that AC overvoltage is more dangerous than DC overvoltage.

Voltage endurance tests at 8.3 kV/mm [16] (15 kV, 50 Hz, 2.5 times service stress) with PD monitoring show a rapid increase before a slowly decrease over a longer time. Measurements 25 h before breakdown (short relative time) show no indications of an electrical breakdown in development. This was explained by the possibility of transition from streamer to Townsend mechanism or that acids can be formed inside the gas void, that suppresses the PD activity.

PD as function of temperature was found in [16], and there was a slight increase in the PD pulse count up to the design temperature at 155 °C, where temperatures above resulted in much higher PD pulse rate. The PRPDA pattern changed slightly, but was comparable to the start. The same study used thermal cycling to mimic rapid start and stops and a temperature gradient in the insulation. The temperature of the copper conductor increases rapidly, while the temperature in the insulation increases more slowly, as it is cooled by the surrounding material. In this experiment, the bar was heated for 30 min by a current to 155 °C, and then cooled by a fan for 30 min. 155 °C was chosen because it was the design limit. The PD rate increased much until about 2000 cycles, where the increase was slower. This can indicate that the number of internal voids increased rapid until a certain saturation level.
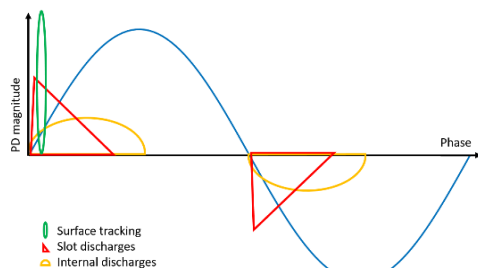

Figure 3: Typical shapes of PRPDA patterns for different defects. The PDs are mainly happening on rising edge.

Slot discharges are harmful and also one of the most frequently occurring failure modes and was therefore studied by Hudon et al. [17]. The bars were placed in slots with 0, 0.25, 0.5 and 1 mm gap. The PD magnitude and activity increased significantly for both gap size and temperature, especially above the glass transition. However, increasing the temperature, the insulation was expanded and hence the slot gap decreased. The PRPDA patterns were documented and described, but the background physics were not explained.

PDs can also be detected by high frequency (HF) methods. HF sensors can be embedded in the machine and provide non-galvanic-contact with the machine [18].

6. Experience with dielectric loss tests

The dielectric losses, or leakage currents, can be described by several quantities. The dissipation factor, $\tan(\delta)$ is the most common, especially at 50 Hz, whereas the complex permittivity or capacitance can be found in either frequency (dielectric spectroscopy) or time domain (polarization/depolarization test). In principle, it is possible to perform a Fourier transform to get to the other [19]. The focus in the following will be in the frequency domain. It could be mentioned that dielectric spectroscopy is mainly performed on single bars or coils, rather than on complete windings [6].

Farahani et al. [19] performed dielectric spectroscopy on single bars at different temperatures and during thermoelectrically ageing. The $\tan(\delta)$ curve as function of frequency changed for all frequencies. During ageing, it decreased during an initial period, before it increased. The loss increased for increased temperature, but the loss-frequency shape was preserved with just another amplitude factor. After ageing, the insulation was considered brittle and general thermal degraded.

Dielectric spectroscopy can be used to detect changes in the loss, such as a loss increase due to water ingress [20]. Water has a higher conductivity, ion dissociation and permittivity than the mica-epoxy insulation and therefore the leakage currents increase significantly. Even small quantities of water can be detected if measurements are compared with results from the sample in dry condition recorded earlier.

The generator bars have end-corona protection that acts as field grading at some parts outside the stator core. This field grading material affects the measured capacitance at low frequency and should be considered if non-guarded measurements are performed. Taylor [21] described the end-winding contribution to dielectric spectroscopy, from 0.1 mHz to 100 Hz, and the importance of guarding when measuring the main insulation. The total capacitance could increase as much as 13 % for the lowest frequencies. At power frequency, this capacitance increase was only 0.05 % at 300 V and 1.5 % at 14.4 kV.

The lower frequencies let the high voltage potential to be over a larger area than at higher frequencies.

PDs increase the losses in the insulation. These losses are more significant at a high voltage than at lower. The tip-up method is to compare the 50 Hz $\tan(\delta)$ value at 0.2 U_N and 0.6 U_N. IEC 60034-27-3 [22] describes dielectric dissipation factor measurement on stator winding insulation of rotating electrical machines. By comparing the machine to itself, the variance between different units are eliminated. The main goal is to reveal voids that create PDs or other mechanisms that increase the loss. When the PD rate is too high, the conventional PD measurement systems do not count all. The dissipation factor is a measure on the average and can be suitable to indicate the total number of voids present in the insulation [16]. A too high PD rate could also result in a constant PD current, which is not possible to trig and give individual PDs.

Cimino et al. [23] used tip-up test to verify decreased strength at bending points of a bar. They vibrated a bar, while fixing one side. The contact point where the bending angle were largest suffered from the highest loss increase. The tip-up test revealed that voids, delamination or cracks were created due to the vibration.
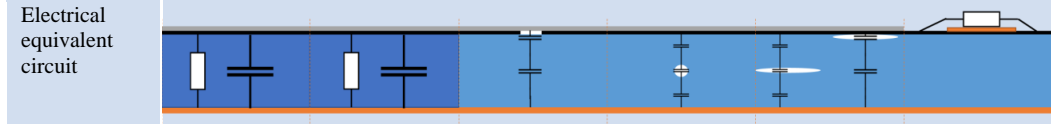
The standard, IEC 60034-27-3 describes a limit for allowed tip-up value. Sedding et al. [24] discussed this standard and questioned the limit. They think that more work is needed to verify or disprove the values. 210 stator coils and bars were tested and all met the 2 % requirement, but a significant number did not meet the 0.5 % tip-up requirement. This made them question if the limits were set too conservative.

7. Interpretation of the measured results

When online measurements of PD, ozone generation or temperature have detected significant changes in trending, offline measurements need to be performed to further investigate the generator and identify the root cause of the measurement. Offline tests can be performed with variable degree of dismantling. The more dismantling, the more certain about the defect location. However, this is a costly process and is only performed if necessary. It is then necessary to have accurate correlations between defect and measured result to identify possible root causes of the measurement.

Different defects produce different PRPDA that acts as signatures for the specific defect. This helps in condition assessment to identify the defect. The comprehensive study by Hudon et al. [10] provides a useful background for comparing different PRPDA patterns. However, different defects have overlapping PRPDA and it could be difficult to distinguish between the different defects. Research is therefore performed on single bars to control the variables and from that know the relation between failure and measurement. Slot gap distances are varied,

Table 1: Summary of the different deterioration mechanisms.

	Thermal	H2O	Slot	Void	Delamination	Surface
Electrical equivalent circuit						
Model	Resistance in parallel with a capacitance	Resistance in parallel with a capacitance	Two capacitors in series	Three capacitors in series	Two/three capacitors in series	Variable surface resistor
Ageing	Number of voids increases, overall condition is weakened	% of water increases, overall condition is weakened	The slot gap expands	The void expands or more arise	The delamination expands	More contaminations
Characteristic	The effective resistance is lowered	The effective resistance is lowered	Relative C in slot decreases, PD occurs	Relative C in void decreases, PD occurs	Relative C in void decreases, PD occurs	Conductivity and E increases, PD occurs
Preferred diagnostic method	Permittivity, tan(δ), PD	Permittivity, tan(δ)	PD, PRPDA, rate and magnitude	PD, PRPDA, rate and magnitude	PD, PRPDA, rate and magnitude	PD, PRPDA, rate and magnitude

temperature increased and lowered, deterioration by bar vibration, artificial voids inserted to the insulation and voltage endurance tests to describe how the defects can be measured. However, no detailed physical explanation of the measured signals has been presented.

The measurement of dielectric losses by dissipation factor or complex permittivity/capacitance is a useful tool to measure the overall condition of the generator bar. It is a good measure on leakage currents that might arise. These currents might originate from water ingress, overall more PD activity or just a general deterioration of the insulation strength. The loss-frequency curve might be compared to known loss sources and from that identify the source and perform the correct action.

There exists no complete physical explanation of the breakdown and pre-breakdown process and signal propagation within the bar. Therefore, absolute numbers for acceptance criteria are not proposed in the reviewed literature. This results in the limited test evaluation that trend changing of the variables for the same unit are more informative than comparing the absolute numbers with other generators. A summary of the described mechanisms and preferred detection methods is given in Table 1.

A condition assessment should reveal insulation defects before they cause breakdown. To do so, it is important to know which measured physical state that characterizes ageing, contaminations and internal partial discharges. When the physical state of these defects is known, it is possible to correlate the measured signal and the root cause of the signal. This leads to increased reliability of condition assessment and reduces the risk of unexpected breakdown.

8. Conclusion

Electrical condition assessment is currently performed on hydropower stator bars by mainly partial discharge, insulation resistance, dissipation factor and complex permittivity measurements. Partial discharges can give indications of the maximum void size or most severe defect and also the location. The phase resolved amplitude plot is a strong characteristic of which defect that causes the PD. Each source has each own signature and analyses can substantiate which faults that are present based on a PRPDA plot. The resistance measurement, dissipation factor and complex permittivity are measuring leakage currents. Whereas the resistance measurement is based on DC, the dissipation factor and complex permittivity can be found for a variety of frequencies. The frequency variation gives more information about the defect source and it is possible to identify the source. Water ingress and enlarged PD activity can be detected by frequency varied measurements. The physical explanation of deteriorations and how to make measurement are mainly qualitative in the literature. More research is needed to explain the quantitative relations and give a complete physical explanation.

9. Acknowledgement

10. References

[1] T. M. Sneve, "Aldersfordeling for komponenter i kraftsystemet, levetid og behov for reinvesteringer (norwegian)," *NVE,* vol. 8-2005, 2005.

[2] E. A. Boulter and G. C. Stone, "Historical development of rotor and stator winding insulation materials and systems," *IEEE Electrical Insulation Magazine,* vol. 20, no. 3, pp. 25-39, 2004.

[3] *Survey of Hydrogenerator Failures*. WG A1.10 CIGRÉ Technical brochure No. 392, 2009.

[4] *IEEE Std 1434-2014 (Revision of IEEE Std 1434-2000), IEEE Guide for the Measurement of Partial Discharges in AC Electric Machinery*, 2014.

[5] C. Hudon, M. Levesque, D. H. Nguyen, C. Millet, and F. Truchon, "Root cause analysis of generator failures," in *Conference Record of IEEE International Symposium on Electrical Insulation*, 2012, pp. 199-203.

[6] G. C. Stone, "Condition monitoring and diagnostics of motor and stator windings - A review," *IEEE Transactions on Dielectrics and Electrical Insulation,* vol. 20, no. 6, pp. 2073-2080, 2013.

[7] *IEEE Std 433-2009 (Revision of IEEE Std 433-1974), IEEE Recommended Practice for Insulation Testing of AC Electric Machinery with High Voltage at Very Low Frequency*, 2009.

[8] G. C. Stone, M. K. W. Stranges, and D. G. Dunn, "Common Questions on Partial Discharge Testing: A Review of Recent Developments in IEEE and IEC Standards for Offline and Online Testing of Motor and Generator Stator Windings," *IEEE Industry Applications Magazine,* vol. 22, no. 1, pp. 14-19, 2016.

[9] *IEC TS 60034-18-34:2000, Functional Evaluation of Insulation Systems - Test Procedures for Form-Wound Windings - Evaluation of Thermomechanical Endurence of Insulation Systems*, 2000.

[10] C. Hudon and M. Bélec, "Partial discharge signal interpretation for generator diagnostics," *IEEE Transactions on Dielectrics and Electrical Insulation,* Article vol. 12, no. 2, pp. 297-319, 2005.

[11] *IEC TS 60034-27:2006, Off-line partial discharge measurements on the stator winding insulation of rotating electrical machines*, 2006.

[12] M. Bélec, C. Hudon, C. Guddemi, and D. N. Nguyen, "A case study of condition-based maintenance of a 202-MVA hydro-generator," in *Proceedings of 2008 International Conference on Condition Monitoring and Diagnosis, CMD 2008*, 2008, pp. 163-166.

[13] M. Bélec *et al.*, "Investigation and diagnosis of a 184-MVA air-cooled generator heavily affected by slot partial discharge activity," in *2007 Electrical Insulation Conference and Electrical Manufacturing Expo*, 2007, pp. 85-90.

[14] G. C. Stone, B. Lloyd, and M. Sasic, "Experience with continuous on-line partial discharge monitoring of generators and motors," in *2008 International Conference on Condition Monitoring and Diagnosis*, 2008, pp. 212-216.

[15] M. Bélec, C. Guddemi, and C. Millet, "Effect of long-term aging test under DC voltage on Roebel bars," in *Condition Monitoring and Diagnosis (CMD), 2012 International Conference on*, 2012, pp. 412-416.

[16] M. Farahani, H. Borsi, E. Gockenbach, and M. Kaufhold, "Partial discharge and dissipation factor behavior of model insulating systems for high voltage rotating machines under different stresses," *IEEE Electrical Insulation Magazine,* vol. 21, no. 5, pp. 5-19, 2005.

[17] C. Hudon, M. Bélec, and M. Lévesque, "Study of slot partial discharges in air-cooled generators," *IEEE Transactions on Dielectrics and Electrical Insulation,* Article vol. 15, no. 6, pp. 1675-1690, 2008, Art. no. 4712672.

[18] G. C. Stone, C. Chan, and H. G. Sedding, "Relative ability of UHF antenna and VHF capacitor methods to detect partial discharge in turbine generator stator windings," *IEEE Transactions on Dielectrics and Electrical Insulation,* vol. 22, no. 6, pp. 3069-3078, 2015.

[19] M. Farahani, H. Borsi, and E. Gockenbach, "Dielectric response studies on insulating system of high voltage rotating machines," *IEEE Transactions on Dielectrics and Electrical Insulation,* vol. 13, no. 2, pp. 383-393, 2006.

[20] T. P. Hong, O. Lesaint, and P. Gonon, "Water absorption in a glass-mica-epoxy composite - [I: Influence on Electrical Properties]," *IEEE Transactions on Dielectrics and Electrical Insulation,* Article vol. 16, no. 1, pp. 1-10, 2009, Art. no. 4784545.

[21] N. Taylor, "Measured and modeled capacitance, loss and harmonics in stator insulation with nonlinear stress control," *IEEE Transactions on Dielectrics and Electrical Insulation,* Article vol. 22, no. 6, pp. 3133-3145, 2015, Art. no. 7367506.

[22] *IEC 60034-27-3:2015, Dielectric dissipation factor measurement on stator winding insulation of rotating electrical machines*, 2015.

[23] A. Cimino, C. Foelting, F. Jenau, and C. Staubach, "Analysis of localized dissipation factor measurements on the insulation system of mechanically aged generator stator bars," in *2016 IEEE International Conference on Dielectrics (ICD)*, 2016, vol. 2, pp. 674-677.

[24] H. Sedding, G. Stone, and A. Shaikh, "Dielectric dissipation factor acceptance criteria for stator winding insulation," in *2016 IEEE International Conference on Dielectrics (ICD)*, 2016, vol. 2, pp. 955-958.

Paper II

T. G. Aakre, E. Ildstad, and S. Hvidsten. Condition assessment of hydrogenerator stator bar insulation using partial discharge measurements. In *Electrical Insulation Conference, EIC 2018*, 2018

Condition Assessment of Hydrogenerator Stator Bar Insulation using Partial Discharge Measurements

Torstein Grav Aakre
Department of Electric Power Engeneering
Norwegian University of Science and
Technology (NTNU)
Trondheim, Norway
torstein.aakre@ntnu.no

Erling Ildstad
Department of Electric Power Engeneering
Norwegian University of Science and
Technology (NTNU)
Trondheim, Norway

Sverre Hvidsten
Department of Electric Power Technology
SINTEF Energy Research
Trondheim, Norway

Abstract—**This paper presents results from laboratory measurements of partial discharge (PD) activity in 50 cm long samples cut from the mainwall section of old hydrogenerator stator bars. All stator bars were manufactured in 1976 and samples were taken after 35 years in service from both the low and high voltage sections of the generator, as well as non-energized back-up bars. The PD activity, using a phase resolved (PRPDA) measuring system, was investigated at different test voltages up to 9.6 kV (1.5 U_0), frequencies and temperatures in the range 20-155 ˚C and 0.1-50 Hz, respectively. The service-aged and the unaged reference samples showed a clear difference in voltage frequency dependence. It was, however, not possible to distinguish between service-aged bars from high and low electric stress. The observed frequency and temperature dependences are discussed with respect to theoretical assumptions regarding possible void degradation and surface conductivity.**

Keywords— Hydropower, partial discharges, variable voltage frequency

I. INTRODUCTION

Condition assessment of hydrogenerator stator bars, based on detection of changes in partial discharge (PD) activity are performed either as online or offline measurements. During PD-testing of installed generators, the temperature varies with the current load or time after shutdown. It is usually beneficial to perform offline PD tests at low frequency (0.1 Hz) due to the large capacitance in the generator windings, keeping the test equipment small. Although, several standardized test procedures are available [1-3] it is unclear how PD results obtained at 0.1 Hz relate to results measured at 50 Hz, see e.g. [4, 5].

One example of results from trend analysis of online PD monitoring is given by Bélec et al. [6]. In case of large change in PD characteristics, a more detailed examination of the generator revealed the presence of slot discharges. Based upon this, it was decided to rewind the generator. In case of considering and comparing the quality of large number of generators, statistical analysis of PD measurements are used to locate the critical generators suggested for further more detailed investigations [7]. An alternative approach is to use measured phase resolved PD signatures (PRPDA) to build a database of possible PD sources, for example Hudon et al. [8].

The main purpose of this paper is to examine experimentally, how PD features change with applied voltage frequency and temperature and examine if the variable voltage

frequency PD technique can be used as a diagnostic tool for stator bars.

II. THEORY REGARDING VOID DISCHARGES

PDs occur when the voltage across voids exceeds its threshold value and a starting electron is available. This means that the PD inception voltage strongly depends on void shape, size and availability of starting electron. Charge is deposited during a PD, opposing the applied field.

The apparent PD charge q_a, which can be measured by an external circuit, can approximately be expressed as

$$q_a = b \cdot \Delta U \tag{1}$$

where b according to the well-known abc equivalent of the test object is the insulation capacitance in series with the void. It is assumed that the test object capacitance, a, is much larger than the void capacitance. ΔU is the voltage change across the void during the PD occurrence.

In order to consider possible effects of testing at low frequencies the deposited charge q_i is here considered to decay exponentially

$$\frac{dq_i(t)}{dt} = -\frac{1}{\tau} q_i \tag{2}$$

where τ is a time constant given by

$$\tau = \frac{\varepsilon}{\sigma} \tag{3}$$

where σ is the resulting apparent conductivity and ε the permittivity.

A statistical time lag influence the voltage ΔU and is more pronounced at higher frequencies, where a certain delay before initiation gives a PD at a higher voltage. The influence of statistical time lag on frequency behavior is e.g. described in the experimental and numerical work in polycarbonate by Forssén et al. [9]. Here a statistical time lag in the millisecond range was used to describe an increase in PD magnitude with applied voltage frequency.

In case of varying the frequency of the applied voltage, three different cases may occur:

I. The time constant is much smaller than the voltage half cycle. Deposited charge decay fast.

II. The time constant is at the order of the voltage half cycle. Deposited charge decay to some extent and is frequency dependent.

III. The time constant is much larger than the voltage half cycle. Deposited charge do not decay.

The PD repetition rate is limited by how fast the void voltage is restored. This means that a higher PD repetition rate is expected in case I than in case II than in case III. The frequency dependence is however expected to be the same, a decreasing PD repetition rate with increasing frequency.

The PD magnitude is, according to equation (1), dependent on a voltage difference and a capacitance. If the complete void participates in the PD, i.e. b constant, then the only factor influencing the PD magnitude is the voltage ΔU. This means that all three cases should have PD magnitude increasing with increasing frequency that are at the same level.

According to equation (3), the time constant is inversely proportional to the resulting conductivity, which is commonly assumed to increase with temperature following Arrhenius law

$$\sigma \propto e^{-\frac{E_a}{k_B T}} \qquad (4)$$

where E_a is the activation energy, k_B the Boltzmann constant and T the temperature in Kelvin.

It is reasonable to assume that the rate of degradation caused by PD activity is proportional to the PD energy dissipated. Therefore, the PD power P is here presented to facilitate comparing results from test objects differently aged; calculated according to

$$P = \frac{1}{\Delta t} \sum_i U_i \cdot q_{a,i} \qquad (5)$$

where Δt is a reference time creating either per period or per time unit and U_i is the momentary voltage at the time instant the PD of apparent measured charge $q_{a,i}$.

III. Methodology

A. Test samples

All 50 cm long test samples were cut from the main-wall insulation of old hydrogenerator stator bars ($U_0 = 6.4$ kV), manufactured in 1976 and taken after 35 years in service. Three samples were taken close to HV terminal, three samples close to neutral terminal and three samples were non-energized back-up bars.

The bars were insulated by mica paper tape with non-woven glass reinforcement, PET film and polyester binder. The 50 cm long test objects had a resulting capacitance of about 400 pF. The surface of 12 cm at each end was painted with end corona protection, CoronaShield P8001, to reduce the electric field and prevent external PDs at the terminations.

B. Measuring principle and test procedure

The test setup consisted of a standard PD detection circuit, schematically shown in Fig. 1, consisting of a measurement impedance, Z, Omicron CPL 542A in series with a coupling
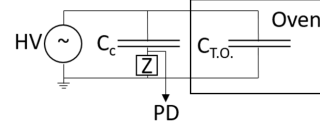

Fig. 1: Test setup. The circuit is fed by a high voltage variable frequency generator, TREK. The coupling capacitance is in series with the measurment impedence Z. The test object $C_{T.O.}$ is placed within an oven.

capacitance, C_C, of 3.4 nF. The samples were clamped between grounded copper plates to simulate the stator slot.

The bars were initially electrically stressed at the maximum test voltage of 9.6 kV (1.5 U_0, where U_0 is the line voltage of 6.4 kV_{RMS}) for 5 minutes at power frequency (50 Hz) as suggested in IEEE std 1434 [3]. During PD testing the voltage was increased from zero voltage to 1.5 U_0 in voltage steps of 0.15 U_0. The voltage was kept constant at each step for the longest of either 10 s or 10 periods. This procedure was immediately repeated for all frequencies, in decreasing order to 0.1 Hz, with the conditioning period reduced to 5 s. The conditioning period also served as a test to control if results from 50 Hz energizing changed during the frequency sweep.

An automated computer controlled test equipment was developed to facilitate PD measurements as a function of voltage magnitude, applied frequency in the range 50 - 0.1 Hz and temperature in the range 20 - 155 ˚C.

During a voltage step, the average of the 10 largest apparent discharges, above a threshold of 20 pC, was noted as the maximum apparent charge. This was done to reduce the influence of noise and large single-occurring PDs. Mean values and error bars in the figures are based on three similar samples per data point.

IV. Results and Discussion

All tested stator bars were produced for the same hydropower generator and it is reasonable to assume that they

a) Unaged back-up bar, 0.1 Hz measurement

b) Unaged back-up bar, 50 Hz measurement

c) Service-aged near HV terminal, 0.1 Hz measurement
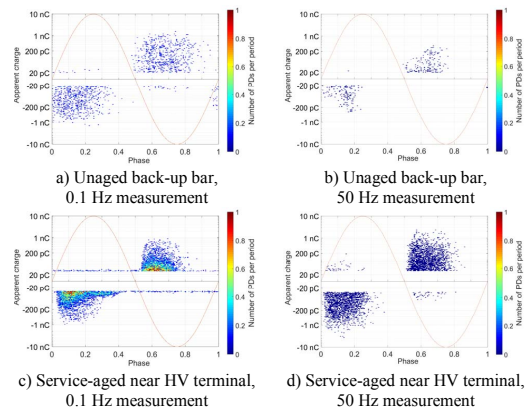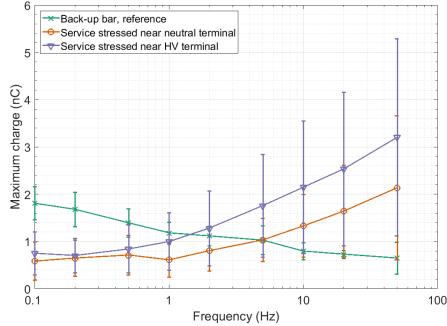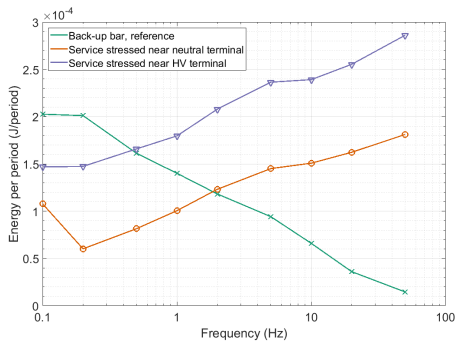
d) Service-aged near HV terminal, 50 Hz measurement

Fig. 2: PRPDA for 10 periods for back-up bars and in-service-aged bars from near HV terminal measured at U_0. Measured at both 0.1 Hz and 50 Hz. Normalization of PD numbers to PDs per period. The integration settings are in the time domain. ±100ns.

a) Maximum charge

b) Average dissipated energy per period. ERRORBARS are not included because the standard deviation for service aged bars are 100 % and 20 % for the back-up bars.
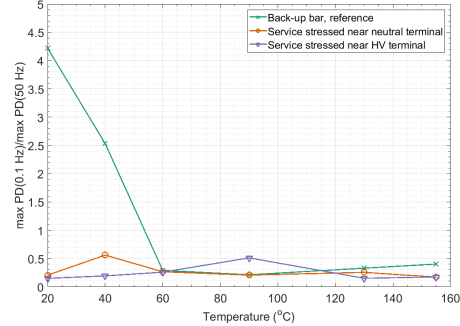
Fig. 3: Measurements of maximum charge and dissipated energy per period measured at 20 °C at U_0.

a) Ratio of maximum charge at 0.1 Hz and 50 Hz

b) Ratio of dissipated energy (P) per period at 0.1 Hz and 50 Hz

Fig. 4: Ratios of measured dissipated energy and maximum charge versus temperature measured at U_0.

were originally similar. Differences must therefore have been introduced during service. Typical PRPDA figures, measured for 10 periods at U_0 and 0.1 Hz and 50 Hz, are shown in Fig. 2. The PRPDAs are symmetric in the polarity, showing internal PDs, and there are more PDs per period at 0.1 Hz than at 50 Hz, as expected. The service-aged bars have more PDs per period than the back-up bars, indicating a higher conductivity as described in the presented cases in the theory section. This indicates that the conductivity has increased during service.
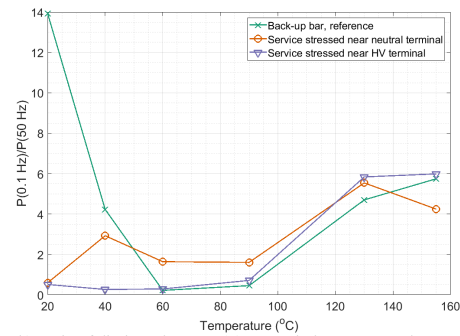
The overall shape of the PRPDA at both 0.1 Hz and 50 Hz are comparable. Measurements at 0.1 Hz energize a larger area due to the field grading paint at the ends of the bar. This is however considered insignificant. Differences were seen between the service-aged and unaged samples. No significant differences were observed between service-aged samples near neutral or HV terminal.

A. Applied frequency dependence,

Results presented in Fig. 3 show the maximum PD charge and dissipated energy per period as function of frequency. The magnitude of the apparent PD charge for the service-aged samples increase with frequency, in good agreement with the presented theory. The dissipated energy is a combined number, dependent on repetition rate and magnitude. Low frequencies

give many small PDs and higher frequencies give larger PDs, but fewer. It is therefore reasonable that the dissipated energy increases with frequency, as seen here with the mean value.

The unaged back-up bars were found to have a decreasing PD magnitude with increasing frequency. The dissipated energy is also decreasing with increasing frequency. This is not in accordance with the presented theory. One important assumption in the theory section was that the capacitance b is constant for all frequencies. It seems that the discharging area of the voids in the unaged back-up bars is frequency dependent. A larger area is discharged at lower frequencies than at higher frequencies.

B. Test temperature dependence

The graphs presented in Fig. 4 show the ratio of the maximum charge and dissipated energy per period. The ratio is found by dividing the value at 0.1 Hz by the value at 50 Hz. This is a compact method to describe the trends presented in Fig. 3 as function of temperature.

All samples show the same trend as function of frequency when the temperature is above 60 °C. PD magnitudes at 50 Hz are larger than at 0.1 Hz for all samples, but the ratio between them varies. The same is valid for dissipated energy, but with values at 0.1 Hz larger than at 50 Hz. The presented theory is valid for this temperature range. The back-up bars differ significantly from the service-aged bars below 60 °C where the

values at 0.1 Hz are larger than at 50 Hz and the presented theory cannot explain this.

The dissipated energy per period above 90 ˚C is significantly larger at 0.1 Hz than at 50 Hz. This might be related to a very high conductivity at high temperatures, as described in equation (4). This gives a low time constant that allows deposited charges to decay almost instantaneously and a high PD repetition rate occurs.

The service-aged bars close to neutral terminal have a higher mean dissipated energy per period at 0.1 Hz than at 50 Hz at all temperatures. The bars close to HV terminal have a higher dissipated energy per period at 50 Hz than at 0.1 Hz below 100 ˚C, indicating a possible difference between service aging with and without voltage stress.

C. Applied voltage dependence

Maximum PD magnitude as function of applied voltage at 20 ˚C and 60 ˚C for the back-up bars is presented in Fig. 5. Which frequency that gives the highest PD magnitude is dependent on the applied voltage. There is no difference between PD magnitude at 0.1 Hz and 50 Hz below 4 kV. This statement is also valid for the service-aged bars.

Above 7 kV, the PD magnitude at 0.1 Hz becomes temperature independent, whereas the 50 Hz values differ significantly as function of temperature. The PDIV is lower at 20 ˚C than at 60 ˚C, indicating that the void conditions are changed at different temperatures.

D. Sample differences

The observed difference in maximum PD magnitude and dissipated energy indicate that the void conditions of the unaged and service-aged samples are different. These differences could originate in various void types or void degradation due to service ageing. The large spread (up to 100 %) for the service-aged bars makes it difficult to distinguish between samples from high and low voltage. This might however indicate that thermal ageing is more dominant than electrical ageing.
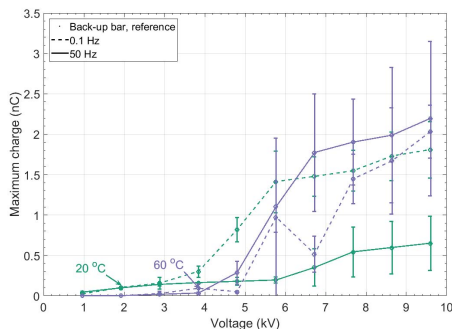

Fig. 5: Maximum charge for the back-up bar as function of applied voltage, measured at 20 ˚C and 60 ˚C at both 0.1 Hz and 50 Hz.

The back-up bars show a lower spread in the results than the service-aged bars. This might indicate that the service ageing of the insulation is not the same in the whole generator. It is however possible to distinguish between the service-aged bars if neglecting the spread in the results. Then, the bars from close to HV terminal produce higher PD magnitude and dissipates more energy per period. This might be a possible difference between the service-aged bars, but a much larger population than three samples must then be tested to reduce the spread and make a conclusion.

V. CONCLUSION

1. Based upon PD-measurements, it is possible to distinguish the service-aged bars from the back-up bars using their maximum apparent charge and dissipated energy as function of voltage frequency and magnitude.

2. No significant difference in PRPDA was observed between service-aged bars exposed to low and high voltage for 35 years.

3. Frequency sweeps give valuable information that is not revealed testing at one voltage frequency only.

REFERENCES

[1] IEC TS 60034-27:2006, Off-line partial discharge measurements on the stator winding insulation of rotating electrical machines, 2006.

[2] IEEE Std 433-2009 (Revision of IEEE Std 433-1974), IEEE Recommended Practice for Insulation Testing of AC Electric Machinery with High Voltage at Very Low Frequency, 2009.

[3] IEEE Std 1434-2014 (Revision of IEEE Std 1434-2000), IEEE Guide for the Measurement of Partial Discharges in AC Electric Machinery, 2014.

[4] C. Forssen and H. Edin, "Partial discharges in a cavity at variable applied frequency part 1: measurements," IEEE Transactions on Dielectrics and Electrical Insulation, vol. 15, no. 6, pp. 1601-1609, 2008.

[5] A. Cavallini and G. C. Montanari, "Effect of supply voltage frequency on testing of insulation system," IEEE Transactions on Dielectrics and Electrical Insulation, Conference Paper vol. 13, no. 1, pp. 111-121, 2006.

[6] M. Bélec, C. Hudon, C. Guddemi, and D. N. Nguyen, "A case study of condition-based maintenance of a 202-MVA hydro-generator," in Proceedings of 2008 International Conference on Condition Monitoring and Diagnosis, CMD 2008, 2008, pp. 163-166, 2008.

[7] C. Hudon, N. Amyot, M. Levesque, M. Essalihi, and C. Millet, "Using integrated generator diagnosis to perform condition based maintenance," in 33rd Electrical Insulation Conference, EIC 2015, pp. 341-345, 2015.

[8] C. Hudon and M. Bélec, "Partial discharge signal interpretation for generator diagnostics," IEEE Transactions on Dielectrics and Electrical Insulation, Article vol. 12, no. 2, pp. 297-319, 2005.

[9] C. Forssen and H. Edin, "Partial discharges in a cavity at variable applied frequency part 2: measurements and modeling," IEEE Transactions on Dielectrics and Electrical Insulation, vol. 15, no. 6, pp. 1610-1616, 2008.

Paper III

T. G. Aakre, E. Ildstad, and S. Hvidsten. Time development of voltage frequency dependence of partial discharge activity in voids. In *Nordic Insulation Symposium (NordIS)*, volume 26, 2019

Time Development of Voltage Frequency Dependence of Partial Discharge Activity in Voids

T. G. Aakre[1], E. Ildstad[1] & S. Hvidsten[2]
[1]NTNU/ Department of Electrical Power Engineering, Trondheim, Norway
[2]SINTEF Energy Research, Trondheim, Norway

Abstract

Condition assessment of high voltage equipment based on partial discharge measurements is often performed after a voltage pre-conditioning period. The aim of this paper is to present results from experimental examinations of time variance of partial discharge activity and to propose physical explanations of the phenomena observed. Experiments were performed on laboratory made 3 mm thick discs of generator bar insulation, consisting of mica and glass fiber reinforced epoxy with a 0.5 mm thick cylindrical void surfaces of 10 mm in diameter. The effect of conducting and insulating void surfaces was examined using copper tape as upper and lower electrodes of the voids. All objects were tested by 12 one-minute long AC voltage frequency sweeps at frequencies from 50 Hz to 0.1 Hz distributed in time from start of the experiment, after initial one-hour constant 50 Hz voltage application and during object short-circuiting for 20 h. The main result shows that in case of insulating voids the apparent charges vanished after the one-hour constant 50 Hz voltage application. After a grounding period of 5 minutes, the charge magnitudes slowly increased with time until reaching steady state after about 4-8 hours. Test objects with conductive void surfaces showed such reduction in case of PD testing at 0.1 Hz only. At voltage frequencies above 10 Hz the measured PD magnitudes were found to be nearly constant, close to the expected high theoretical value. This indicate that PD by-products strongly affected the void resistivity and thereby affect the PD activity of insulating voids. These by-products are temporary and disappear with time.

1. Introduction

To avoid temporary partial discharge (PD) events and to ensure stable void conditions during diagnostic PD-testing, IEC 60034-27 [1] and IEEE std 1434 [2] suggest a procedure for pre-conditioning of stator bar insulation. It is recommended to use at least 1-15 minutes of pre-conditioning at maximum test voltage. Recommended duration is, however, flexible, as it is stated that pre-conditioning up to 1 hour may be preferable. For example it is reported that in case of polycarbonate insulated samples stable PD conditions were reached after 1.5 hours of pre-conditioning [3].

The main purpose of this work is to experimentally investigate how PD parameters change with varying frequency AC test voltage after different durations of short-circuiting time after the one-hour pre-conditioning period. The observed phenomena are discussed with respect to a classical theory of interpretation of PD measurements.

2. Theoretical model

Equations applied in this chapter are based on the PD characteristics of new samples with no preceding PD activity. Examples on how preceding PD activity might change the void properties are shown in Chapter 2.3.

PD arcs in a void are assumed to last for a very short time, most probably a few nanoseconds [4], i.e. an applied test voltage of 50 Hz can be considered constant during the PD arc. This means that any voltage frequency dependence of PD activity must be caused by changes occurring *before* the first PD occurrence.

2.1 Frequency dependent voltage across the void

A void encapsulated in a partly conducting dielectric can be modelled by a modified abc-model, as shown in Figure 1. Here the capacitors C_a and C_b of the insulation and the void capacitance C_c are considered to have a resistor in parallel.
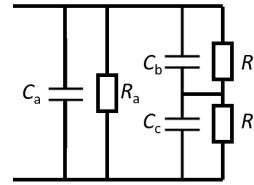
Figure 1: The modified abc-equivalent circuit for interpretation PD activity in a void enclosed in an insulation system with low conductivity.

The voltage across the void U_c is determined by the applied voltage U_a

$$U_c = \frac{Z_c}{Z_c + Z_b} \cdot U_a \qquad (1)$$

where Z_b and Z_c represent the frequency dependent impedance of the involved sections. This equation has a cut-off frequency given by the Maxwell-Wagner relation

$$f_{\text{cut-off}} \approx \frac{1}{RC} = \frac{\frac{1}{R_b} + \frac{1}{R_c}}{C_b + C_c} = \frac{R_b + R_c}{R_b R_c (C_b + C_c)} \qquad (2)$$

A PD can occur when the applied voltage exceeds the breakdown strength of the gas in the void. It is here assumed that the electric field inside the void is homogeneous and that the minimum breakdown voltage U_{s0} is given by Paschen law [5]

$$U_{s0} = 6.72\sqrt{pd} + 24.36(pd)[\text{kV}] \qquad (3)$$

where p is the pressure and d the gap distance. This expression is valid for pd values in the range from 10^{-2} to $5 \cdot 10^2$ (bar cm).

2.2 Derived partial discharge parameters

When the electric field locally is above a threshold value, an electron is needed to start PD initiation (statistic time lag) before the formation of the PD event takes place (formative time lag). The apparent charge q_{a0} is measured in the external circuit, and can be modelled by the abc-equivalent, due to the short duration of the PD pulse. In case the entire void is considered discharged

$$q_{a0} = C_b \cdot (U_s - U_r) \qquad (4)$$

where C_b is the capacitance of the insulation in series with the void, U_r is the remanent voltage after a PD has occurred and U_s the actual breakdown voltage of the void. There might be a voltage higher than that of equation (3) if no start electron is available when the voltage increased above the threshold limit. A frequency independent time delay Δt causes a larger overvoltage at high frequency due to a larger voltage change during the same period compared to low frequency

$$U_s = U_0 \cdot \sin\big(\omega(t_{PD0} + \Delta t)\big) \qquad (5)$$

where U_0 is the maximum void voltage, $t_{PD0} = \frac{1}{\omega} \cdot \mathrm{asin}\left(\frac{U_{s0}}{U_0}\right)$ is found by using $\Delta t = 0$ and Paschen voltage.

The PD pulse repetition rate n per half period is rounded down to the nearest digit and given by

$$n = \left\lfloor 2 \cdot \frac{U_0 - U_r}{U_s - U_r} \right\rfloor \qquad (6)$$

where U_0 is the maximum voltage applied across the void during a voltage cycle.

A new alternative approach, suggested here, is to define a so-called apparent repetition rate, $\hat{n}$. This is defined as the sum of all measured apparent charge magnitudes divided by the theoretical apparent charge value

$$\hat{n} = \frac{1}{q_{a0}} \sum q_a \qquad (7)$$

The total measured apparent charge is a parameter that is easy to measure, less influenced by statistical variation than the apparent charge and is directly dependent on the capacitance C_b in series with the void, the maximum void voltage U_0 and the remanent voltage U_r. The total apparent charge is expressed by combining equations (4), (6) and (7):

$$\sum q_a = \hat{n} \cdot q_{a0} = 4 \cdot g \cdot C_b \cdot (U_0 - U_r) \qquad (8)$$

where g is an area correction factor introduced as the 'relative PD-active' void area.

2.3 Influence of surface change due to PD activity

Free electrons, or start electrons, in the void can originate from different sources, such as cosmic radiation, field emission from the void walls with charges in shallow traps [6]. The PD arc reacts with the air in the void and the void surface and can produce various acids, which have been found to highly

increase the polymeric void surface conductivity [7, 8]. Such acids are known to self-decompose into neutral components, nitric acid in particular [9]. The increased surface conductivity due to PD arcs is therefore expected to decrease with time after short-circuiting. An increasing surface conductivity on epoxy surfaces caused by PD activity has been shown to change the discharge type from spark to continuous glow discharges [10]. Glow discharges produce a continuous current and can only be measured with photodetectors or pico-amperemeters. A higher surface conductivity reduces the void resistance and hence the void voltage at low frequency. This is demonstrated by the graphs presented in Figure 2, where a sketch of the normalized void voltage based on equation (1) as function of frequency are given for different void relaxation times ($\tau_c = R_c C_c$).
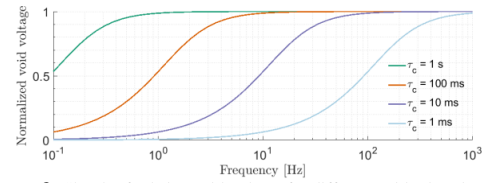
Figure 2: Sketch of relative void voltage for different void relaxation times $\tau_c = R_c C_c$, based on equation (1). The relaxation time of the insulation is chosen high; 1000 s, i.e. representing a low insulation conductivity.

3. Examined test objects

The test samples were produced using a commercially available mica tape, which was cured at 160 °C for 1 h under a pressure of 3.3 bar into 1.5 mm thickness. A 10 mm hole diameter with height of 0.5 mm was constructed with a metal spacer in the lower part during the curing. The test object types are sketched in Figure 3. The samples had dimensions 100x100x3 mm³. The upper and lower surfaces (indicated with a red line) were either kept insulating, or covered with copper tape of thickness 0.1 mm giving a reduced void height of 0.3 mm. Three similar samples were made for each type of test object.
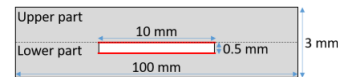
Figure 3: Sketch of test objects. The void surface (red) can be covered with 0.1 mm thick copper tape.

The samples were clamped between two brass electrodes enclosed in an epoxy cylinder to prevent spurious discharges in the air at the triple point between insulation surface, electrode and air. Additionally, a thin layer of silicone grease was applied between the electrodes and the sample to prevent unintended PD in small voids at the interface between the test object and the metal electrodes.

4. Material characterization

4.1 Methods

The complex permittivity of the insulation as function of frequency was determined by dielectric spectroscopy measurements at 200 V in the frequency range of 1 mHz to 0.1 kHz with IDAX 206 hardware and software.

One test object was modified by connecting thin copper wires to the copper tapes positioned at the surface of the voids. The wire ends were available on the outside of the test objects. The void resistance of this object before and after 1 h of $10\,\text{kV}_{\text{rms}}$ at 50 Hz was measured using a DC insulation tester at 1 kV.

4.2 Results from material characterization

The results from material characterization are shown in Table 1. The DC conductivity was calculated from the complex permittivity at low frequency.

Table 1. Equivalent circuit parameters for a void with diameter 10 mm and height 0.5 mm (0.3 mm for conducting samples) and insulation thickness of 2.5 mm based on measured complex permittivity.

Parameter	Value	Comment
C_{b} [pF]	1.1	Based on measured permittivity at 1 kHz
C_{c} [pF]	1.4	Based on void geometry h = 0.5 mm
C_{c} [pF]	2.3	Based on void geometry h = 0.3 mm
R_{b} [PΩ]	5.6	Based on measured imaginary part of complex permittivity at 0.1 mHz
R_{c} [TΩ]	>3	Measured before 1 hour at $10\,\text{kV}_{\text{rms}}$
R_{c} [TΩ]	1	Measured right after 1 hour at $10\,\text{kV}_{\text{rms}}$
R_{c} [TΩ]	>3	Measured after 20 h of object grounding
Voltage divider	0.44	$C_{\text{b}}/(C_{\text{b}}+C_{\text{c}})$, insulating samples
Voltage divider	0.32	$C_{\text{b}}/(C_{\text{b}}+C_{\text{c}})$, conducting samples

5. Partial discharge test methods

5.1 Experimental setup

The experimental setup was fully automated and controlled by a LabView program as shown in Figure 4. The hardware is based on a standard PD detection circuit [11]. The input voltage signal from the computer was amplified by a high voltage amplifier, TREK 20/20B, and filtered by a low pass filter (5 kHz) to reduce inherit amplifier noise. The test object (~20 pF) was in parallel with a coupling capacitance (100 pF).
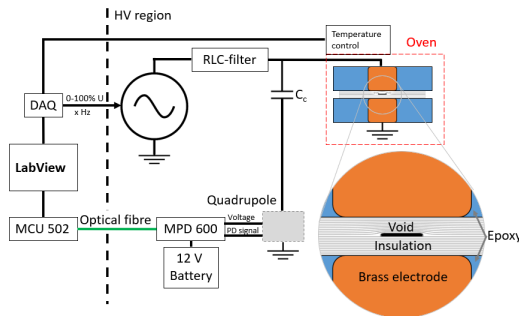

Figure 4: Setup of the PD detection circuit. Everything was controlled by a LabView program.

PD pulses was detected by using a quadrupole in series with the coupling capacitance and processed by the automated PD detection system from Omicron, MPD600 and MCU 502.

The circuit was calibrated with a calibrator that injected a charge corresponding to 100 pC across the test object.

5.2 Test procedure

The voltage application on the test samples is sketched in Figure 5. A constant voltage of $10\,\text{kV}_{\text{rms}}$ at 50 Hz was applied the first test hour with a high PD number before short-circuiting for 20 h. PD measurements during voltage frequency sweeps were performed at different time intervals during the test as indicated in the figure. The frequency sweeps consisted of 5 periods at $10\,\text{kV}_{\text{rms}}$ at each of the following frequencies: 50, 10, 1, 0.1, 1, 10 and 50 Hz. This included only 35 voltage periods, equivalent to less than a second of 50 Hz voltage application. It was therefore assumed that the conditions within the void was unaffected by the short period of PD measurements during the frequency sweep. This was controlled by the first and last five 50 Hz periods in the frequency sweep.
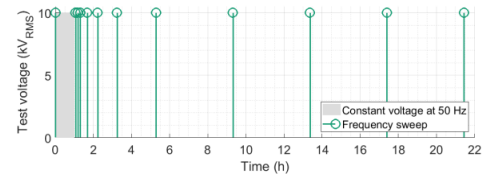
Figure 5: Sketch showing the voltage application versus time. The test object was short-circuited between the frequency sweeps, except between the first and second frequency sweep.

One sample were tested with the frequency sweep order changed, starting at low frequency, to investigate if the test procedure influenced the results.

6. Results from measurements of time development of PD parameters

The PD frequency sweep gave the same results regardless of the frequency sequence (50 Hz to 0.1 Hz or 0.1 Hz to 50 Hz) or the position in the frequency sweep (first vs last). Hence, the frequency sweep does not contribute to any measured frequency dependence on the PD characteristics

The measured PDs occurred at different phase locations and with different magnitude. The distribution of PD magnitude at three time instances for the two object types are given as a typical example in Figure 6. The PRPDAs are not shown, but they are symmetric and shifted to the voltage rise, which is typical for void discharges.
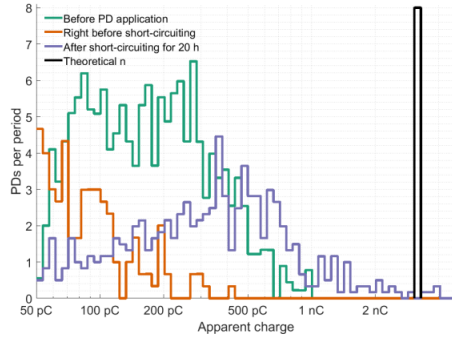
a) Void with insulating surfaces.
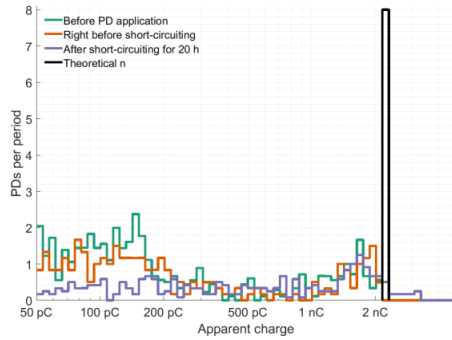
a) Void with copper tape

Figure 6: Histogram of number of PDs per period for both sample types at 50 Hz based on the average of three samples. It is a similar distribution at all tested frequencies, but with the maximal magnitude slightly different. The theoretical value of 8 per period is based on twice the value obtained in equation (6) for one half period.

The apparent PD repetition rate $\hat{n}$ versus time for different frequency and object type is given in Figure 7. It is a large spread in apparent charge magnitude with many small values and the resulting repetition rate n is very high and thereby useless.

Figure 7: Apparent PD repetition rate $\hat{n} = \sum q_a/q_{a0}$ for three parallels (giving the error bars) versus test time. A constant voltage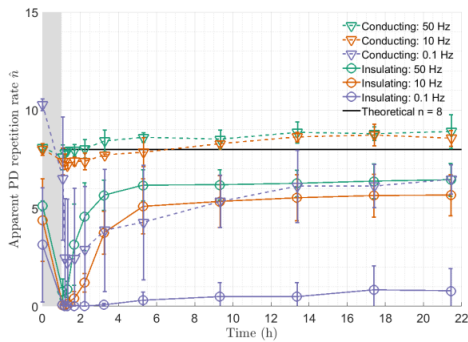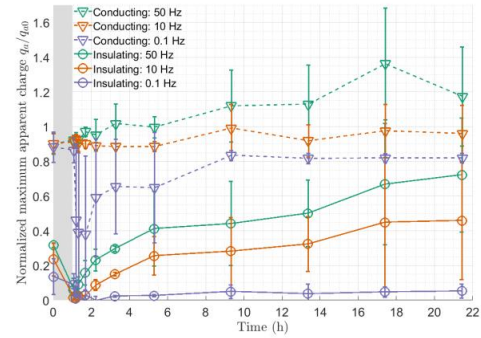 was applied (grey region), with high PDs, for the first test hour. The theoretical value of 8 per period is based on twice the value obtained in equation (6) for one half period.

The normalized maximum detected apparent charge during five voltage periods as function of time for different frequencies and object type is presented in Figure 8. The theoretical value was used as normalization factor, given by equation (4), which is 3.1 nC for insulating objects and 2.2 nC for conductive objects. This difference is due to a reduced void height caused by the thickness of the copper tape.

Figure 8: Average normalized maximum apparent charge for three parallels (giving the error bars) versus test time. A constant voltage was applied (grey region), with high PDs, for the first test hour.

The calculated void voltage based on equation (8) is presented in Figure 9 for insulating objects and in Figure 10 for the objects with copper tape. It is a significant influence from the pre-conditioning.
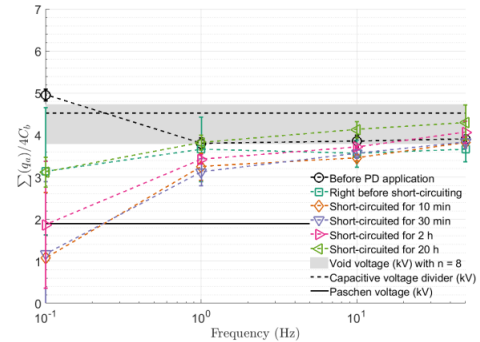
Figure 9: Void voltage as function of frequency at different time instants for samples with copper tape. The y-axis is equal to $g(U_0 - U_r)$ as defined in equation (8). The void voltage with n = 8 per period is based on the voltage region in equation (6) that gives n = 8.
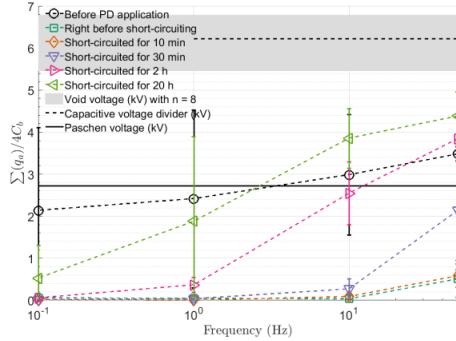
Figure 10: Void voltage as function of frequency at different time instants for samples with insulating surfaces. The y-axis is equal to $g(U_0 - U_r)$ as defined in equation (8). The void voltage with n = 8 per period is based on the voltage region in equation (6) that gives n = 8.

7. Discussion

The cutoff frequency based on material parameters for new samples, given in Table 1, and equation (2) is less than 1 mHz. This means that no frequency dependence is expected. The one-hour pre-conditioning lowered the void resistivity, increasing the cutoff frequency to 2 Hz. The pre-conditioning change the void resistivity and is thereby expected to change the voltage frequency response of the void.

Figure 6 shows great difference in distribution of PD magnitude of both object types vs expected theoretical value. A minor spread was expected according to equation (5) with a time lag. The large observed spread cannot be explained by a time lag and it makes no meaning to use the PD repetition rate n to describe the PD activity. The suggested apparent repetition rate $\hat{n}$ is therefore an adequate estimator for how many times the total void area discharges during a voltage period. The small PD magnitudes can be related to edge effects at the edge of the copper tape. Another observation is that the voids with insulating surfaces in a) are more influenced by the constant 50 Hz voltage application than the voids with copper tape in b).

The calculated apparent repetition rate $\hat{n}$ based on the total apparent charge is presented in Figure 7 for the two object types at different voltage frequencies versus time. The theoretical repetition rate n were expected to be 8 in both objects despite the geometrical difference. The apparent repetition rate for the voids with copper tape was close to the theoretical repetition rate, which indicates that the complete void was discharged as expected. However, the steady-state repetition rate at 0.1 Hz is only 6, probable related to a lower void voltage. The apparent repetition rate in case of voids with insulating surfaces was lower than for the samples with copper tape. This can be caused either by a lower void voltage, or a smaller relative 'PD-active area'. The sum of apparent charge divided by four divided by the series capacitance C_b, equal to $g(U_0 - U_r)$ by equation (8), for the objects with copper tape is presented in Figure 9 and with insulating surface in Figure 10. Void voltages below Paschen voltage cannot give PDs and only a fraction of the total area can be 'PD-active'. By assuming a pure capacitive divider, the area correction factor g for the insulating object is: 0.70, 0.62, 0.30

and 0.08 for 50, 10, 1 and 0.1 Hz respectively. This corresponds to a reduced 'PD-active' void diameter of 8.4, 7.9, 5.5 and 2.9 mm. The reduction in 'PD-active' area provides still a too high apparent charge if the complete reduced area discharges during a PD, compared to the measured maximum apparent charge at these frequencies shown in Figure 8. This strongly indicates that the voids with insulating surfaces have a smaller frequency dependent PD-active discharge area.

The pre-conditioning lowered the void resistance, as also measured by direct methods reported in Table 1. The resistance reduction was only temporary as it restored to original state after a long short-circuited period. The reduced void voltage enables less discharges to be produced, as is shown in Figure 7 and a smaller maximum apparent charge as is shown in Figure 8. This effect was largest for the voids with insulating surfaces, which indicates that the properties of the insulating surfaces were changed by the PD activity during constant 50 Hz voltage application. It was a relatively large frequency dependence, in which the void was almost short-circuited at low frequency. The frequency dependent PD activity at different time instants in Figure 10 for the voids with insulating surfaces can be described by a varying relaxation time. By comparing it with Figure 2 it is seen that the overall trend was that the relaxation time started high, reduced to a low value after the pre-conditioning and then gradually recover with time. This indicates, by a lower PD activity, that the void resistivity decreased with pre-conditioning and increased when grounded. One possible explanation is the presence of PD by-products such as acids, as seen in [7, 8], and following gradual self-decomposition of the acids when the test object was short-circuited. The effect of pre-conditioning was only important for voids with insulating surfaces as there were a large time and frequency dependence in Figure 10 and a low frequency dependence in Figure 9.

Hudon et al. [10] studied PD activity during a long constant AC voltage application with PD and described a transition from spark to glow discharges after a long time. This was correlated to an increased surface conductivity caused by PD activity. The increased surface conductivity in voids, in contrast to [10] with no void walls, short-circuit the void and it is possible that glow discharges are not present in voids. However, a transition to glow discharges *can* explain a reduced void discharging area and can be interesting to investigate in further works. This study had not the equipment to follow this track any further.

8. Conclusions

- The measured repetition rate was much higher than the theoretical value n. A more convenient parameter was the estimator apparent repetition rate, $\hat{n}$, which was introduced here. It sums up all the apparent charge during a voltage cycle, normalized to the theoretical apparent charge, and was close to the theoretical value for the repetition rate.
- The pre-conditioning period with PD activity changed the void such that the PDs extinguished at low frequency. This can be explained by a reduced void resistance due to by-products from PD activity.
- The void change due to pre-conditioning was only temporary as the PD activity slowly restored to the original state when short-circuited. This can be explained by gradual

neutralization of the by-products from PD process that initially reduced the void voltage.

Acknowledgement

References

[1] *IEC TS 60034-27:2006, Off-line partial discharge measurements on the stator winding insulation of rotating electrical machines*, 2006.

[2] *IEEE Std 1434-2014 (Revision of IEEE Std 1434-2000), IEEE Guide for the Measurement of Partial Discharges in AC Electric Machinery*, 2014.

[3] C. Forssen and H. Edin, "Partial discharges in a cavity at variable applied frequency part 1: measurements," *IEEE Transactions on Dielectrics and Electrical Insulation,* vol. 15, no. 6, pp. 1601-1609, 2008.

[4] R. Morrow and J. J. Lowke, "Streamer propagation in air," *Journal of Physics D: Applied Physics,* vol. 30, no. 4, p. 614, 1997.

[5] E. Kuffel and W. S. Zaengl, *High-voltage engineering: fundamentals*. Pergamon Press, 1984.

[6] L. Niemeyer, "A Generalized Approach to Partial Discharge Modeling," *IEEE Transactions on Dielectrics and Electrical Insulation,* Article vol. 2, no. 4, pp. 510-528, 1995.

[7] C. Hudon, R. Bartnikas, and M. R. Wertheimer, "Surface conductivity of epoxy specimens subjected to partial discharges," in *Conference Record of IEEE International Symposium on Electrical Insulation*, pp. 153-155, 1990.

[8] C. Hudon, R. Bartnikas, and M. R. Wertheimer, "Analysis of degradation products on epoxy surfaces subjected to pulse and glow type discharges," in *1991 Annual Report. Conference on Electrical Insulation and Dielectric Phenomena*, 1991, pp. 237-243.

[9] G. D. Robertson, D. M. Mason, and W. H. Corcoran, "The Kinetics of the Thermal Decomposition of Nitric Acid in the Liquid Phase," *The Journal of Physical Chemistry,* vol. 59, no. 8, pp. 683-690, 1955/08/01 1955.

[10] C. Hudon, R. Bartnikas, and M. R. Wertheimer, "Spark-to-glow Discharge Transition due to Increased Surface Conductivity on Epoxy Resin Specimens," *IEEE Transactions on Electrical Insulation,* Article vol. 28, no. 1, pp. 1-8, 1993.

[11] *IEC 60270:2000, High-voltage test techniques - Partial discharge measurements* 2000.

Paper IV

T. G. Aakre, E. Ildstad, and S. Hvidsten. Partial discharge inception voltage of voids enclosed in epoxy/mica versus voltage frequency and temperature. *IEEE Transactions on Dielectrics and Electrical Insulation*, 27(1):190–197, 2020

Partial Discharge Inception Voltage of Voids Enclosed in Epoxy/Mica versus Voltage Frequency and Temperature

Torstein Grav Aakre and **Erling Ildstad**
Norwegian University of Technology and Science (NTNU)
Department of Electric Power Engineering
NO-7491 Trondheim, Norway

Sverre Hvidsten
SINTEF Energy Research
Department of Electric Power Technology
NO-7465 Trondheim, Norway

ABSTRACT

Detection of partial discharges (PDs) is widely used as a condition assessment tool for high voltage equipment. Application of low frequency test voltage is often preferred in the case of test objects with a large capacitance. The question addressed here is how results from PD-measurements performed at low frequencies correspond to that occurring at 50 Hz power frequency. Different theoretical models for void voltage were examined and compared to experiments performed on laboratory samples of mica/epoxy, including embedded cylindrical voids. All test objects were preconditioned at 10 kV and 50 Hz for 5 min before partial discharge inception voltage (PDIV) testing by stepwise increasing the test voltage from 0 to 10 kV. The PDIV test was first completed at 300 Hz before being repeated at decreasing frequencies down to 0.1 Hz. The temperature was varied in the range of 20° to 155°C. The results at high frequencies showed that a pure capacitive model fits well to the measurements. Measured dielectric response in mica/epoxy explained the decreasing PDIV at low frequencies and high temperatures. A high PDIV was measured at a combination of low temperatures and low frequencies. This was correlated with a reduced void resistance of the electrically stressed void sidewalls caused by the PD activity during the preconditioning period. This indicates that the effect of PD by-products decays faster at higher temperatures. Values of PDIV are, therefore, expected to be dependent on both temperature and frequency.

Index Terms — **partial discharges, rotating machine insulation, cavities, variable frequency**

1 INTRODUCTION

ELECTRICAL condition assessment of high voltage equipment is today performed at different voltage frequencies. It is advantageous to test high voltage equipment with a large capacitance, e.g. generators and cables, by energising them at a very low frequency (VLF) voltage, because these voltage sources are much smaller and easier to apply than the required transformer or resonant source at power frequency. Power frequency tests have been in focus in condition assessment standards [1, 2]. VLF tests can be used, but at a higher voltage [3], and VLF and power frequency tests can give significantly different results.

Several studies have tried to explain partial discharges (PDs) in small voids as a function of frequency. The simplest approach

was by using an RC circuit to model an insulation system with a void [4]. They varied the time constants of the insulation and the void. A greater cavity time constant than the material time constant resulted in a higher PD repetition rate at low frequencies. The PD repetition rate decreased when the time constant of the void was smaller than that of the insulation. Other works have compared finite element method (FEM) modelling of various void dimensions of different level of detail to experimental results [5-10], with parameters such as apparent charge and repetition rate vs voltage frequency.

The purpose of this study is to establish an equivalent circuit that can be used to describe the frequency- and temperature-dependent void voltage. This was studied experimentally in a laboratory setup using mica/epoxy samples with an enclosed cylindrical void. This work will discuss the experimental validity of different theoretical models and the mechanisms responsible for frequency-dependent partial discharge inception voltage (PDIV) behaviour at different temperatures.

2 VOID VOLTAGE MODELS

The voltage across a void encapsulated in a dielectric can be modelled by representing the system by an equivalent circuit. To establish such circuits, the void is denoted with subscript c, the series insulation subscript b, and the surrounding insulation parallel subscript a. Edge effects are not included, and the electric field is assumed to be homogeneous in all parts of the insulation.

The first model considered here (Model 1, Figure 1a) is the capacitive so-called abc-circuit equivalent [11], referring to the circuit components as pure capacitances. In the case of modelling PD inception at DC or low voltage frequency, the abc-model is expanded by introducing resistance (Model 2, Figure 1b) and dielectric response (Model 3, Figure 1c) in the insulation. The void resistance R_c consists of both resistance in air and resistance at the surface between sections a and c.

a) Model 1: Capacitive

b) Model 2: Capacitive and resistive

c) Model 3: Capacitive, resistive and dielectric response
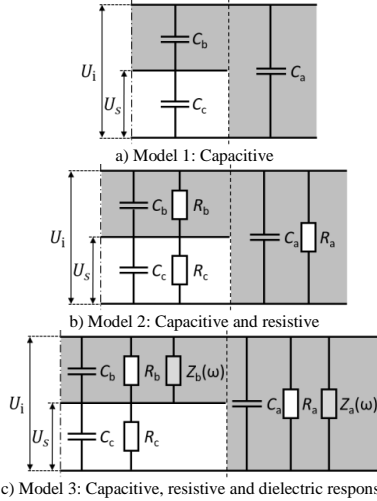
Figure 1. Equivalent circuits of an insulation system with a cylindrical void. The insulation is shaded gray, whereas the void is white.

The resulting relations between the applied voltage U_i and the voltage occurring across the void U_s are presented in Equations (1), (2), and (3), assuming a cylindrical void. The definitions of the symbols used in these equations are given in Table 1. The circuit elements are expressed by material parameters to make the equations independent of void area.

Table 1. Definition of parameters used in the models.

Parameter	Definition
U_s	Breakdown voltage in void, based on Paschen curve
U_i	Measured Partial Discharge Inception Voltage for given U_s
d_b	Insulation thickness
d_c	Void gap distance
ω	Angular frequency; $\omega = 2\pi f$, where f is frequency
ε_0	Vacuum permittivity
$\varepsilon_{r,c}$	Relative permittivity of air
$\varepsilon_{r,b}$	Relative permittivity of insulation
ε_b^*	Complex permittivity of the insulation
σ_b	Conductivity of the insulation
σ_c	Conductivity of the air in the void

PDIV U_i for given void voltage U_s with Model 1:

$$U_i = \left(1 + \frac{d_b}{d_c} \cdot \frac{\varepsilon_{r,c}}{\varepsilon_{r,b}}\right) \cdot U_s. \qquad (1)$$

PDIV U_i for given void voltage U_s with Model 2:

$$U_i = \left(1 + \frac{d_b}{d_c} \frac{\sigma_c + j\omega\varepsilon_0\varepsilon_{r,c}}{\sigma_b + j\omega\varepsilon_0\varepsilon_{r,b}}\right) \cdot U_s. \qquad (2)$$

PDIV U_i for given void voltage U_s with Model 3:

$$U_i = \left(1 + \frac{d_b}{d_c} \frac{\sigma_c + j\omega\varepsilon_0\varepsilon_{r,c}}{\sigma_b - \frac{\mathrm{Im}\{\varepsilon_b^*\}}{\omega} + j\omega\mathrm{Re}\{\varepsilon_b^*\}}\right) \cdot U_s. \qquad (3)$$

Partial discharge modelling assumes that a discharge occurs when the voltage across the void exceeds the withstand strength of the void. In the case of a homogeneous electric field in the void, the withstand strength of the void given by the Paschen law can be approximated to [11]:

$$U_s = 6.72\sqrt{pd} + 24.36(pd)[\mathrm{kV}], \qquad (4)$$

when the pressure times distance, pd, is in the range 10^{-2} to $5 \cdot 10^2$ (bar cm).

In the case of dielectric response, the frequency dependence of the permittivity of the solids, ε^*, needs to be included. Here, the empirical Cole-Cole model [12] is used,

$$\varepsilon^* = \varepsilon(\infty) + \frac{\varepsilon(DC) - \varepsilon(\infty)}{1 + (j\omega\tau)^{1-\alpha}}, \qquad (5)$$

where $\varepsilon(\infty)$ is the permittivity at very high frequencies, $\varepsilon(DC)$ the permittivity at very low frequencies, ω the angular frequency, and τ the temperature-dependent relaxation time. The shape parameter α describes the broadness of the relaxation peak and has a value between 0 and 1. Equation (5) is temperature-dependent according to an Arrhenius relation [13] such that $\tau(T) = \tau_0 \cdot \exp\frac{E_a}{k_BT}$, where E_a is the activation energy, k_B the Boltzmann constant, and T the temperature in Kelvin.

The capacitive Model 1 is valid at high frequencies when the resistive contribution is low. Model 2 applies at low frequencies when the resistive contribution is higher or comparable to the capacitive contribution, as can be seen in Equation (2) for Model 2. The cut-off frequency f_c between high and low frequencies is described by the Maxwell-Wagner effect for interfacial polarisation between two materials:

$$f_c = \frac{d_c\sigma_b + d_b\sigma_c}{d_c\varepsilon_0\varepsilon_{r,b} + d_b\varepsilon_0\varepsilon_{r,c}}. \qquad (6)$$

The inclusion of dielectric response in Model 3 complicates the calculation of the cut-off frequency f_c. As ε_b^* is frequency-dependent, a numerical approach is needed. This can be done by creating a frequency-dependent

estimator $\hat{f}_c$ for f_c in Equation (6) and comparing it to the frequency at the different values for ε_b^*. The cut-off frequency f_c is then defined when $\hat{f}_c = f$.

The void resistance is usually neglected, as the air conductivity is low. The conductivity of air strongly depends on atmospheric conditions and is in the range 10^{-16} to 10^{-13} S/m [14]. The value is drastically reduced if the gas ions are neutralised. This conductivity range corresponds to cut-off frequencies in the range $5 \cdot 10^{-6}$ to $5 \cdot 10^{-3}$ Hz.

PDs produce chemical by-products when in contact with the surrounding gas or dielectric surface. Hudon *et al* [15] determined that PDs react with air and the epoxy surface and create oxidic, formic, glycolic, glyoxylic, and nitric acids, which result in a significantly increased surface conductivity. Test objects are often preconditioned, and during this period such components are likely to be produced, thereby decreasing the void resistivity. This can partly or completely short-circuit voids, significantly increasing the cut-off frequency, while the void models cannot neglect the void resistivity.

The effect of such preconditioning disappears with time [16]. Generally, at elevated temperatures, the PD by-products diffuse or are neutralised faster than they are produced. The temperature dependence is especially large for the self-decomposition of nitric acid [17], which reduces the acidity at higher temperatures and thereby the surface conductivity. Consequently, the decomposition of nitric acid is almost instantaneous at 90°C. Possible effects of PD by-products caused by the preconditioning are, therefore, expected to be active at low temperatures only.

3 EXPERIMENTAL METHODS

3.1 TEST OBJECTS

Square samples with dimensions 100x100x3 mm^3 were produced from a resin-rich mica tape commonly used as the main insulation of bars and coils of motor and hydro and turbo generators with 45% mica, 43% epoxy resin and 12% glass fibre, by weight percent. The samples were cured at 160°C for one hour before being rapidly cooled to 20°C for 5 minutes. Three different test objects with embedded voids were used, as shown in Figure 2. Test object 1 consisted of two layers pressed together, where the void was created in the lower layer by using a thin metal disk during the casting process. This created voids with a smooth surface. The void diameter D was in the range of 3-20 mm and the void gap distance d_c in the range of 0.1-1 mm. Test object 2 consisted of three layers with a drilled hole in the middle layer with a void diameter of 80 mm, much larger than the electrode, giving no electrically stressed sidewalls and a void gap distance of 1 mm. Test object 3 was similar to Test object 2, but with a void diameter of 10 mm and a void gap distance of 0.8 mm. The top and bottom of the cylindrical void in Test object 3 were covered with copper tape, which was connected to the outside of the sample with a thin copper wire. The test
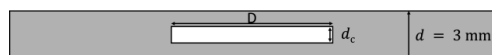

Figure 2. Schematic drawing of the cross section of the test objects.

objects were clamped between two electrodes with a diameter of 30 mm with the side walls embedded in epoxy and covered with a thin silicon grease layer to prevent any unintended air discharges.

3.2 MATERIAL CHARACTERISTICS

The insulation material was characterised by dielectric spectroscopy in both time and frequency domain. This can measure the frequency-dependent complex permittivity and DC conductivity, which are important parameters to the presented void voltage models.

The time domain dielectric response tests on the mica/epoxy insulation were performed using 1-mm-thick objects without voids. Aluminium electrodes with a diameter of 40 mm with guard were evaporated to the surface. These samples fitted into an automated measurement setup, as described in [18]. A constant DC voltage in the range of 1 to 8 kV was used. The temperature was set to 40°, 60° and 90°C, in increasing order. The DC voltage was applied for 2 h to measure the polarisation current before the object was grounded for 20 h during depolarisation current measurements.

Dielectric response in the frequency domain was performed on 1 mm thick mica/epoxy samples without voids, by standard methods with IDAX 206 hardware and software. This was done at frequencies in the range of 10^3 to 10^{-4} Hz at 200 V_{peak}. The temperatures were in the range of 20° to 155°C and larger than for the time domain measurements due to limitations of the equipment.

The void resistivity was measured before and after preconditioning on Test object 3 by a DC insulation tester by applying 1 kV DC voltage. This was done to establish whether the preconditioning can decrease the void resistivity or not by a direct resistivity measurement method.

3.3 PD MEASUREMENTS

The PDIV is here defined, in accordance with the definition in IEC 60270 [19], as the voltage level that first produces PDs above a threshold value of 100 pC. Each PDIV data point in this article represents the average result of PD measurements for three similar samples.

The standard PD test setup is shown in Figure 3, as described in e.g. IEC 60034-27 [1]. The Test object (with a capacitance of ~20 pF) was in parallel with a coupling capacitance (100 pF). The measure impedance was in series with the coupling capacitance, Omicron CPL 542, and the data processing unit MPD 600. The high voltage was set by a DAQ and amplified by a TREK 20/20B high voltage amplifier in series with a low-pass filter, with a cut-off frequency at 5 kHz.

The voltage source, heat control, and data measurements were fully automated in LabView. The test procedure was based on the standard method in IEC 60034-27 and IEEE 1434 [1, 2]. The standardised procedure at 50 Hz was expanded to a frequency and temperature sweep, to keep the void condition time variation at a minimum during the test.
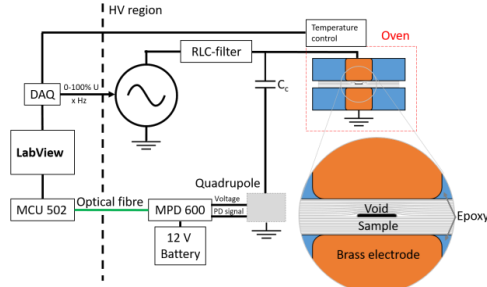
Figure 3. Setup of the PD detection circuit. The setup was controlled by a LabView program.

The procedure of voltage application is shown in Figure 4. It started with a conditioning period of 5 minutes at a maximum test voltage of 10 kV$_{RMS}$ at 50 Hz. Then, the sample was grounded before the voltage was increased in 10 equal steps to maximum test voltage and then decrease in 10 steps back to zero voltage, starting at 300 Hz. The duration of each voltage step was the longest time of 10 s and 10 voltage periods. A minimum of 10 periods was chosen in order to be able to sweep many samples at different frequencies in a limited time. The procedure of voltage application was repeated for several frequencies in decreasing order down to 0.1 Hz. The 50 Hz PDIV test was repeated after the 0.1 Hz PDIV test was finished. The conditioning period at 50 Hz between different frequencies was reduced to 5 s to not influence the void condition but, rather, act as a reference if PDs at 50 Hz changed during the frequency sweep. Both the maximum and total apparent charge during this 5 s period were recorded and used as they can be related to the void voltage [16].
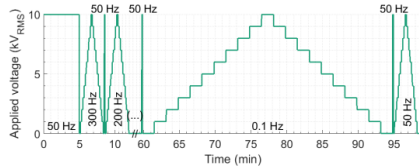
Figure 4. Sketch of the frequency sweep with reducing frequencies.

The temperature was increased in the range of 20° to 155°C after the frequency sweep was finished. A waiting time of 1 hour was shown to be sufficient to reach stable thermal conditions before a new frequency sweep started.

Four samples were tested a second time to check if the frequency and temperature sweep had introduced permanent changes to the samples that influenced the PDIV.

The preconditioning was expected to increase the void conductivity according to Model 2. An increased void conductivity results in a high PDIV. One sample of Test object 1 with a diameter 10 mm and void gap distance 0.5 mm was, therefore, PDIV tested at 0.1 Hz without any preconditioning. This test should indicate whether the preconditioning period increased the value of PDIV at 0.1 Hz.

4 RESULTS AND DISCUSSION

4.1 MATERIAL CHARACTERISATION

The mica/epoxy bulk conductivity was found to be independent of the electric field in the measured range of 1 to 8 kV/mm. It followed an Arrhenius relation with conductivity at 20°C of $\sigma_{20°C} = 5 \cdot 10^{-15}$ S/m and activation energy $E_a = 0.44$ eV with $R^2 = 0.995$.

The void resistance before preconditioning at 20°C was above the instrument limit of 3 TΩ. The void resistance had decreased after the preconditioning to 1 TΩ (corresponding to a void conductivity of $\sigma_c \approx 10^{-11}$ S/m), which means that PD-activity was reducing the void resistance.

The measured values of the real and imaginary parts of the complex permittivity for the tested insulation are given in Figure 5 as data points. The extrapolated conductivity based on the measured values is given as dotted, straight lines. The solid lines correspond to one Cole-Cole mechanism, including the DC conductivity, as described in the temperature-dependent version of Equation (5). The Cole-Cole parameters were curve-fitted to be $\varepsilon(\infty) = 4.42$, $\varepsilon(DC) = 940$, $\tau_0 = 7.4 \cdot 10^{-9}s$, $E_{a,\tau} = 1.00$ and $\alpha = 0.42$. At frequencies above 0.1 Hz, the contribution to dielectric loss from DC conductivity is more than two orders of magnitudes lower than the other losses and can be omitted.
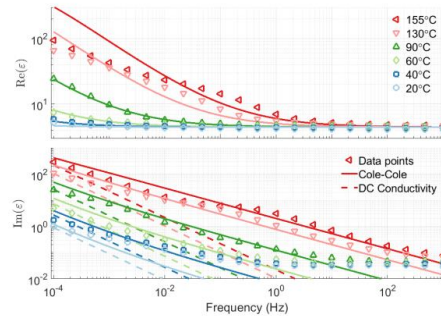

Figure 5. Complex permittivity of the epoxy/mica insulation as a function of frequency for increasing temperatures fitted to a temperature dependent Cole-Cole mechanism and the curve fitted DC-conductivity based on measured dielectric response in the time domain.

4.2 VALIDITY REGIONS OF THE MODELS

A typical insulation system in this study has a void gap distance of 0.5 mm and a mica/epoxy thickness of 2.5 mm. Measured material parameters, together with the assumption of a non-conducting void, have been inserted into the different models. The resulting regions in the temperature-frequency domain, where the different models work, are given in Figure 6. The estimated PDIV cut-off frequencies based on Equation (6) are also included in the figure. All models are equal in the red region (Models 1, 2, 3) where the DC conductivity or dielectric response do not contribute. The conductivity is dominant in the blue region, and Models 2 and 3 are equal. Similarly, in the green region, the dielectric response is dominant, and Model 3 is the only model describing this. The borders between the different regions are

defined as the frequency at which the different models differ more than 5% from each other, and the valid model is assumed to be the most advanced. The limit of 5% was set as a low limit, considering the uncertainties when measuring PDIV in the laboratory and voltage step size. The polarisation losses and insulation conductivity can be neglected above their respective cut-off frequencies, f_c, which is practically always when testing above 0.1 Hz and below 110°C.
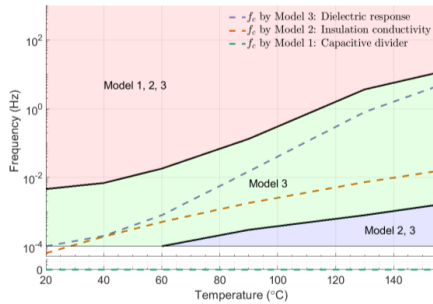
Figure 6. 'Model phase diagram' based on measured values for insulation conductivity and dielectric response for the three different models. The conductivity in the void is assumed to be zero. The estimated Maxwell-Wagener frequency, f_c, is indicated by coloured dotted lines.

4.3 INFLUENCE ON PDIV FROM PRECONDITIONING

A PDIV test at 0.1 Hz without preconditioning on Test object 1 with a diameter 10 mm and a height 0.5 mm demonstrated a PDIV of 5 kV, estimating a low void conductivity. This indicates that the high PDIV at low frequencies after preconditioning - as seen for example in Figure 8 - is a result of the preconditioning period.

A second PDIV test succeeding the first complete frequency and temperature sweep did not produce any significant changes to the PDIV curves. Possible permanent surface changes due to the temperature and electric stress during the test do not seem to affect the PDIV. This means that any increase in conductivity was caused by temporary effects, such as PD by-products that disappeared when the temperature was increased.

The preconditioning was found to influence the void conditions. The total apparent charge during the 5 s conditioning between the different frequencies generally increased with time. This indicated that the preconditioning effect faded with time, similarly to what was seen in [16]. This means that the effect of preconditioning was weaker at lower frequencies than at higher frequencies due to the frequency test order. However, as is seen in the following figures and discussion, the effect remains strong enough to increase the PDIV at low frequencies and thereby predict a reasonable void conductivity. The measured PDIV can be lower than expected if the preconditioning effect fades, resulting in an underestimated void conductivity.

4.4 THE EFFECT OF PRECONDITIONED ELECTRICALLY STRESSED SIDE WALLS

The measured PDIV as a function of frequency for selected sample geometries is given in Figures 7-10. The solid lines represent curve fitting by varying the void conductivity to the dielectric response-based Model 3 in Equation (3). Model 2 could have been used to give equally good estimates to explain trends, but with a minor deviation at high temperatures where the dielectric response is dominating. It was, therefore, considered easier to use Model 3 to fit all the data. Figure 8 describes Test object 1 with a large void diameter (20 mm) and gap distance (0.5 mm) acting as an example for large voids. PDIVs as a function of frequency are all similar for Test object 1 with diameters larger than 10 mm or the gap distance is larger than 0.5 mm.

Test object 2 without electrically stressed sidewalls in Figure 7b has, as expected, zero void conductivity compared to the case in Figure 6. Voids without electrically stressed walls appear as non-conducting. The difference in PDIV at low temperature between Test object 2 in Figure 7 and the other three figures with Test object 1 illustrates that the electrically stressed sidewalls in Test object 1 are important and increases the void conductivity. PD by-products must then deposit at the void sidewall and thereby increase the void conductivity.

The void with a small gap distance (0.1 mm) in Figure 9 shows a smaller frequency dependence than the voids with larger gap distances. The measured low PDIV at low temperatures in a larger frequency range indicates that the void conductivity is lower than for larger gap distances. This indicates that narrow void gaps are less influenced by the PD by-products from the preconditioning than the larger gaps are.

In the case of a small void diameter (3 mm) in Figure 10, measured values of PDIV did not fit the suggested models by being less frequency-dependent than expected. This indicates that the fundamental model assumptions did not hold for void diameters lower than 5 mm. One possible explanation is that the effect of the preconditioning had become weakened and influenced the measured PDIV. The stronger influence at higher temperatures can be due to different time dynamics of the PD by-products due to void geometry.
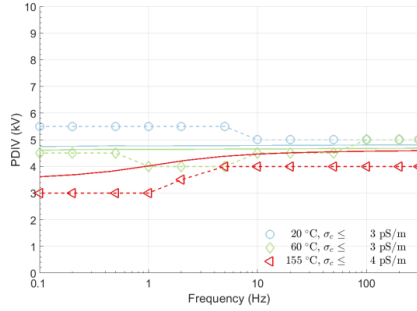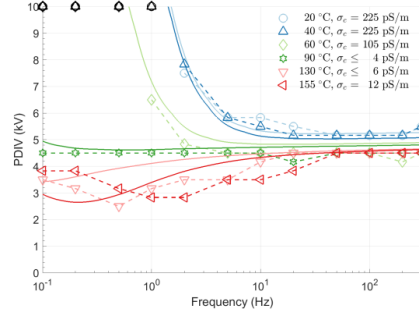
a) PDIV with fitted curves based on Model 3. Markers are measured values, whereas solid lines in the same color represent the theoretical values. $\sigma_c \leq 3$ pS/m, which were the limit by using minimum 0.1 Hz.
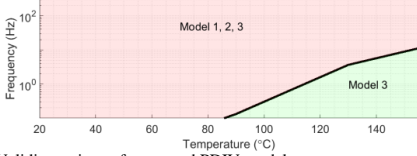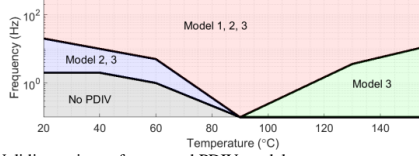

b) Validity regions of presented PDIV models.

Figure 7. PDIV vs frequency for different temperatures for Test object 2, without void walls, with void gap distance 1 mm.

a) PDIV with fitted curves based on Model 3. Markers are measured values, whereas solid lines in the same color represent the theoretical values. Black markers indicate PDIV values higher than 10 kV.

b) Validity regions of presented PDIV models.

Figure 9. PDIV vs frequency for different temperatures for Test object 1, with void diameter 10 mm and gap distance 0.1 mm.

a) PDIV with fitted curves based on Model 3. Markers are measured values, whereas solid lines in the same color represent the theoretical values. Black markers indicate PDIV values higher than 10 kV.

b) Validity regions of presented PDIV models.

Figure 8. PDIV vs frequency for different temperatures for Test object 1, with void diameter 20 mm and gap distance 0.5 mm.
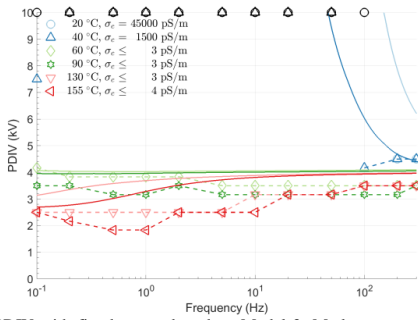

a) PDIV with fitted curves based on Model 3. Markers are measured values, whereas solid lines in the same color represent the theoretical values. Black markers indicate PDIV values higher than 10 kV.
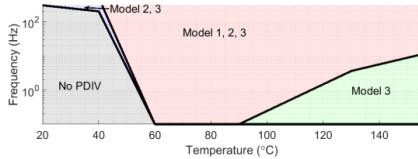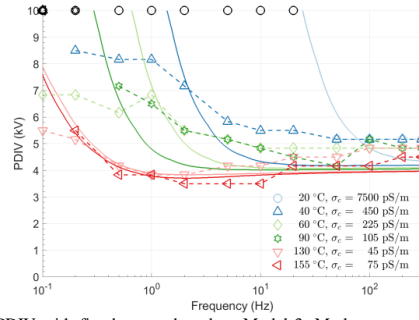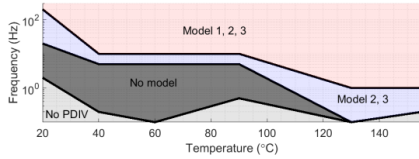

b) Validity regions of presented PDIV models.

Figure 10. PDIV vs frequency for different temperatures for Test object 1, with void diameter 3 mm and gap distance 0.5 mm.

4.5 TEMPERATURE DEPENDENCE OF CALCULATED VOID CONDUCTIVITY

The calculated void conductivities from Model 3 for selected void geometries as a function of temperature are shown in Figure 11. The Arrhenius relation of the void conductivity shows decreasing values with temperature. This is the opposite of what is usually measured for insulation materials where the conductivity increases with temperature. PD by-products deposited at the surface and contributing to the void conductive are, therefore, most likely responsible for this temperature dependence. The involved conductivity processes are not following simple theory, but rather a complex process in which the conductive species are created and assumed to disappear with time and faster at higher temperatures. This can explain the high conductivity at low temperatures and why the conductivity is low at high temperatures, but it needs to be investigated in detail in other studies.

The objects with the smallest void diameters and void gap distances had a different void conductivity temperature dependence than the objects with larger voids. The conductivity remained high, which might indicate that by-products in smaller voids do not relax as fast as in larger voids. This might indicate that the void volume is important for by-product relaxation.
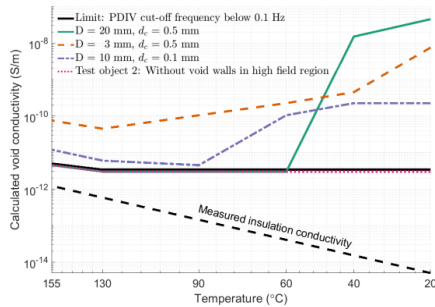

Figure 11. Calculated void conductivity from Model 3 for varying void geometry.

4.6 SIMPLIFIED VOID VOLTAGE MODEL

The mica/epoxy and void air bulk conductivity were demonstrated to be low, resulting in a cut-off frequency below 0.01 Hz. This means that the capacitive Model 1 is sufficient to describe the frequency dependence of PDIV. The capacitive Model 1 must be modified to include the dielectric response at temperatures above 110°C and frequencies above 0.1 Hz. Other limits apply if changing the minimum frequency, according to Figure 6.

The void conductivity can be high and influencing the PDIV when dealing with preconditioned electrically stressed voids at temperatures below 60°C, as was seen by an increased calculated void conductivity in Figure 11. This means that the void conductivity must be included in the model. A simplified version of Model 2 is obtained by expanding Model 1 with the void resistance as presented in

Figure 12. The material conductivity was demonstrated to be low and thereby not influencing the PDIV and not included in the model. The simplified Model 2 is valid below 110°C and frequencies above 0.1 Hz, where the permittivity is low and not influencing the PDIV. The model does not fit for voids smaller than 5 mm in diameter. Model 1 can be used if no preconditioning has occurred. The dielectric response must, however, be included if applying frequencies or temperatures outside the limiting values described by Figure 6.
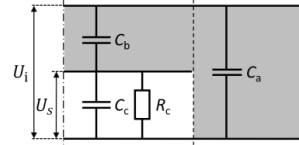

Figure 12. Simplified Model 2, requiring temperatures below 110°C, voltage frequencies above 0.1 Hz and preconditioned voids with diameter larger than 5 mm. The void (wall) resistance R_c can be omitted when no preconditioning has been done or there are no electrically stressed side void walls.

5 CONCLUSIONS

- The frequency-dependent mica/epoxy permittivity was shown to follow the Cole-Cole model. The increased dielectric response at low frequencies at high temperatures decreased the PDIV.
- The calculated void conductivity was dominated by the void surface conductivity.
- PD activity during the preconditioning period at low temperatures increased the void surface conductivity and hence short-circuited the voids at low frequencies resulting in no PDs. This effect was not present at high temperatures. This indicates that the effect of PD by-products decays faster at higher temperatures.
- A simplified model for calculating void voltage that fits well to the measured data is proposed, with two capacitances representing the insulation and the void, and a resistance representing the void wall. This model was a satisfactory approximation for voids with a diameter larger than 5 mm, even though dielectric response had to be included in the model to fit the measured data at temperatures above 110°C.

ACKNOWLEDGMENT

REFERENCES

[1] Off-line partial discharge measurements on the stator winding insulation of rotating electrical machines, IEC TS 60034-27:2006.
[2] IEEE Guide for the Measurement of Partial Discharges in AC Electric Machinery, IEEE Std 1434-2014 (Revision of IEEE Std 1434-2000).
[3] IEEE Recommended Practice for Insulation Testing of AC Electric Machinery with High Voltage at Very Low Frequency, IEEE Std 433-2009 (Revision of IEEE Std 433-1974).

[4] U. Gäfvert, H. Edin and C. Forssén, "Modelling of partial discharge spectra measured with variable applied frequency," *IEEE Int. Conf. Prop. Appl. Dielectr. Mat.(ICPADM)*, 2003, vol. 3, pp. 839-842.

[5] C. Forssen and H. Edin, "Partial discharges in a cavity at variable applied frequency part 1: measurements," IEEE Trans. Dielectr. Electr. Insul., vol. 15, no. 6, pp. 1601-1609, 2008.

[6] C. Forssen and H. Edin, "Partial discharges in a cavity at variable applied frequency part 2: measurements and modeling," IEEE Trans. Dielectr. Electr. Insul., vol. 15, no. 6, pp. 1610-1616, 2008.

[7] H. Illias, G. Chen and P. Lewin, "Partial discharge behavior within a spherical cavity in a solid dielectric material as a function of frequency and amplitude of the applied voltage," IEEE Trans. Dielectr. Electr. Insul., vol. 18, no. 2, pp. 432-443, 2011.

[8] H. A. Illias, G. Chen, and P. L. Lewin, "Partial discharge measurements for spherical cavities within solid dielectric materials under different stress and cavity conditions," *Annu. Rep. Conf. Electr. Insul. Dielectr. Phenom. (CEIDP)*, 2009, pp. 388-391.

[9] G. Callender, T. Tanmaneeprasert, and P. L. Lewin, "Simulating partial discharge activity in a cylindrical void using a model of plasma dynamics," J. Phys. D: Appl. Phys., vol. 52, no. 5, p. 055206, 2019.

[10] M. Lévesque, E. David, and C. Hudon, "Effect of surface conditions on the electric field in air cavities," IEEE Trans. Dielectr. Electr. Insul., vol. 20, no. 1, pp. 71-81, 2013.

[11] E. Kuffel and W. S. Zaengl, *High-voltage engineering: fundamentals,* Pergamon Press, 1984.

[12] K. S. Cole and R. H. Cole, "Dispersion and absorption in dielectrics I. Alternating current characteristics," J. Chem. Phys., vol 9, no. 4, pp. 341-351, 1941.

[13] K. C. Kao, *Electric Polarization and Relaxation. Dielectric Phenomena in Solids*. San Diego, Academic Press, 2004 p. 99.

[14] M. Saltzer, U. Gäfvert, B. Källstrand, K. Johansson and L. Walfridsson, "Observation of space charge dynamics in air under DC electric fields," *Annu. Rep. Conf. Electr. Insul. Dielectr. Phenom. (CEIDP)*, 2011, pp. 141-144.

[15] C. Hudon, R. Bartnikas and M. R. Wertheimer, "Effect of physico-chemical degradation of epoxy resin on partial discharge behavior," IEEE Trans. Dielectr. Electr. Insul., vol. 2, no. 6, pp. 1083-1094, 1995.

[16] T. G. Aakre, E. Ildstad, and S. Hvidsten, "Time Development of Voltage Frequency Dependence of Partial Discharge Activity in Voids," *Nordic Insul. Symp. (NordIS)*, 2019.

[17] G. D. Robertson, D. M. Mason, and W. H. Corcoran, "The Kinetics of the Thermal Decomposition of Nitric Acid in the Liquid Phase," J. Phys. Chem., vol. 59, no. 8, pp. 683-690, 1955.

[18] T. A. Ve, F. Mauseth, and E. Ildstad, "Effect of water content on the conductivity of XLPE insulation," *Annu. Repo. Conf. Electr. Insul. Dielectr. Phenom. (CEIDP)*, 2012, pp. 649-653.

[19] High-voltage test techniques - Partial discharge measurements, IEC 60270:2000.

Sverre Hvidsten received the M.Sc. degree in 1992 at the Norwegian Institute of Technology (NTH) in Trondheim. During 1993 - 1994 he was a researcher at EFI in Norway. In 1999 he gained the Ph.D. in electrical engineering at The Norwegian University of Science and Technology (NTNU) in Trondheim. He now works as a Senior Research Scientist at SINTEF Energy Research (SEfAS).

Torstein Grav Aakre received the M.Sc degree from the Norwegian University of Technology and Science (NTNU) in Trondheim, Norway in 2013. He was then employed by SINTEF Energy Research. In 2016, he started a Ph.D. at NTNU regarding condition assessment of hydropower generator bars. His research interests are within electrical insulation materials, with a focus on condition assessment, conductivity and breakdown mechanisms.

Erling Ildstad received the M.Sc. degree in technical physics in 1978 and the Ph.D. degree in electrical power engineering in 1982 from NTNU in Trondheim, Norway. He has been a full-time professor of high voltage engineering at NTNU since 1993.

Paper V

Planned paper to IEEE Transactions on Dielectrics and Electrical Insulation 2020. Draft soon to be completed.

Partial Discharge Magnitude and Repetition Rate in Voids at Variable Voltage Frequency and Temperatures.

Paper VI

Planned paper to IEEE Transactions on Dielectrics and Electrical Insulation 2020. Draft soon to be completed.

Partial Discharges in Mainwall Insulation of Hydropower Generator Bars versus Voltage Frequency and Temperature

Bibliography

[1] NVE. Vannkraftstatistikk (Norwegian), 2019.

[2] T. M. Sneve. Aldersfordeling for komponenter i kraftsystemet, levetid og behov for reinvesteringer (Norwegian). *NVE*, 8, 2005.

[3] *Survey of Hydrogenerator Failures*. WG A1.10 CIGRÉ Technical brochure No. 392, 2009.

[4] R. Brütsch, M. Tari, K. Fröhlich, T. Weiers, and R. Vogelsang. Insulation failure mechanisms of power generators. *IEEE Electrical Insulation Magazine*, 24(4):17–25, 2008.

[5] G. C. Stone. Condition monitoring and diagnostics of motor and stator windings - a review. *IEEE Transactions on Dielectrics and Electrical Insulation*, 20(6):2073–2080, 2013.

[6] C. Hudon and M. Bélec. Partial discharge signal interpretation for generator diagnostics. *IEEE Transactions on Dielectrics and Electrical Insulation*, 12(2):297–319, 2005.

[7] R.P. Nair and S.B. Vishwanath. Analysis of partial discharge sources in stator insulation system using variable excitation frequency. *IET Science, Measurement and Technology*, 13(6):922–930, 2019.

[8] IEEE. IEEE guide for the measurement of partial discharges in AC electric machinery. Standard IEEE std 1434, IEEE, 2014.

[9] IEEE. Recommended practice for insulatinon tesiting of large AC rotating machinery with high voltage at very low frequency. Standard IEEE std 433, IEEE, 2009.

[10] M. Levesque, C. Hudon, and E. David. Insulation degradation analysis of stator bars subjected to slot partial discharges. In *2013 IEEE Electrical Insulation Conference, EIC 2013*, pages 479–483, 2013.

[11] C. Hudon, M. Levesque, D. H. Nguyen, C. Millet, and F. Truchon. Root cause analysis of generator failures. In *Conference Record of IEEE International Symposium on Electrical Insulation*, pages 199–203, 2012.

[12] C. Sumereder and T. Weiers. Significance of defects inside in-service aged winding insulations. *IEEE Transactions on Energy Conversion*, 23(1):9–14, 2008.

[13] M. Piller, G. Schena, A. Contin, and G. Rabach. Ground-wall insulation system analysis combining advanced imaging techniques and numerical simulation. *Electric Power Systems Research*, 116:444–450, 2014.

[14] D. Lenko, S. Schlögl, S. Bichler, G. Lemesch, F. Ramsauer, W. Ladstätter, J. Rosc, and W. Kern. New approaches towards the investigation on defects and failure mechanisms of insulating composites used in high voltage applications. *Composites Part B: Engineering*, 58:83–90, 2014.

[15] M. Lévesque, C. Hudon, N. Amyot, and L. Lamarre. Post-mortem dissection of stator bars and coils. In *EIC 2014 - Proceedings of the 32nd Electrical Insulation Conference*, pages 64–68, 2014.

[16] Xiongwei Jiang, Gang Liu, Guangchun Zhang, and Guangning Wu. Study on PD characteristics of insulation internal defects of large generator stator bar. In *Conference Record of the the 2002 IEEE International Symposium on Electrical Insulation (Cat. No.02CH37316)*, pages 14–18, April 2002.

[17] C. Pan, G. Chen, J. Tang, and K. Wu. Numerical modeling of partial discharges in a solid dielectric-bounded cavity: A review. *IEEE Transactions on Dielectrics and Electrical Insulation*, 26(3):981–1000, 2019.

[18] E. Kuffel and W. S. Zaengl. *High-voltage engineering: fundamentals*. Pergamon Press, 1984.

[19] A. Pedersen, G. C. Crichton, and I. W. McAllister. The theory and measurement of partial discharge transients. *IEEE Transactions on Electrical Insulation*, 26(3):487–497, 1991.

[20] C. Forssen and H. Edin. Partial discharges in a cavity at variable applied frequency part 2: measurements and modeling. *IEEE Transactions on Dielectrics and Electrical Insulation*, 15(6):1610–1616, 2008.

[21] R. Morrow and J. J. Lowke. Streamer propagation in air. *Journal of Physics D: Applied Physics*, 30(4):614, 1997.

[22] P. H. F. Morshuis. Degradation of solid dielectrics due to internal partial discharge: Some thoughts on progress made and where to go now. *IEEE Transactions on Dielectrics and Electrical Insulation*, 12(5):905–913, 2005.

[23] A. Cavallini and G. C. Montanari. Effect of supply voltage frequency on testing of insulation system. *IEEE Transactions on Dielectrics and Electrical Insulation*, 13(1):111–121, 2006.

[24] C. Forssen and H. Edin. Partial discharges in a cavity at variable applied frequency part 1: measurements. *IEEE Transactions on Dielectrics and Electrical Insulation*, 15(6):1601–1609, 2008.

[25] H. Illias, G. Chen, and P. Lewin. Partial discharge behavior within a spherical cavity in a solid dielectric material as a function of frequency and amplitude of the applied voltage. *IEEE Transactions on Dielectrics and Electrical Insulation*, 18(2):432–443, 2011.

[26] H. N. O, T. R. Blackburn, B. T. Phung, H. Zhang, and R. H. Khawaja. Investigation of electric field distribution in power cables with voids. In *2006 IEEE 8th International Conference on Properties applications of Dielectric Materials*, pages 637–640, June 2006.

[27] H. Illias, M. A. Tunio, H. Mokhlis, G. Chen, and A. H. A. Bakar. Determination of partial discharge time lag in void using physical model approach. *IEEE Transactions on Dielectrics and Electrical Insulation*, 22(1):463–471, 2015.

[28] K. Wu, Y. Suzuoki, and L. A. Dissado. The contribution of discharge area variation to partial discharge patterns in disc-voids. *Journal of Physics D: Applied Physics*, 37(13):1815–1823, 2004.

[29] C. Hudon, R. Bartnikas, and M. R. Wertheimer. Surface conductivity of epoxy specimens subjected to partial discharges. In *Conference Record of IEEE International Symposium on Electrical Insulation*, pages 153–155, 1990.

[30] I.W. McAllister. Electric field theory and the fallacy of void capacitance. *IEEE Transactions on Electrical Insulation*, 26(3):458–459, 1991.

[31] G.C. Crichton, P.W. Karlsson, and A. Pedersen. Partial discharges in ellipsoidal and spheroidal voids. *IEEE Transactions on Electrical Insulation*, 24(2):335–342, 1989.

[32] S.A. Boggs. Partial discharge - part III: Cavity-induced PD in solid dielectrics. *IEEE Electrical Insulation Magazine*, 6(6):11–16, 1990.

[33] Z. Achillides, M. G. Danikas, and E. Kyriakides. Partial discharge modeling and induced charge concept: Comments and criticism of Pedersen's model and associated measured transients. *IEEE Transactions on Dielectrics and Electrical Insulation*, 24(2):1118–1122, April 2017.

[34] E. M. El-Refaie, M. K. Abd Elrahman, and O. Zidane. Internal discharge properties for different solid insulating materials. In *2016 Eighteenth International Middle East Power Systems Conference (MEPCON)*, pages 962–967, Dec 2016.

[35] P. K. Olsen, F. Mauseth, and E. Ildstad. The effect of DC superimposed AC voltage on partial discharges in dielectric bounded cavities. In *2014 ICHVE International Conference on High Voltage Engineering and Application*, pages 1–4, Sep. 2014.

[36] L. Niemeyer. A generalized approach to partial discharge modeling. *IEEE Transactions on Dielectrics and Electrical Insulation*, 2(4):510–528, 1995.

[37] F. Gutfleisch and L. Niemeyer. Measurement and simulation of PD in epoxy voids. *IEEE Transactions on Dielectrics and Electrical Insulation*, 2(5):729–743, 1995.

[38] A. C. Gjærde. A phenomenological aging model for combined thermal and electrical stress. *IEEE Transactions on Dielectrics and Electrical Insulation*, 4(6):674–680, 1997.

[39] C. Hudon, R. Bartnikas, and M. R. Wertheimer. Analysis of degradation products on epoxy surfaces subjected to pulse and glow type discharges. In *1991 Annual Report. Conference on Electrical Insulation and Dielectric Phenomena*, pages 237–243, 1990.

[40] M. Lévesque, E. David, C. Hudon, and M. Bélec. Effect of surface degradation on slot partial discharge activity. *IEEE Transactions on Dielectrics and Electrical Insulation*, 17(5):1428–1440, 2010.

[41] P. H. F. Morshuis and F. H. Kreuger. The evolution of the discharge mechanism in a dielectric bounded cavity due to surface effects. pages 672–675, 1991.

[42] J. Kindersberger and C. Lederle. Surface charge decay on insulators in air and sulfurhexafluorid - part II: Measurements. *IEEE Transactions on Dielectrics and Electrical Insulation*, 15(4):949–957, 2008.

[43] C. Hudon, M. Bélec, and M. Lévesque. Study of slot partial discharges in air-cooled generators. *IEEE Transactions on Dielectrics and Electrical Insulation*, 15(6):1675–1690, 2008.

144

[44] T. G. Aakre, R. Skattenborg, and Ildstad. Limitations regarding use of the abc-model for interpretation of partial discharge measurements. In *2019 Nordic Insulation Symposium (NordIS)*, volume 26, 2019.

[45] E. Eberg, T. G. Aakre, G. Berg, and S. Hvidsten. Comparison of offline VLF PD measurements and online PD measurements on a 50-year-old hydrogenerator stator in norway. In *Electrical Insulation Conference, EIC 2018*, 2018.

[46] M. Farahani, H. Borsi, and E. Gockenbach. Dielectric response studies on insulating system of high voltage rotating machines. *IEEE Transactions on Dielectrics and Electrical Insulation*, 13(2):383–393, 2006.

[47] L. Lamarre and E. David. Temperature dependence of the resistance of modern epoxy mica insulation of hv rotating machines. *IEEE Transactions on Dielectrics and Electrical Insulation*, 15(5):1305–1312, 2008.

[48] M. Saltzer, U. Gäfvert, B. Källstrand, K. Johansson, and L. Walfridsson. Observation of space charge dynamics in air under DC electric fields. In *Annual Report - Conference on Electrical Insulation and Dielectric Phenomena, CEIDP*, pages 141–144, 2011.

[49] K. S. Cole and R. H. Cole. Dispersion and absorption in dielectrics I. alternating current characteristics. *The Journal of Chemical Physics*, 9(4):341–351, 1941.

[50] K. C. Kao. *Electric Polarization and Relaxation. Dielectric Phenomena in Solids*. Academic Press, 2004.

[51] N. L. Allen and P. N. Mikropoulos. Dynamics of streamer propagation in air. *Journal of Physics D: Applied Physics*, 32(8):913, 1999.

[52] R. Bartnikas and G. L. d'Ombrain. A study of corona discharge rate and energy loss in spark gaps. *IEEE Transactions on Power Apparatus and Systems*, 84(9):770–779, 1965.

[53] C. Pan, K. Wu, Y. Du, Y. Meng, Y. Cheng, and J. Tang. The effect of surface charge decay on the variation of partial discharge location. *IEEE Transactions on Dielectrics and Electrical Insulation*, 23(4):2241–2249, 2016.

[54] U. Gäfvert, H. Edin, and C. Forssén. Modelling of partial discharge spectra measured with variable applied frequency. In *Proceedings of the IEEE International Conference on Properties and Applications of Dielectric Materials*, volume 3, pages 839–842, 2003.

[55] T. A. Ve, F. Mauseth, and E. Ildstad. Effect of water content on the conductivity of XLPE insulation. In *Annual Report - Conference on Electrical Insulation and Dielectric Phenomena, CEIDP*, pages 649–653, 2012.

[56] IEC. Off-line partial discharge measurements on the stator winding insulation of rotating electrical machines. Standard IEC 60034-27, IEC, 2006.

[57] IEC. High voltage test techniques - partial discharge measurements. Standard IEC 60270, IEC, 2000.

[58] G. D. Robertson, D. M. Mason, and W. H. Corcoran. The kinetics of the thermal decomposition of nitric acid in the liquid phase. *The Journal of Physical Chemistry*, 59(8):683–690, 1955.

[59] G. Callender, T. Tanmaneeprasert, and P. L. Lewin. Simulating partial discharge activity in a cylindrical void using a model of plasma dynamics. *Journal of Physics D: Applied Physics*, 52(5):055206, 2019.

[60] R.W. Warfield and M.C. Petree. Electrical resistivity of polymers. *Polymer Engineering and Science*, 1(2):80–85, 1961.

[61] C. Hudon, R. Bartnikas, and M. R. Wertheimer. Effect of physico-chemical degradation of epoxy resin on partial discharge behavior. *IEEE Transactions on Dielectrics and Electrical Insulation*, 2(6):1083–1094, 1995.

[62] T. G. Aakre, E. Ildstad, S. Hvidsten, and A. Nysveen. Review of partial discharge and dielectric loss tests for hydropower generator bars. In *2017 Nordic Insulation Symposium (NordIS)*, volume 25, 2017.

[63] T. G. Aakre, E. Ildstad, and S. Hvidsten. Condition assessment of hydrogenerator stator bar insulation using partial discharge measurements. In *Electrical Insulation Conference, EIC 2018*, 2018.

[64] T. G. Aakre, E. Ildstad, and S. Hvidsten. Time development of voltage frequency dependence of partial discharge activity in voids. In *Nordic Insulation Symposium (NordIS)*, volume 26, 2019.

[65] T. G. Aakre, E. Ildstad, and S. Hvidsten. Partial discharge inception voltage of voids enclosed in epoxy/mica versus voltage frequency and temperature. *IEEE Transactions on Dielectrics and Electrical Insulation*, 27(1):190–197, 2020.